PROCESS DESIGN FOR PLASMA-BASED GAS-PHASE NUCLEATION OF CARBON NANOPARTICLES

By

JONATHAN COLE

Submitted in partial fulfillment of the requirements for the degree of
Doctor of Philosophy

Department of Chemical and Biomolecular Engineering

CASE WESTERN RESERVE UNIVERSITY

January, 2018

CASE WESTERN RESERVE UNIVERSITY
SCHOOL OF GRADUATE STUDIES

We hereby approve the thesis/dissertation of
Jonathan Cole

candidate for the degree of **Doctor of Philosophy***.

Committee Chair
R. Mohan Sankaran

Committee Member
Heidi Martin

Committee Member
Donald Feke

Committee Member
Giuseppe Strangi

Date of Defense
11/14/2017

*We also certify that written approval has been obtained
for any proprietary material contained therein

This is dedicated to the memory of Becca Stempel, who is missed very much in this world. Her voice won’t be forgotten.

ACKNOWLEDGMENTS

I would first like to thank my advisor, Dr. Mohan Sankaran, whose expression of confidence in me from the beginning led me down this path. The opportunities that I've been granted throughout my Ph.D. and will continue to see in the future would not have happened if it weren't for Mohan's dedication and resolute commitment to mine and all of his students' success.

This final product would not have been possible without the critical intervention of my colleagues, Dr. Mihai Bilici, Dr. Souvik Ghosh, Andrew Wang, Tianqi Liu, and Joseph Toth, especially when that intervention included hot pots and barbecues. Special thanks also goes to Dr. Cliff Hayman, without whose assistance during times of need I would never have progressed as far forward as I did, and whose guidance I've come to value immensely. I'm grateful to Dr. Hatsuo Ishida, who by generously granting the use of his Raman spectrometer has made a spectroscopist out of me. Our pleasant conversations on the side have been a very welcome distraction. Dr. Danqi Wang deserves many thanks for teaching me much of what I know about TEM and for being a confident and collected second pair of eyes. Our TEM sessions were a bright highlight throughout my time here, whether the samples were good or bad. Also, to Adam Maraschky: sorry I forgot to acknowledge you for the photos and videos in my seminar presentation. Your acknowledgment is now much more perpetually enshrined.

Some of the studies in this document were conducted in conjunction with my collaborators Dr. Yao Zhang, Dr. Abdurrahman Almethen, and Dr. Philip Hemmer, whom I've enjoyed working with and learning from. Additional thanks go to Dr. Heidi Martin and Dr. John Angus for the use of their CVD equipment, which was pivotal in

reaching a compelling conclusion to my projects. Additional collaborators on other projects that I would like to acknowledge are Dr. Sukrit Sucharitakul, Dr. Alireza Rashed, Dr. Mohamed ElKabbash, Glynis Schumacher, and Dr. Giuseppe Strangi of the Case Physics Department, all of whose good humor has been a great source of enjoyment.

Dr. J. Mann deserves special recognition for his kind patience in granting me a second chance when I struggled in his course at the very beginning of my studies and for jump-starting in me a new interest in mathematics at the same time. I'm also very grateful to Dr. Uziel Landau for his patient and enlightening discussions with me after class and for lending his ear and offering his kind support during emotionally stressful times, which I will not forget.

I'm indebted to my parents, who have absolutely no idea what on earth I've been up to here, and we're all better off for that. Eccentric characters though they may be, I can't begin to conceive of better examples of what it means to love unconditionally. There's no replacement for the perspective I've been given by them and will always see the world with. They humble me tremendously, and I hope I may pay that gift forward in the coming years.

Finally, there's no way to completely express my appreciation and gratitude to my fiancée Poroshat, who's struggled along with me throughout the last four years of my Ph.D. Whether on one side of the planet or the other, her presence has changed the tenor of my life profoundly, very unexpectedly, and perhaps undeservedly. She's given me motivation to face and overcome my personal and professional challenges and the hope that I can, one day, become the person that I wish I could be.

ABSTRACT

Process Design for Plasma-Based Gas-Phase Nucleation of Carbon Nanoparticles

By JONATHAN COLE

This thesis project is focused on designing plasma processes for the controlled synthesis of nanoscale forms of crystalline carbon. The general mechanism for all the plasma systems is homogeneous nucleation, which describes the formation of nanoparticles in the gas-phase from vapor precursors. Nucleation from a preexisting seed particle is also explored, which is similar to heterogeneous nucleation on a substrate except that in some cases nucleation of the seed itself occurs within a gas flow.

The first type of plasma system that was studied is a direct-current (DC), atmospheric-pressure microplasma that effectively limits particle growth so that nanosized (<10 nm) particles are synthesized. However, this plasma is limited in volume and requires metal electrodes that could produce impurities. For this reason, the second type of plasma system is a radio-frequency capacitively-coupled plasma (RF CCP), where the excitation of the plasma occurs with two metal electrodes on the outside of a quartz tube, eliminating contact with metal. This was studied in two variations, one at low pressure with a large plasma volume and, therefore, greater throughput, and one at atmospheric-pressure. To scale-up nanoparticle throughput at atmospheric-pressure, a high-voltage, alternating current, coaxial dielectric barrier discharge (DBD) was also studied. Characterization by Raman spectroscopy and transmission electron microscopy of the nanoparticles synthesized from different precursors in the various plasma systems is presented.

The different processes were found to produce distinct materials, with the DC microplasma producing small quantities of diamond but a majority of mixed sp^2 and sp^3 phases of carbon. The RF CCP processes, meanwhile, produced more graphitic material, including onion-like carbon. Seeded growth by coinjection of methane and silane yielded cubic crystalline silicon carbide nanoparticles instead of diamond, but preexisting silicon nanoparticles produced by RF CCP were demonstrated with microwave plasma-enhanced chemical vapor deposition to be suitable seeds for diamond nucleation and also for photoluminescent silicon-vacancy defect centers in diamond. Scale-up of particle throughput in atmospheric-pressure plasma reactors was accomplished using two DBD reactors with different plasma volumes. These were found to produce comparable particle size distributions under some conditions while also maintaining comparable gas breakdown voltages.

Contents

List of Tables

List of Figures

Chapter 1: Introduction and motivation

1.1 The phases of carbon and their properties on the nanoscale

Carbon in its crystalline form can adopt two dissimilar allotropes, graphite and diamond, the former of which is opaque, electrically conducting, and exhibits a layered hexagonally-coordinated structure, and the latter of which is translucent, insulating, and exhibits a tetrahedrally-coordinated cubic structure. The pressure-temperature phase diagram of bulk carbon is well-established[1,2] and reflects the higher thermodynamic stability of graphite near room temperature and pressure. The Gibbs free energy of transformation becomes favorable for diamond at extremely high pressures (on the order of GPa) when the unfavorable amount of work needed to sustain a volume of low density graphite outweighs the contribution of graphite's more favorable specific entropy.[3] Nonetheless, both allotropes are known to persist well into each other's respective region of thermodynamic stability on account of sluggish kinetics,[1] which has two effects. One is that synthesis of diamond is therefore very difficult, requiring not only high pressure but also high temperature and in some cases a catalyst.[4] The other effect is beneficial, as the sluggish kinetics also make diamond metastable at many conditions, including room temperature and pressure, allowing its extraordinary properties to be utilized widely.

Bulk forms of diamond have extraordinary mechanical, thermal, and optical properties and are used for various applications such as cutting tools, heat removal, and windows. Nanoscale (<10 nm) diamond particles, or nanodiamonds, are of interest for more advanced applications, such as bio-imaging and quantum information processing.[5–8] Nanodiamonds fall into the broader category of Group IV quantum dots, which also include Si, SiC, and Ge, and which photoluminesce due to the quantum confinement

effect.[9–11] In the case of nanodiamond, however, the interband transition energy is typically not within visible wavelengths of light; instead, useful photoluminescence (PL) in nanodiamond originates from defect centers,[9,11] or color centers, which are heteroatom substitutions in the diamond lattice, usually accompanied by at least one adjacent vacancy in the lattice.[12] Examples of these defect centers include nitrogen-vacancy (N-V),[13] the most common, and silicon-vacancy (Si-V)[14] pairs. Defect centers in diamond have elicited great interested because they are stable and resistant to spin decoherence at room temperature.[15,16] In addition, nanodiamond is biocompatible,[17] inert to ambient oxygen and moisture, and has an abundantly tunable surface chemistry[18] that enables colloidal stability in a variety of solvents as well as attachment of functional molecules, including drugs,[19] proteins,[20] and fluorophores.[5]

Graphite also exists at the nanoscale as particles, but unlike its bulk form, which consists of flat, stacked sheets, highly crystalline graphitic nanoparticles form concentric, spherical layers and are thus referred to as ‘fullerenic’ or ‘onion-like’ carbon (OLC).[21] OLC particles do not photoluminesce in the way that nanodiamonds do, but they are biocompatible and can be surface functionalized with fluorophores and drug molecules, making them of interest for many of the same biomedical applications.[22] In addition, like bulk graphite, OLC is electrically conductive and therefore of interest in areas such as electrochemical energy storage.[23,24] Like carbon nanotubes, OLC offers a high specific surface area, making it suitable for high power devices,[25] particularly as an additive in supercapacitor electrode materials.[26] The conductivity of OLC can additionally be improved by doping with elements such as boron.[27,28]

Besides OLC, small nm-size stacks of graphitic sheets and singular nm-size graphene flakes have also been synthesized.[29] These belong to a broader class of materials known as carbonaceous quantum dots, which have widely varying degrees of crystallinity. Other examples include amorphous carbon nanoparticles and polymeric nanoparticles.[30,31] Carbonaceous quantum dots exhibit photoluminescence which, unlike nanodiamond, is primarily dependent on surface states.[31]

1.2 Nanodiamond synthesis methods

Synthesis of nanocrystalline carbon particles of either allotrope for the aforementioned applications presents a significant engineering challenge requiring control of phase purity, particle size, aggregation, and dopant and/or defect concentration. Nanodiamonds in particular are challenging owing to their thermodynamic barrier. The most common methods that have been employed for producing nanodiamond particles follow thermodynamic stability and apply high pressure and temperature process conditions. One example is detonation of explosive materials such as TNT and hexogen in a closed chamber, where pressure and temperature approach 30 GPa and 4,000 K.[5,32,33] In this case, the resulting nanodiamonds are small and monodisperse, around 5 nm, and naturally contain nitrogen impurities that, upon electron-irradiation and annealing, can form N-V centers.[34] However, the detonation process also results in significant byproducts of non-diamond carbon, some metal, and also severe aggregation of particles into clusters.[35] Post-processing of detonation nanodiamond is thus required and includes removal of impurities, such as by acid etching or oxidation in air,[36,37] and break up agglomerates by nano-milling.[38]

Another common nanodiamond production method is to convert graphite by a high-pressure high-temperature (HPHT) process.[4] In this case, diamond seeds are compressed at pressures up to 10 GPa in the presence of graphitic carbon dissolved in a molten metal catalyst; over time, carbon precipitates onto the seeds, growing them into larger diamonds. Unlike detonation, the HPHT process enables much more flexibility in incorporation of dopants. Reducing the size of the resulting diamond particles to the nanoscale, however, requires successive milling steps, acid washing, and size separation by centrifugation,[39,40] Both detonation and HPHT processes thus have significant drawbacks relating to the extreme conditions required and to their costly post-processing steps.

Extreme pressure and temperature are not necessary for diamond growth, though. Indeed, chemical vapor deposition (CVD) of diamond films, which most often occurs under vacuum, is a well-established process.[41,42] The central pillar of CVD diamond growth is inhibition of diamond surface reconstruction and active etching of non-diamond carbon by an abundance of H atoms during simultaneous incorporation of growth species onto the diamond surface.[43,44] Growth species and H atoms are produced by gas-phase reactions driven by some activation source, the most common being a hot filament or microwave plasma. Activated species then diffuse to a heated substrate that has typically been seeded by abrasion with diamond powder.

The most commonly used feed mixture in CVD is CH_4/H_2, in which case it is generally accepted that the primary growth species is CH_3 radicals.[45,46] C/H/O mixtures such as CO_2/CH_4 and CO/H_2 have also been reported,[47,48] in which case CH_3 is also suspected to play the primary growth role.[49] Growth of highly nanocrystalline films with

a grain size less than 10 nm has also been achieved with Ar/CH_4,[50] which results in a hydrogen-poor environment relative to the other mixtures. It has been argued that C_2 is primarily responsible for growth in that environment instead of CH_3,[51] though not without controversy.[52] Ar/CH_4 mixtures also tend to result in simultaneous homogeneous nucleation of soot particles.[53,54]

The propagation of diamond during CVD, while not expected to occur from inspection of bulk equilibrium thermodynamics alone, is nonetheless kinetically driven by chemical potential and temperature gradients within the growth chamber.[43,44,55,56] However, while this supports the growth of diamond, *de novo* nucleation of diamond is less well understood.[42] Here, surface thermodynamics must be considered, which may dramatically shift the stability lines of diamond and graphite.

1.3 Thermodynamics of nanoscale carbon

In order to explain the presence of nanodiamonds discovered in meteorites,[57] Nuth first suggested the possibility that small diamonds could be more stable than graphite at low pressure because of surface energy favorability.[58] Later, Badziag *et al.* computed the binding energy of small hydrogenated clusters of carbon arranged tetrahedrally and hexagonally and determined that, up to a diameter of about 3 nm, the tetrahedral configuration, *i.e.*, diamond, was indeed more stable.[59] Gamarnik computed the free energies of diamond and graphite from charge lattice models and reached a similar conclusion, showing also a theoretical dependence of the size stability of diamond on temperature.[60,61] More recently, molecular dynamics simulations by Dubois and Pineau obtained a different result showing OLC particles to be more stable than nanodiamond

except at high pressure, similar to the bulk phase diagram of carbon.[62] Experimentally, OLC has been obtained in a simple manner by annealing of nanodiamonds,[26,63,64] though this conversion has also been observed to occur in reverse by electron[65] or laser[66] irradiation of OLC. Although there is thus some conflicting evidence regarding the thermodynamic stability of nanodiamond, it is clear that confining it to small particle sizes is important.

1.4 Homogeneous synthesis of nanoparticles from the vapor phase

Briefly, homogeneous nucleation of a condensed phase from a vapor-phase precursor occurs when the concentration of the vapor becomes supersaturated enough to drive the formation of a critical nucleus size.[67] Nuclei undergo competition between condensation and evaporation of precursor, and because at the nanoscale a large fraction of atoms or molecules in a particle exist on its surface, evaporation rates increase rapidly with decreasing particle size. The critical nucleus size is the point at which the condensed particle will not spontaneously evaporate and is determined in part by the surface energy of the material. Creating a supersaturated vapor requires establishment of some negative temperature gradient in time, with higher cooling rates corresponding to higher supersaturation and therefore a greater likelihood of reaching a critical nucleus size.

Many methods of synthesizing nanoparticles from the vapor phase generate this temperature gradient by some mode of thermal excitation.[68] These include flames, laser ablation,[69] spark ablation,[70,71] and thermal plasma.[72,73] In each of these cases, the precursor is either vaporized by or generated within the thermalized region and then cooled to supersaturation as it convects away, producing an aerosol. The particle size

distribution and level of agglomeration depend strongly on the temperature of the thermalized region and the rate at which the gas cools.[72,74]

Recently, non-thermal plasmas have become increasingly used to homogenously nucleate particles.[75–77] These plasmas are ionized gases that are named as such because they consist of species that are not at thermal equilibrium with each other. Specifically, they contain electrons with average kinetic energies on the order of 10,000 K along with positive ions and neutral gas molecules and radicals that are close to room temperature.[75] Thus, hot electrons can dissociate gas molecules into precursor species which cool and reach supersaturation rapidly on account of the low neutral gas temperature. Nuclei then form inside of the plasma as opposed to outside in the case of thermal excitation.[78] After nuclei formation, the non-thermal plasma environment provides additional benefits. Importantly, despite the low gas temperature, nanoparticles may reach high temperatures due to electron-ion recombination and other reactions on particle surfaces, allowing them to crystallize.[78,79] Electron attachment to particles also imparts them with a negative surface charge that causes them to repel each other, preventing agglomeration.[80] A narrow particle size distribution can be further promoted in atmospheric-pressure microdischarges by means of confined reactor residence times.[81–83] When it comes to carbon in particular, non-thermal plasmas are especially attractive for homogeneous synthesis of nanoparticles given the success of the microwave plasma-enhanced CVD process in growing diamond.

1.5 Outline

In this thesis, homogeneous nucleation of carbon nanoparticles from gas-phase precursors in non-thermal plasma systems is investigated, with particular attention given to the influence of gas-phase chemistry on material characteristics. In Chapter 2, an atmospheric-pressure DC microdischarge is studied using two precursors, ethanol and methanol, as a follow-up to a study by Kumar *et al.*[84] which resulted in nanodiamond synthesis. Drawbacks of the DC microdischarge system include low particle throughput and contamination from metal electrodes, so, in Chapter 3, a low pressure radio-frequency capacitively-coupled plasma (RF CCP) reactor with a larger volume and no internal electrodes is studied. Here, a few strategies for promoting selective growth of diamond phase were attempted, including addition of H_2 to the reactant feed and seeding by coinjection of SiH_4. Also, as an alternative to homogeneous nucleation, the suitability of Si nanoparticles for heterogeneous growth of diamond is tested using a microwave plasma-enhanced CVD process. In Chapter 4, the RF CCP reactor design is adapted to atmospheric-pressure operation by reducing its size, making it analogous to the DC microdischarge and enabling higher power densities than at low pressure. In Chapter 5, the issue of low particle throughput at atmospheric-pressure is addressed using a dielectric barrier discharge. A reactor geometry is chosen which allows for scaling of plasma volume, and therefore gas throughput, without increasing the plasma breakdown voltage. Two different size reactors and their ability to produce identical particle size distributions of Ni nanoparticles at equivalent conditions are investigated. Finally, in Chapter 6, perspective on the results of the previous chapters and suggestions for future research directions in this area are offered.

1.6 References

1. Bundy, F. P. *et al.* The pressure-temperature phase and transformation diagram for carbon; updated through 1994. *Carbon N. Y.* **34,** 141–153 (1996).

2. van Thiel, M. & Ree, F. H. Theoretical Description of the Graphite, Diamond, and Liquid Phases of Carbon. *Int. J. Thermophys.* **10,** 227–236 (1989).

3. Fried, L. E. & Howard, W. M. Explicit Gibbs free energy equation of state applied to the carbon phase diagram. *Phys. Rev. B* **61,** 8734–8743 (2000).

4. Bundy, F. P., Hall, H. T., Strong, H. M. & Wentorf, R. H. Man-Made Diamonds. *Nature* **176,** 51–55 (1955).

5. Mochalin, V. N., Shenderova, O., Ho, D. & Gogotsi, Y. The properties and applications of nanodiamonds. *Nat. Nanotechnol.* **7,** 11–23 (2011).

6. Balasubramanian, G. *et al.* Nanoscale imaging magnetometry with diamond spins under ambient conditions. *Nature* **455,** 648–651 (2008).

7. Greentree, A. D., Fairchild, B. A., Hossain, F. M. & Prawer, S. Diamond integrated quantum photonics. *Mater. Today* **11,** 22–31 (2008).

8. Aharonovich, I., Greentree, A. D. & Prawer, S. Diamond photonics. *Nat. Photonics* **5,** 397–405 (2011).

9. Fan, J. & Chu, P. K. Group IV nanoparticles: Synthesis, properties, and biological applications. *Small* **6,** 2080–2098 (2010).

10. Shenderova, O. *et al.* Carbon-dot-decorated nanodiamonds. *Part. Part. Syst. Charact.* **31,** 580–590 (2014).

11. Montalti, M., Cantelli, A. & Battistelli, G. Nanodiamonds and silicon quantum dots: ultrastable and biocompatible luminescent nanoprobes for long-term bioimaging. *Chem. Soc. Rev.* **44,** 4853–4921 (2015).

12. Jelezko, F. & Wrachtrup, J. Single defect centres in diamond: A review. *Phys. Status Solidi* **203,** 3207–3225 (2006).

13. Doherty, M. W. *et al.* The nitrogen-vacancy colour centre in diamond. *Phys. Rep.* **528,** 1–45 (2013).

14. Wang, C., Kurtsiefer, C., Weinfurter, H. & Burchard, B. Single photon emission from SiV centres in diamond produced by ion implantation. *J. Phys. B At. Mol. Opt. Phys.* **39,** 37–41 (2006).

15. Balasubramanian, G. *et al.* Ultralong spin coherence time in isotopically engineered diamond. *Nat. Mater.* **8,** 383–387 (2009).

16. Tisler, J. *et al.* Fluorescence and spin properties of defects in single digit nanodiamonds. *ACS Nano* **3,** 1959–1965 (2009).

17. Mohan, N., Chen, C.-S., Hsieh, H.-H., Wu, Y.-C. & Chang, H.-C. In vivo imaging and toxicity assessments of fluorescent nanodiamonds in caenorhabditis elegans. *Nano Lett.* **10,** 3692–3699 (2010).

18. Krueger, A. & Lang, D. Functionality is key: Recent progress in the surface modification of nanodiamond. *Adv. Funct. Mater.* **22,** 890–906 (2012).

19. Chow, E. K. *et al.* Nanodiamond Therapeutic Delivery Agents Mediate Enhanced Chemoresistant Tumor Treatment. *Sci. Transl. Med.* **3,** (2011).

20. Liu, Y. L. & Sun, K. W. Protein functionalized nanodiamond arrays. *Nanoscale Res. Lett.* **5,** 1045–1050 (2010).

21. Ugarte, D. Onion-like Graphitic Particles. *Carbon N. Y.* **33,** 989–993 (1995).

22. Camisasca, A. & Giordani, S. Carbon nano-onions in biomedical applications: Promising theranostic agents. *Inorganica Chim. Acta* **468,** 67–76 (2017).

23. Pech, D. *et al.* Ultrahigh-power micrometre-sized supercapacitors based on onion-like carbon. *Nat. Nanotechnol.* **5,** 651–654 (2010).

24. Portet, C., Yushin, G. & Gogotsi, Y. Electrochemical performance of carbon onions, nanodiamonds, carbon black and multiwalled nanotubes in electrical double layer capacitors. *Carbon N. Y.* **45,** 2511–2518 (2007).

25. Simon, P. & Gogotsi, Y. Capacitive energy storage in nanostructured carbon-electrolyte systems. *Acc. Chem. Res.* **46,** 1094–1103 (2013).

26. Zeiger, M., Jäckel, N., Mochalin, V. & Presser, V. Review: Carbon onions for electrochemical energy storage. *J. Mater. Chem. A* **4,** 3172–3196 (2016).

27. Mykhailiv, O. *et al.* Boron-Doped Polygonal Carbon Nano-Onions: Synthesis and Applications in Electrochemical Energy Storage. *Chem. - A Eur. J.* **23,** 7132–7141 (2017).

28. Serin, V. *et al.* Evidence for the solubility of boron in graphite by electron energy loss spectroscopy. *Carbon N. Y.* **38,** 547–554 (2000).

29. Baker, S. N. & Baker, G. A. Luminescent carbon nanodots: Emergent nanolights. *Angew. Chemie - Int. Ed.* **49,** 6726–6744 (2010).

30. Wang, J. *et al.* Opportunities and Challenges of Fluorescent Carbon Dots in Translational Optical Imaging. *Curr. Pharm. Des.* **21,** (2015).

31. Zhu, S. *et al.* The photoluminescence mechanism in carbon dots (graphene quantum dots, carbon nanodots, and polymer dots): current state and future perspective. *Nano Res.* **8,** 355–381 (2015).

32. Greiner, N. R., Phillips, D. S., Johnson, J. D. & Volk, F. Diamonds in detonation soot. *Nature* **333,** 440–442 (1988).

33. Dolmatov, V. Y. Detonation synthesis ultradispersed diamonds: properties and applications. *Russ. Chem. Rev.* **70,** 607–626 (2001).

34. Vlasov, I. I. *et al.* Nitrogen and luminescent nitrogen-vacancy defects in detonation nanodiamond. *Small* **6,** 687–694 (2010).

35. Danilenko, V. V. Nanodiamonds: Problems and prospects. *J. Superhard Mater.* **32,** 301–310 (2010).

36. Dolmatov, V. Y. in *Ultrananocrystalline Diamond - Synthesis, Properties, and Applications* 347–377 (William Andrew Inc., 2006).

37. Osswald, S., Yushin, G., Mochalin, V., Kucheyev, S. O. & Gogotsi, Y. Control of sp2/sp3 carbon ratio and surface chemistry of nanodiamond powders by selective oxidation in air. *J. Am. Chem. Soc.* **128,** 11635–11642 (2006).

38. Ozawa, M. *et al.* Preparation and behavior of brownish, clear nanodiamond colloids. *Adv. Mater.* **19,** 1201–1206 (2007).

39. Boudou, J.-P. *et al.* High yield fabrication of fluorescent nanodiamonds.

Nanotechnology **20,** 235602 (2009).

40. Morita, Y. *et al.* A facile and scalable process for size-controllable separation of nanodiamond particles as small as 4 nm. *Small* **4,** 2154–2157 (2008).

41. Angus, J. C. & Hayman, C. C. Low-Pressure, Metastable Growth of Diamond and 'Diamondlike' Phases. *Science (80-.).* **241,** 913–921 (1988).

42. Angus, J. C. Diamond synthesis by chemical vapor deposition: The early years. *Diam. Relat. Mater.* **49,** 77–86 (2014).

43. Ashfold, M. N. R. *et al.* Unravelling aspects of the gas phase chemistry involved in diamond chemical vapour deposition. *Phys. Chem. Chem. Phys.* **3,** 3471–3485 (2001).

44. Butler, J. E., Mankelevich, Y. A., Cheesman, A., Ma, J. & Ashfold, M. N. R. Understanding the chemical vapor deposition of diamond: recent progress. *J. Phys. Condens. Matter* **21,** 364201 (2009).

45. Lee, S. S., Minsek, D. W., Vestyck, D. J. & Chen, P. Growth of diamond from atomic hydrogen and a supersonic free jet of methyl radicals. *Science (80-.).* **263,** 1596–1598 (1994).

46. Goodwin, D. G. Scaling laws for diamond chemical-vapor deposition. I. Diamond surface chemistry. *J. Appl. Phys.* **74,** 6888–6894 (1993).

47. Bachmann, P. K., Leers, D. & Lydtin, H. Towards a general concept of diamond chemical vapour deposition. *Diam. Relat. Mater.* **1,** 1–12 (1991).

48. Gries, T., Vandenbulcke, L., Rouzaud, J. N. & de Persis, S. Diagnostics in dusty

C–H–O plasmas with diamond and graphitic nanoparticle generation. *Plasma Sources Sci. Technol.* **19,** 25015 (2010).

49. Petherbridge, J. R., May, P. W., Pearce, S. R. J., Rosser, K. N. & Ashfold, M. N. R. Low temperature diamond growth using CO2/CH4 plasmas: Molecular beam mass spectrometry and computer simulation investigations. *J. Appl. Phys.* **89,** 1484–1492 (2001).

50. Xiao, X., Birrell, J., Gerbi, J. E., Auciello, O. & Carlisle, J. A. Low temperature growth of ultrananocrystalline diamond. *J. Appl. Phys.* **96,** 2232–2239 (2004).

51. Sternberg, M., Zapol, P. & Curtiss, L. A. Carbon dimers on the diamond (100) surface: Growth and nucleation. *Phys. Rev. B* **68,** 205330 (2003).

52. Rabeau, J. R., John, P., Wilson, J. I. B. & Fan, Y. The role of C2 in nanocrystalline diamond growth. *J. Appl. Phys.* **96,** 6724–6732 (2004).

53. Hassouni, K., Mohasseb, F., Bénédic, F., Lombardi, G. & Gicquel, A. Formation of soot particles in Ar/H2/CH4 microwave discharges during nanocrystalline diamond deposition: A modeling approach. *Pure Appl. Chem.* **78,** 1127–1145 (2006).

54. Aggadi, N. *et al.* Structural and chemical characterisation of soot particles formed in Ar/H2/CH4 microwave discharges during nanocrystalline diamond film synthesis. *Diam. Relat. Mater.* **15,** 908–912 (2006).

55. Hassouni, K., Silva, F. & Gicquel, A. Modelling of diamond deposition microwave cavity generated plasmas. *J. Phys. D. Appl. Phys.* **43,** 153001 (2010).

56. Raty, J.-Y. & Galli, G. Ultradispersity of diamond at the nanoscale. *Nat. Mater.* **2,** 792–795 (2003).

57. Lewis, R. S., Ming, T., Wacker, J. F., Anders, E. & Steel, E. Interstellar diamonds in meteorites. *Nature* **326,** 160–162 (1987).

58. Nuth, J. A. Are Small Diamonds Thermodynamically Stable in the Interstellar Medium? *Astrophys. Space Sci.* **139,** 103–109 (1987).

59. Badziag, P., Verwoerd, W. S., Ellis, W. P. & Greiner, N. R. Nanometre-sized diamonds are more stable than graphite. *Nature* **343,** 244–245 (1990).

60. Gamarnik, M. Y. Energetical preference of diamond nanoparticles. *Phys. Rev. B* **54,** 2150–2156 (1996).

61. Gamarnik, M. Y. Size-Related Stabilization of Diamond Nanoparticles. *NanoStructured Mater.* **7,** 651–658 (1996).

62. Dubois, V. & Pineau, N. New developments of the CARTE thermochemical code: A two-phase equation of state for nanocarbons. *J. Appl. Phys.* **119,** 15903 (2016).

63. Cebik, J. *et al.* Raman spectroscopy study of the nanodiamond-to-carbon onion transformation. *Nanotechnology* **24,** 205703 (2013).

64. Mykhaylyk, O. O., Solonin, Y. M., Batchelder, D. N. & Brydson, R. Transformation of nanodiamond into carbon onions: A comparative study by high-resolution transmission electron microscopy, electron energy-loss spectroscopy, x-ray diffraction, small-angle x-ray scattering, and ultraviolet Raman spectroscopy. *J. Appl. Phys.* **97,** 74302 (2005).

65. Banhart, F. & Ajayan, P. M. Carbon onions as nanoscopic pressure cells for diamond formation. *Nature* **382,** 433–435 (1996).

66. Xiao, J., Ouyang, G., Liu, P., Wang, C. X. & Yang, G. W. Reversible nanodiamond-carbon onion phase transformations. *Nano Lett.* **14,** 3645–3652 (2014).

67. Seinfeld, J. & Pandis, S. in *Atmospheric Chemistry and Physics: From Air Pollution to Climate Change* 408–429 (John Wiley & Sons, Inc., 2006).

68. Swihart, M. T. Vapor-phase synthesis of nanoparticles. *Curr. Opin. Colloid Interface Sci.* **8,** 127–133 (2003).

69. Tarasenka, N., Stupak, A., Tarasenko, N., Chakrabarti, S. & Mariotti, D. Structure and Optical Properties of Carbon Nanoparticles Generated by Laser Treatment of Graphite in Liquids. *ChemPhysChem* **18,** 1074–1083 (2017).

70. Borra, J.-P., Jidenko, N., Hou, J. & Weber, A. Vaporization of bulk metals into single-digit nanoparticles by non-thermal plasma filaments in atmospheric pressure dielectric barrier discharges. *J. Aerosol Sci.* **79,** 109–125 (2015).

71. Pfeiffer, T. V., Feng, J. & Schmidt-Ott, A. New developments in spark production of nanoparticles. *Adv. Powder Technol.* **25,** 56–70 (2014).

72. Girshick, S. L. & Chiu, C.-P. Homogeneous Nucleation of Particles from the Vapor Phase in Thermal Plasma Synthesis. *Plasma Chem. Plasma Process.* **9,** 355–369 (1989).

73. Girshick, S. L. Particle nucleation and growth in thermal plasmas. *Plasma Sources*

Sci. Technol. **3,** 388–394 (1994).

74. Flagan, R. C. & Lunden, M. M. Particle structure control in nanoparticle synthesis from the vapor phase. *Mater. Sci. Eng. A* **204,** 113–124 (1995).

75. Kortshagen, U. R. *et al.* Nonthermal Plasma Synthesis of Nanocrystals: Fundamental Principles, Materials, and Applications. *Chem. Rev.* **116,** 11061–11127 (2016).

76. Mariotti, D. & Sankaran, R. M. Microplasmas for nanomaterials synthesis. *J. Phys. D. Appl. Phys.* **43,** 323001 (2010).

77. Chiang, W.-H., Richmonds, C. & Sankaran, R. M. Continuous-flow, atmospheric-pressure microplasmas: a versatile source for metal nanoparticle synthesis in the gas or liquid phase. *Plasma Sources Sci. Technol.* **19,** 34011 (2010).

78. Lopez, T. & Mangolini, L. On the nucleation and crystallization of nanoparticles in continuous-flow nonthermal plasma reactors. *J. Vac. Sci. Technol. B* **32,** 61802 (2014).

79. Kramer, N. J., Aydil, E. S. & Kortshagen, U. R. Requirements for plasma synthesis of nanocrystals at atmospheric pressures. *J. Phys. D. Appl. Phys.* **48,** 35205 (2015).

80. Boufendi, L. & Bouchoule, A. Industrial developments of scientific insights in dusty plasmas. *Plasma Sources Sci. Technol.* **11,** A211–A218 (2002).

81. Kumar, A. *et al.* Ligand-free Ni nanocluster formation at atmospheric pressure via rapid quenching in a microplasma process. *Nanotechnology* **25,** 385601 (2014).

82. Lin, P. A. & Sankaran, R. M. Plasma-Assisted Dissociation of Organometallic Vapors for Continuous, Gas-Phase Preparation of Multimetallic Nanoparticles. *Angew. Chemie - Int. Ed.* **50,** 10953–10956 (2011).

83. Sankaran, R. M., Holunga, D., Flagan, R. C. & Giapis, K. P. Synthesis of blue luminescent Si nanoparticles using atmospheric-pressure microdischarges. *Nano Lett.* **5,** 537–541 (2005).

84. Kumar, A. *et al.* Formation of nanodiamonds at near-ambient conditions via microplasma dissociation of ethanol vapour. *Nat. Commun.* **4,** 2618 (2013).

Chapter 2: Isolation of diamond nanoparticles in an atmospheric-pressure DC microplasma

2.1 Introduction

Gas-phase homogeneous nucleation of diamond has been previously reported in capacitively-coupled RF plasmas,[1] microwave-assisted flames,[2–4] microwave plasma CVD,[5] and DC arcs.[6] Phase purity (diamond vs. nondiamond forms of carbon) and size distribution of the resulting free-standing particles have typically been uncontrolled. Recently, nanodiamond synthesis from ethanol has been shown in an atmospheric-pressure DC microplasma.[7] In these novel plasmas,[8,9] the particle size distribution is controlled by the confined residence time of the reactor design.[10–12] An interesting aspect of the study was that it was determined that addition of H_2 to the gas feed enhanced the phase selection of diamond, analogous to selective etching and destabilization of non-diamond carbon by H atoms in the deposition of diamond by CVD.[13] In general for diamond CVD, it has been shown that the phase of carbon growth that occurs during the process can be predicted by the atomic fractions of C, H, and O in the gas feed.[14,15] The region of this CHO ternary diagram, also called the Bachmann diagram, in which diamond grows is bounded on its lower end by the line connecting the molecule CO with the H vertex,[16] meaning any molecule or mixture of molecules containing an equal number of C and O atoms is likely to produce diamond films in CVD (we note that the Bachmann diagram does not make any predictions regarding rate of growth[16]). In this study, the ability of different molecular precursors to synthesize diamond in a DC microdischarge is compared. Based on the principles described by the Bachmann diagram, the molecules that were selected are methanol, CH_3OH, which lies within the

diamond region, and ethanol, C_2H_5OH, which lies in the region of non-diamond carbon growth.

2.2 Experimental design

A schematic diagram of the DC microdischarge reactor is shown in Figure 2-1. The discharge is formed between a stainless steel capillary cathode (316 stainless steel, .007" I.D., 1/16" O.D., 2" length) and a grounded stainless steel wire mesh anode (304 stainless steel, 400x400 squares per inch, .001" wire diameter) separated by a gap of approximately 2 mm. Bias between the electrodes is applied by a negative high voltage power supply (Power Designs Pacific, Inc. model HV-1547). A ballast resistor of 160 kΩ is added to the circuit between the cathode and negative terminal of the supply, and a 500 Ω resistor is added between the anode and ground terminal of the supply for the purpose of measuring current through the circuit. The plasma discharge and electrodes are viewable through a quartz tube (0.16" I.D., 1/4" O.D.) concentric with the capillary which also isolates the reactor from the environment and insulates the two electrodes from each other.

In order to provide a controlled amount of precursor vapor to the reactor on the order of 10 to 1,000 ppm, Ar carrier gas is bubbled through liquid precursor, either ethanol (EtOH) or methanol (MeOH). The temperature of the bubbler is controlled by a Neslab model RTE-111 chiller. The concentration of precursor in the process gas stream is further adjusted through a series of two dilution streams of pure Ar with an exhaust stream in between (see Figure 2-1). The carrier, dilution, and exhaust flow rates are all controlled by thermal mass flow controllers. Pressure on either end of the bubbler was

measured with Bourdon gauges. Check valves were installed on either end of the bubbler as well to help prevent rapid pressure bursts through the liquid. The concentration of precursor in the feed, y_p, was then estimated from the following equation:

$$y_p = \frac{Q_p(Q_c + Q_p + Q_{dil1} - Q_{Ex})}{(Q_c + Q_p + Q_{dil1})(Q_c + Q_p + Q_{dil1} + Q_{dil2} - Q_{Ex})} \quad (2.1)$$

where Q_c, Q_p, Q_{dil1}, Q_{dil2}, and Q_{Ex} are the volumetric flowrates of carrier gas, precursor, first and second dilutions, and exhaust stream, respectively. Q_p is estimated by

$$Q_p = \frac{Q_c}{p/p^*(T) - 1} \quad (2.2)$$

where p is the overhead pressure of the bubbler and $p^*(T)$ is the vapor pressure of the precursor as a function of temperature, T. In all trials, the electrical current and total gas volumetric flow rate through the plasma were maintained at 3.6 mA and 100 sccm, respectively. A total flow rate of 100 sccm through the capillary resulted in a backing pressure (and therefore a bubbler overhead pressure) typically around 10 psig. The capillary was cleared of any potential debris prior to installation by running thin tungsten wire through it followed by a methanol rinse.

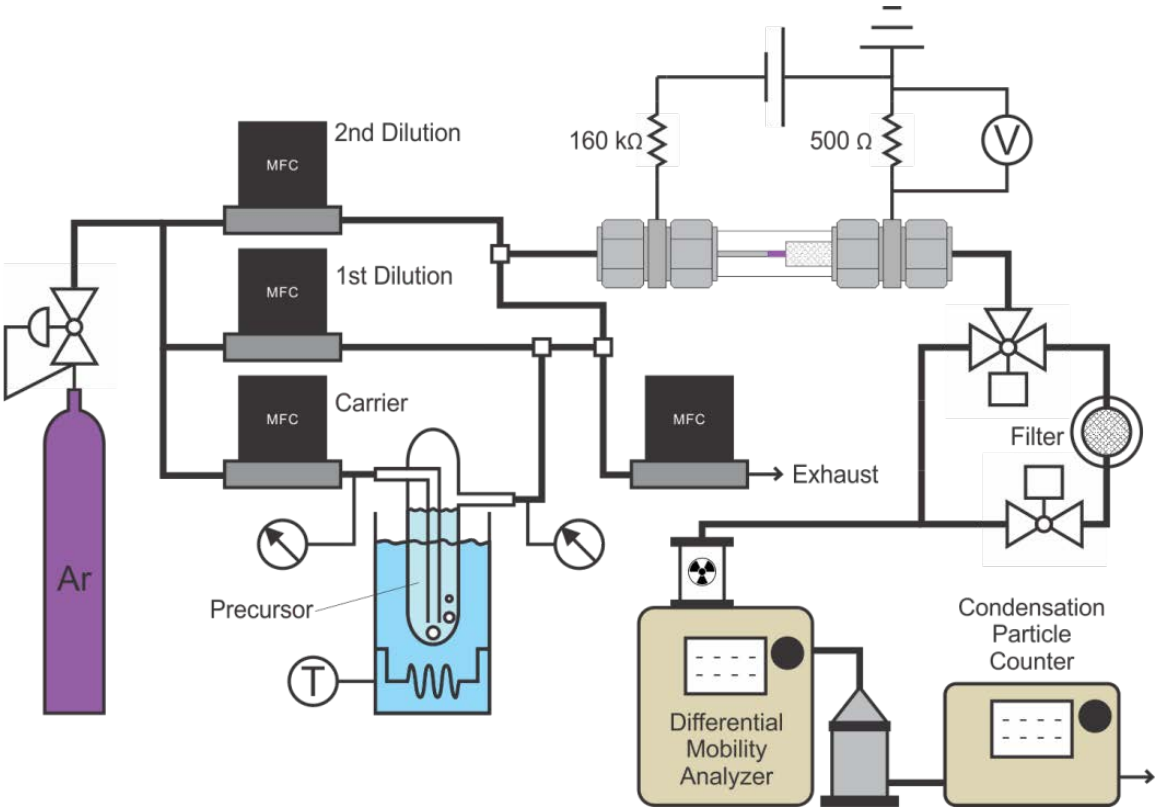

Figure 2-1. An overview of the experimental setup, including gas plumbing, electrical circuitry, and online measurements.

Size distributions of particles synthesized in the reactor were measured online by a scanning mobility particle sizer spectrometer (SMPS) which consisted of an electrostatic classifier (EC), differential mobility analyzer (DMA), and condensation particle counter (CPC) from TSI, Inc. (Models 3080, 3085, and 3776, respectively). The EC was equipped with a 710 μm impactor at the inlet and Model 3077 aerosol neutralizer. The reactor effluent was diluted with 1.4 slm of N_2 prior to entering the SMPS (additional information on the role of N_2 dilution is given in Section 5.3). Sample powders were collected downstream of the plasma using 25 mm diameter PTFE fiber filter with 100 nm equivalent pore size (Millipore, Inc. JVWP02500) held between

washers pressed together with two KF25 flange adapters for subsequent chemical purification and analysis with Raman spectroscopy and transmission electron microscopy (TEM). The SMPS was utilized to verify a nearly 100% collection efficiency by the filter.

Before each experiment, a plasma was initiated and maintained in pure Ar at 3.6 mA and monitored with the SMPS to ensure a clean gas flow. At each set of operating conditions with precursor added, the PSD produced by the reactor was typically found to converge to a particular final shape within about two minutes. At least five scans of steady-state operation were collected and averaged to produce the PSDs shown, with error bars representing the standard error of the mean (SE) in each measurement bin.

Powder samples were typically collected over a period of five days. The powders were purified to remove nondiamond carbon and metal contaminants by a previously reported acid purification technique.[17] Briefly, the powder was placed in a round-bottom flask with 2.5 mL of a 3:1 mixture of sulfuric and nitric acids, respectively, and heated to roughly 130 °C under reflux for 2 hours, diluted in water, and vacuum filtered through another 100 nm pore-size PTFE filter. Finally, the cleaned powder was sonicated in a vial with methanol to remove and disperse.

A few μL from each sample set, purified and unpurified, were dropped onto 3 nm thick carbon film coated Cu grids (Ted Pella, Inc. 01824) for TEM analysis. TEM was performed using an FEI Tecnai F30 at 300 kV accelerating voltage. Electron energy loss spectroscopy (EELS) and energy-dispersive X-ray spectroscopy (EDS) were performed in STEM mode. Raman spectroscopy was performed on dry powder as collected using a Horiba Jobin Yvon LabRAM HR800 spectrometer equipped with CCD detector and two grating systems at 600 and 1800 lines per mm. A 632.81 nm He/Ne laser with minimum

spot size of 1 μm^2 was used as excitation, and an Olympus BH-2 optical microscope was used for specimen imaging and laser focusing. The spectrometer was calibrated before every session using either the 520 cm^{-1} Stokes shift from a Si wafer or the 1332 cm^{-1} Stokes shift from a Macle diamond gem.

2.3 Results and discussion

A summary of SMPS measurements for carbon nanoparticles synthesized from EtOH and MeOH precursor vapor in the DC microdischarge over a range of concentrations is shown in Figure 2-2. Concentrations were chosen such that a comparison could be made between the two precursors at equal mass inputs of carbon. EtOH was found to produce more than an order of magnitude higher particle number concentration than MeOH. Additionally, with increasing precursor concentration, the PSD peak shifts to higher mean diameters in the case of EtOH but not in the case of MeOH. The concentration dependence of the PSDs is most probably related to a combination of the nucleation, growth, and agglomeration rates.[18,19] In the case of MeOH, the increase in particle number concentration without a concomitant shift in the particle mean diameter as concentration is increased could indicate an accelerating nucleation rate but little change in growth and agglomeration rates. With EtOH, on the other hand, the shift in the particle mean diameter indicates a more significant contribution from growth and perhaps agglomeration rates. The larger particle formation rate for EtOH than MeOH is consistent with previously reported results for soot formation in flames.[20]

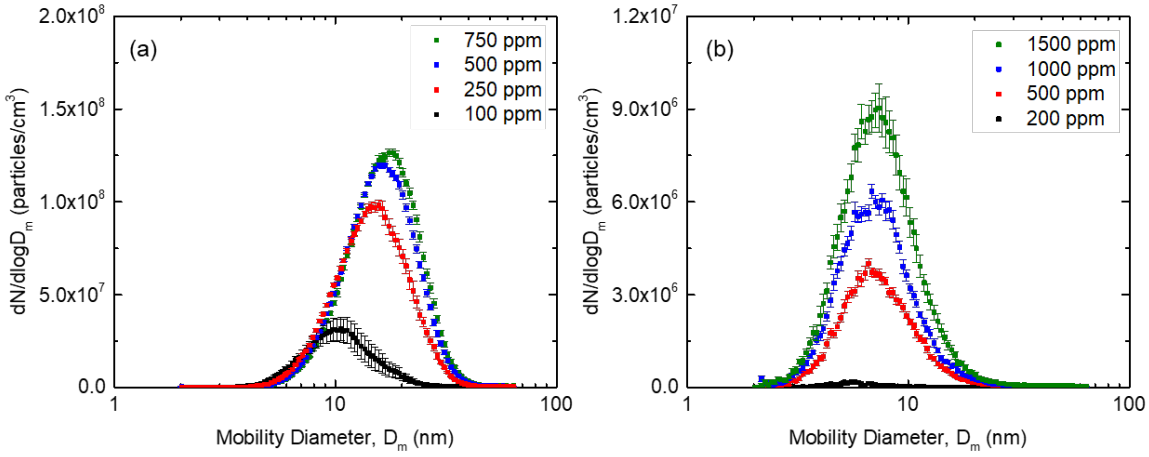

Figure 2-2. PSDs measured by SMPS at varying precursor concentrations for (a) EtOH and (b) MeOH.

Photos of the powders collected at 500 ppm EtOH and 1000 ppm MeOH are shown in Figure 2-3(a), along with their Raman spectra. While EtOH produced a black powder, the color of the powder produced from methanol was brownish-grey. The Raman spectra, however, were very similar. Spectra of commercially available unpurified and purified detonation diamond from Adamas Nanotechnologies, Inc. are also shown for comparison in Figure 2-3(b). The most prominent features observed for our synthesized powders are the so-called D and G bands at approximately 1330 and 1595 cm^{-1}, respectively. Both bands are fairly wide, with a full-width at half-maximum around 150 cm^{-1}, indicating a highly amorphous structure.[21] The spectra are very similar in appearance to that found for raw detonation powder, which consists of about 70% diamond by weight.[22] The concealment of diamond signal in the detonation powder is due in part to the excitation wavelength of the incident laser, which is more selective toward sp^2-coordinated carbon.[21] In comparison, the Raman spectrum for commercially

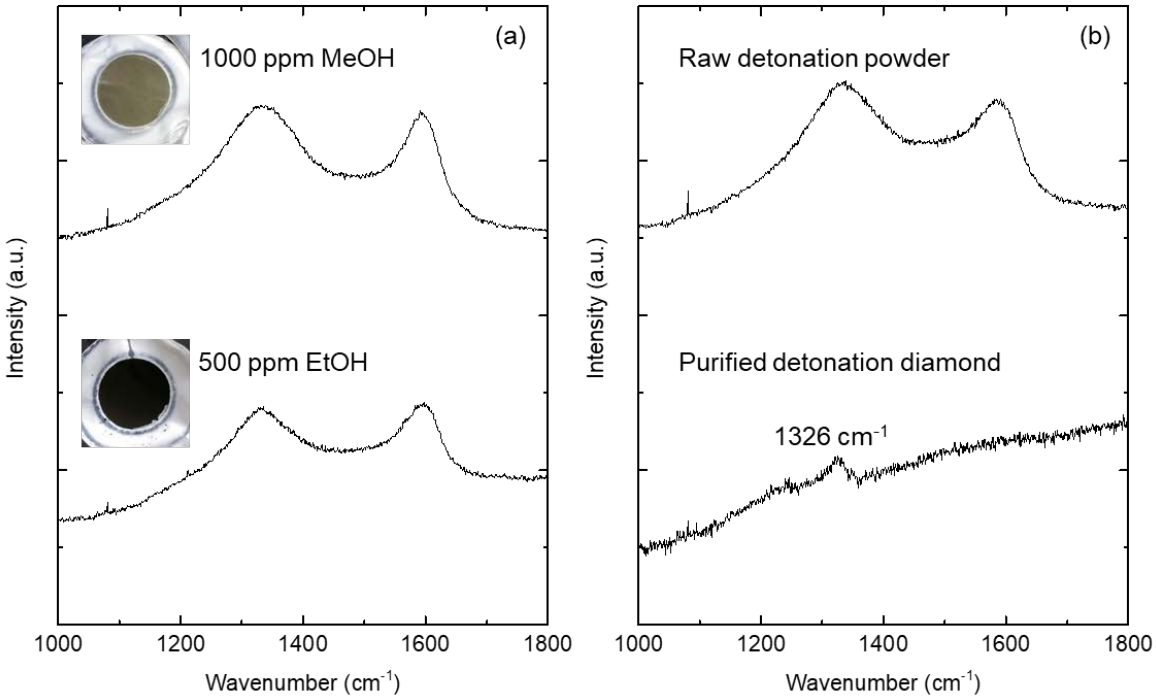

Figure 2-3. Raman spectra of (a) the two experimentally synthesized powders and (b) commercially obtained raw and acid-purified detonation diamond. Insets: photos of synthesized powders as collected.

purified detonation diamond sample exhibits a small peak near 1326 cm^{-1} corresponding to diamond and the G band is also absent. The phonon scattering peak arising from diamond is down-shifted from its typical position at 1332 cm^{-1} and broadened because of phonon confinement from size effects.[23] Similarly, purification was carried out on synthesized powders in order to isolate any diamond phase, but, unfortunately, the amount of material remaining after the acid treatment was too small for Raman analysis.

Representative TEM images of powders synthesized from EtOH and MeOH are shown in Figures 2-4(a-d). Both samples were found to be composed of a mixture of phases. While the majority of the material appeared amorphous, some graphitic regions in

the form of turbostratic sheets and onion-like carbon were also observed, along with some large dense spheres (such as in Figure 2-4(b)). Crystal lattice spacings were also visible. However, while some of the spacings matched with what would be expected for cubic diamond, near 2.06 Å, for example (see Figure 2-4(a)), other spacings were also found, with those in the range of 2.46-2.54, 2.10-2.16, and 1.45-1.53 Å being particularly frequent (see Figure 2-4(f), for example). While the spacings could not be assigned to a material, EDS shown in Figure 2-4(e), revealed the presence of Fe, Ni,, which most likely originated from the stainless steel electrodes used in the reactor.

EELS offers a unique chemical signature for different allotropes of carbon, including diamond, that circumvents any ambiguity arising from interpretation of crystal structure. Representative EELS of the MeOH and EtOH-derived samples are shown in Figure 2-5. Importantly, the peak at 285.5 eV corresponds to electron energy level transitions between 1s and π^* orbitals and therefore can only originate from carbon that is sp^2 or sp-coordinated. The region around 300 eV, meanwhile, corresponds to energy level transitions between 1s and σ^* orbitals and therefore appears in all forms of carbon but exhibits a fine structure that is unique to different ordered morphologies.[24] In amorphous carbon, this region appears only as a wide band. Both sample spectra in Figure 2-5 appear amorphous; for reference, the EEL spectrum of the amorphous carbon film on the TEM grid itself is also shown.

Although the electron beam is converged to a spot size less than 10 nm when probing EELS, signal from a small diamond crystal could nonetheless be covered by interference from non-diamond carbon. Removal of metals and non-diamond carbon by acid treatment allows the diamond phase to be isolated. TEM samples of both of the

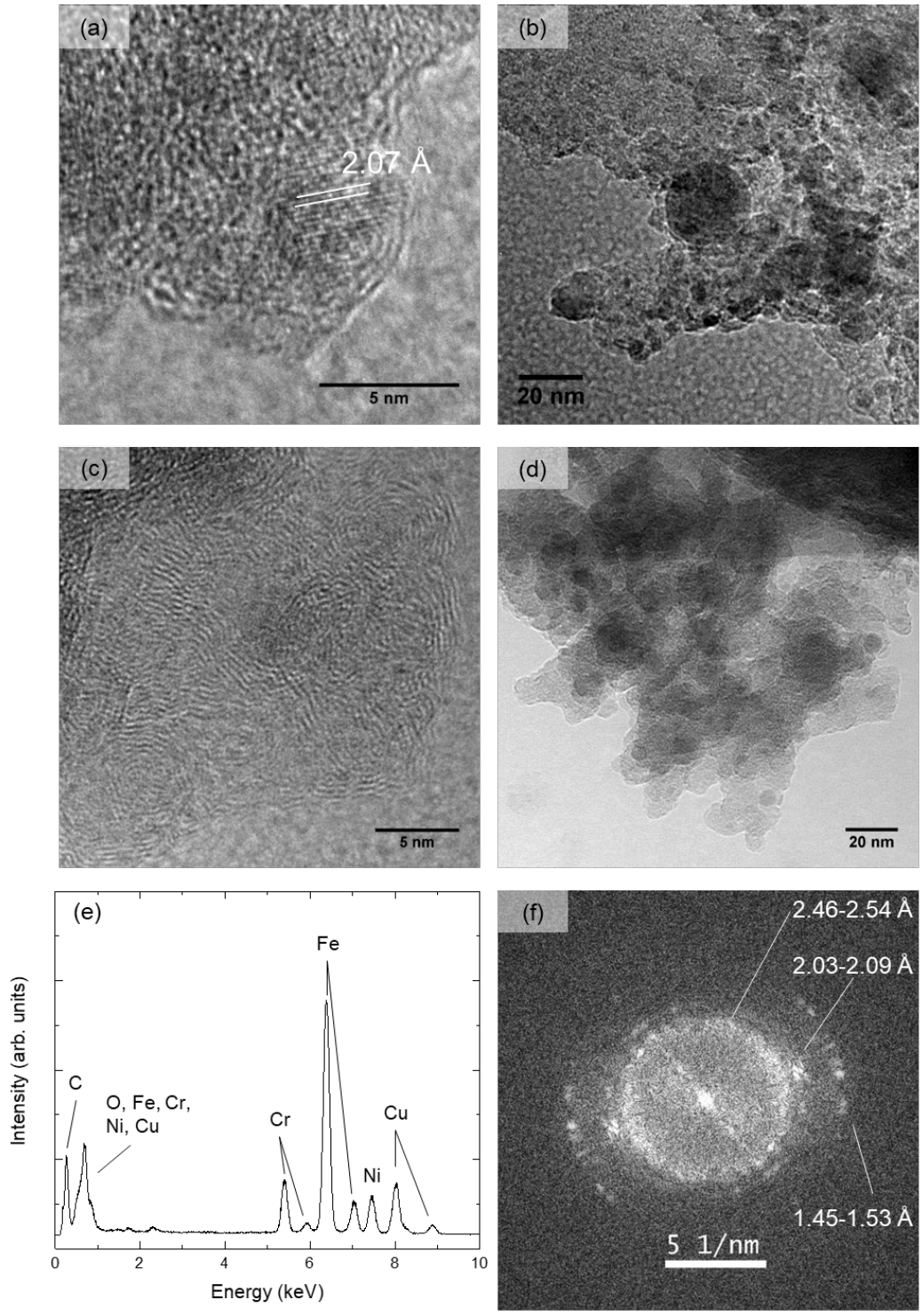

Figure 2-4. Example TEM images of material produced using (a,b) 1000 ppm MeOH and (c,d) 500 ppm EtOH. The image in (a) shows an example direct-space lattice measurement. (e) Example EDS showing the presence of Fe, Ni, and Cr in the specimens. Signal from Cu originates from the TEM support grid itself. (f) Example fast Fourier transform exhibiting some of the lattice spacings commonly observed throughout the specimens.

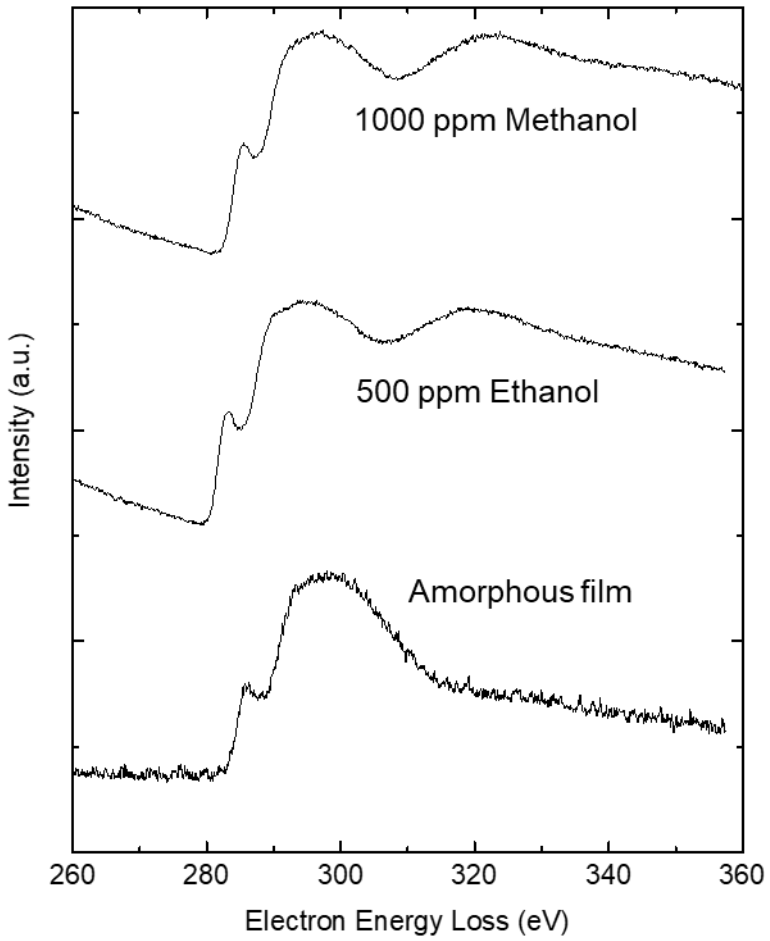

Figure 2-5. EELS obtained from unpurified experimentally-synthesized specimens. EELS of the amorphous carbon film suspended on the TEM grid itself is included for comparison.

treated and filtered MeOH and EtOH-derived specimens were prepared, although material could only be located on the MeOH-derived specimen after some searching, which is shown in Figure 2-6(a). Small crystallites a few nm in size were observed in aggregated clusters, with all measured lattice spacings corresponding to reflections of cubic diamond. Moreover, EELS on the aggregated clusters, shown in Figure 2-6(b), exhibited the characteristic fine structure of diamond.[24] For comparison, the EEL

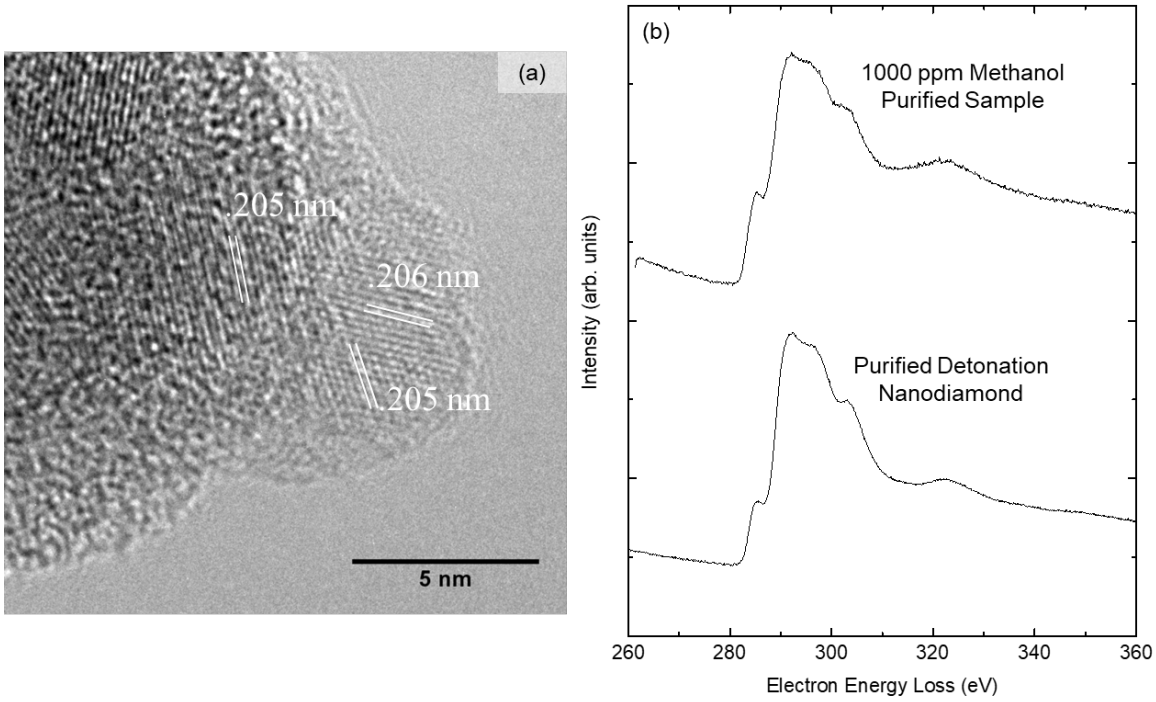

Figure 2-6. (a) TEM image of material synthesized from 1000 ppm MeOH after purification. Direct-space lattice measurements are shown which correspond to the (111) reflection of cubic diamond. (b) EELS of the specimen shown in (a), along with EELS of commercially purified detonation diamond powder for comparison.

spectrum of commercially purified detonation soot is also shown. In both cases, there is still a small peak corresponding to the 1s to π* transition. This may be due in part to a layer of graphitic carbon that has been shown to spontaneously reconstruct on the surface of small diamond particles[25] and is common to many detonation diamond samples and difficult to remove.[17]

2.4. Conclusions and Future Work

Particles of carbon were homogeneously nucleated in a DC microdischarge using ethanol and methanol as precursors. Both precursors nucleated particles, though ethanol was found to be more than an order of magnitude more efficient in terms of carbon conversion. Raman analysis showed little difference in the material produced from either precursor. Analysis by TEM revealed a mixture of carbon phases along with the presence of metallic impurities. Conclusive evidence of the presence of diamond-phase carbon was obtained by purifying the powder produced from methanol in an acid mixture and probing the residual material with EELS.

2.5 Acknowledgments

This work was supported by NSF Grant No. CBET-1335990. We are grateful to Dr. Hatsuo Ishida for access to Raman spectroscopy and to Dr. Danqi Wang for assistance with TEM.

2.6 References

1. Mitura, S. Nucleation of diamond powder particles in an RF methane plasma. *J. Cryst. Growth* **80,** 417–424 (1987).

2. Frenklach, M. *et al.* Homogeneous nucleation of diamond powder in the gas phase. *J. Appl. Phys.* **66,** 395–399 (1989).

3. Howard, W. *et al.* Synthesis of diamond powder in acetylene oxygen plasma. *J. Appl. Phys.* **68,** 1247–1251 (1990).

4. Frenklach, M. *et al.* Induced nucleation of diamond powder. *Appl. Phys. Lett.* **59,** 546–548 (1991).

5. Gries, T., Vandenbulcke, L., Rouzaud, J. N. & de Persis, S. Diagnostics in dusty C–H–O plasmas with diamond and graphitic nanoparticle generation. *Plasma Sources Sci. Technol.* **19,** 25015 (2010).

6. Moriyoshi, Y. *et al.* Preparation and characterization of ultra-fine diamond powders obtained by using a d.c. arc plasma jet. *J. Mater. Sci.* **31,** 3579–3582 (1996).

7. Kumar, A. *et al.* Formation of nanodiamonds at near-ambient conditions via microplasma dissociation of ethanol vapour. *Nat. Commun.* **4,** 2618 (2013).

8. Mariotti, D. & Sankaran, R. M. Microplasmas for nanomaterials synthesis. *J. Phys. D. Appl. Phys.* **43,** 323001 (2010).

9. Chiang, W.-H., Richmonds, C. & Sankaran, R. M. Continuous-flow, atmospheric-pressure microplasmas: a versatile source for metal nanoparticle synthesis in the gas or liquid phase. *Plasma Sources Sci. Technol.* **19,** 34011 (2010).

10. Kumar, A. *et al.* Ligand-free Ni nanocluster formation at atmospheric pressure via rapid quenching in a microplasma process. *Nanotechnology* **25,** 385601 (2014).

11. Lin, P. A. & Sankaran, R. M. Plasma-Assisted Dissociation of Organometallic Vapors for Continuous, Gas-Phase Preparation of Multimetallic Nanoparticles. *Angew. Chemie - Int. Ed.* **50,** 10953–10956 (2011).

12. Sankaran, R. M., Holunga, D., Flagan, R. C. & Giapis, K. P. Synthesis of blue

luminescent Si nanoparticles using atmospheric-pressure microdischarges. *Nano Lett.* **5,** 537–541 (2005).

13. Angus, J. C. & Hayman, C. C. Low-Pressure, Metastable Growth of Diamond and 'Diamondlike' Phases. *Science (80-.).* **241,** 913–921 (1988).

14. Bachmann, P. K., Leers, D. & Lydtin, H. Towards a general concept of diamond chemical vapour deposition. *Diam. Relat. Mater.* **1,** 1–12 (1991).

15. Petherbridge, J. R., May, P. W. & Ashfold, M. N. R. Modeling of the gas-phase chemistry in C-H-O gas mixtures for diamond chemical vapor deposition. *J. Appl. Phys.* **89,** 5219–5223 (2001).

16. Ford, I. Boundaries of the diamond domain in the C-H-O diagram of carbon film deposition. *J. Phys. D. Appl. Phys.* **29,** 2229–2234 (1996).

17. Shenderova, O. *et al.* Carbon-dot-decorated nanodiamonds. *Part. Part. Syst. Charact.* **31,** 580–590 (2014).

18. Flagan, R. C. & Lunden, M. M. Particle structure control in nanoparticle synthesis from the vapor phase. *Mater. Sci. Eng. A* **204,** 113–124 (1995).

19. Girshick, S. L. & Chiu, C.-P. Homogeneous Nucleation of Particles from the Vapor Phase in Thermal Plasma Synthesis. *Plasma Chem. Plasma Process.* **9,** 355–369 (1989).

20. Schofield, K. & Steinberg, M. CH and C2 measurements imply a radical pool within a pool in acetylene flames. *J. Phys. Chem. A* **111,** 2098–2114 (2007).

21. Ferrari, A. C. & Robertson, J. Raman spectroscopy of amorphous, nanostructured, diamond-like carbon, and nanodiamond. *Philos. Trans. R. Soc. London A* **362,** 2477–2512 (2004).

22. Shenderova, O. *et al.* Surface chemistry and properties of ozone-purified detonation nanodiamonds. *J. Phys. Chem. C* **115,** 9827–9837 (2011).

23. Osswald, S., Mochalin, V. N., Havel, M., Yushin, G. & Gogotsi, Y. Phonon confinement effects in the Raman spectrum of nanodiamond. *Phys. Rev. B - Condens. Matter Mater. Phys.* **80,** 75419 (2009).

24. Berger, S. D. & McKenzie, D. R. EELS analysis of vacuum arc-deposited diamond-like films. *Philos. Mag. Lett.* **57,** 285–290 (1988).

25. Raty, J.-Y., Galli, G., Bostedt, C., van Buuren, T. W. & Terminello, L. J. Quantum confinement and fullerenelike surface reconstructions in nanodiamonds. *Phys. Rev. Lett.* **90,** 37401 (2003).

Chapter 3: Homogeneous synthesis of amorphous carbon nanoparticles and seeded growth of diamond in low-pressure RF and MW plasmas

3.1 Introduction

Low-pressure, low-temperature, flow-through, radio frequency capacitively-coupled plasma (RF CCP) reactors have previously been utilized to synthesize quantum dots of Group IV elements such as Si and Ge by homogenous nucleation in the gas phase, resulting in high crystallinity and small size dispersion.[1,2] Additionally, bottom-up synthesis from the gas phase has enabled controlled introduction of dopants that allow tuning of the nanoparticles' optoelectronic properties.[3–5] While RF CCP reactors have been employed for CVD of hydrogenated amorphous carbon, diamond-like carbon,[6] and diamond films,[7] there are few studies of homogeneous nucleation. The most pertinent to this study are by Mitura[8] and Frenklach *et al.*,[9–11] wherein diamond nanoparticles were detected and characterized by TEM. While the former study took place in an RF CCP, the latter studies took place in a high-temperature microwave plasma-assisted combustion reactor.

This chapter consists of two experimental studies. The first is homogeneous nucleation of carbon nanoparticles in an RF CCP in a similar reactor that was previously reported for Si and Ge nanoparticle synthesis.[1–5] De Bleecker *et al.* have modeled the formation mechanism of nanoparticle precursor molecules in a C_2H_2 discharge and suggested that they originate *via* polymerization of both negatively and positively charged hydrocarbon ions as well as radical aliphatic and polyaromatic hydrocarbons.[12,13] Although the particles synthesized in this work could also grow by a similar mechanism,

here, we focused on the morphology of the resulting particles and the possibility of tuning their carbon phase as a function of applied power and addition of H_2. Characterization is performed by Raman spectroscopy and transmission electron microscopy (TEM). The second is seeded growth of diamond in the gas phase by either adding SiH_4 to the hydrocarbon feedstock or CVD of diamond on a substrate by first synthesizing crystalline Si nanoparticles in the RF CCP reactor, then drop casting them as a suspension onto a copper substrate, followed by microwave plasma-enhanced CVD (MPCVD). The latter experiments serve as proof-of-concept that Si nanoparticles support diamond growth and could be applied in the future to all-gas-phase growth of diamond.

3.2 Experimental design

An overview of the reactor schematic is shown in Figure 3-1. The plasma reactor consisted of a 3/8" OD clear-fused quartz tube of wall thickness 0.05". Power was coupled to the gas discharge *via* two copper rings (1/2" OD, 0.04" thickness, ¼" wide) separated by a distance of 1" and positioned on the quartz tube so that the plasma would not make contact with the metal vacuum fittings on either end of the tube. The impedance of the RF power supply (RF VII, Inc. model RF-3-XIII) was matched to the system load impedance *via* a custom-made pi-configuration matching box. In each experiment, air variable capacitors were adjusted until the reflectance measured by the power supply reached zero and the plasma length was maximized. The reactor was pumped by a rotary-vane pump (Edwards RV3), and the pressure during experiments was controlled by a throttle valve at the pump inlet. Pressure was monitored by both a gas-dependent

Granville-Philips 275 Convectron Gauge and gas-independent Brooks CMC 1000 Torr capacitance manometer. All experiments were performed at a pressure of 50 Torr. Four thermal MFCs were used to supply feed gases to the reactor: Ar, CH_4, H_2, and a mixture of 1% SiH_4 in Ar. The total flow rate was 50 sccm for all experiments.

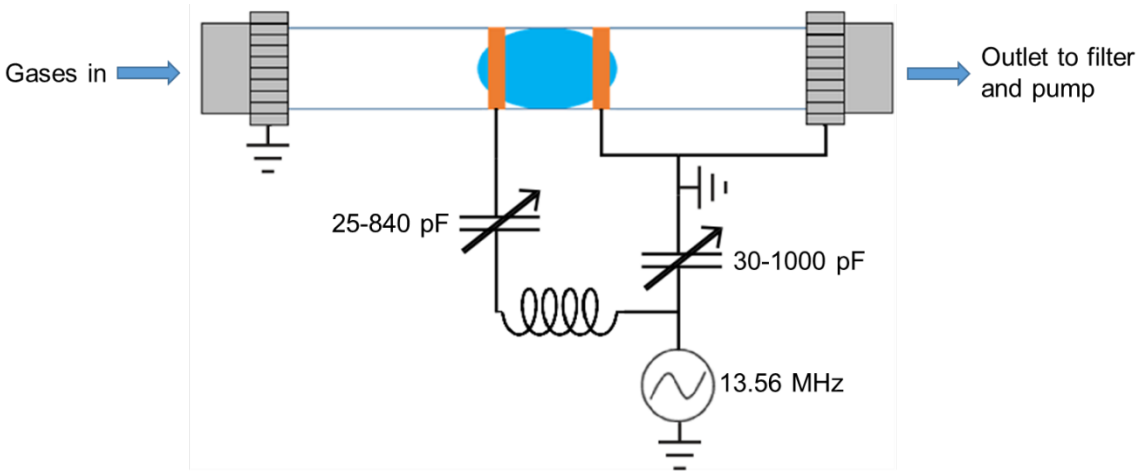

Figure 3-1. Schematic of the RF CCP reactor used to synthesize material in this chapter. The fixed inductor consisted of a 1/8" diameter copper wire coiled 21.5 turns around a ¾" ID with an average gap spacing of 0.08" between turns.

To measure the mass production rate of particles, the aerosol product was collected in a filter setup similar to that used in Chapter 2 placed downstream of the reactor. The gas line to the filter was isolated from the vacuum line by a three-way valve for removal and replacement without breaking vacuum in the reactor. Weight measurements were done on a Sartorius R200D microbalance.

Powder material was analyzed with Raman spectroscopy. In most cases, the spectra were recorded in the presence of the PTFE filter; the powder layers were thick enough that this did not contribute background peaks. Curve fitting and baseline correction of spectra that exhibited significant fluorescence were carried out with the aid

of Origin software. Carbon samples were fit using a total of five peaks in the first-order region of the spectrum and four peaks in the second-order region of the spectrum following the method employed by Sadezky *et al.* for soot-like powders.[14] To allow for maximum flexibility in the fitting procedure, every peak was fit to a Voigt curve, which is a convolution of Gaussian and Lorentzian functions:

$$f_{\mathrm{V}}(x) = y_0 + A\frac{2\ln 2}{\pi^{3/2}}\frac{w_{\mathrm{L}}}{{w_{\mathrm{G}}}^2}\int_{-\infty}^{\infty}\frac{\mathrm{e}^{-t^2}}{\left(\sqrt{\ln 2}\frac{w_{\mathrm{L}}}{w_{\mathrm{G}}}\right)^2 + \left(2\sqrt{\ln 2}\frac{x - x_{\mathrm{c}}}{w_{\mathrm{G}}} - t\right)^2}\,\mathrm{d}t \tag{3.1}$$

where y_0 is the function offset, A is the peak area, w_{L} is the full-width at half maximum (FWHM) of the Lorentzian component, w_{G} is the FWHM of the Gaussian component, x_{c} is the peak center, and x is wavenumber. The FWHM of each convoluted peak, w_{V}, was approximated by the following expression:

$$w_{\mathrm{V}} = .5346w_{\mathrm{L}} + \sqrt{.2166w_{\mathrm{L}}^2 + w_{\mathrm{G}}^2} \tag{3.2}$$

The choice of five peaks in the first-order region of the spectrum was justified in a manner similar to Sadezky *et al.*: one sample was selected for testing (carbon synthesized with 100 sccm of 0.9% methanol in Ar with 60 W at atmospheric pressure from the reactor detailed in the following chapter) in which fitting was performed using two, three, four, and then five peaks. Adjusted R^2 was evaluated for each number of peaks and found to reach a maximum at five. Adding a sixth peak resulted either in suppression of one of the peaks or failure to converge according to the prescribed tolerance.

Samples were prepared for TEM analysis by removing the collected material from the filters with a spatula and sonicating in a vial of 200 proof ethanol for 5 minutes. Each solution was diluted if necessary to a point at which color in the solution was just visible. One or two 2.5 μL drops of each solution were placed on an amorphous carbon film

copper grid (Ted Pella, Inc. 01824) and then placed in a vacuum oven to dry overnight at about 80 °C. To further remove organic impurities associated with the powders, some samples were treated with an additional step in which the original filter, with sample still collected on it, was loaded into a vacuum filtration column on top of a fritted glass base and washed repeatedly with cyclohexane. This resulted in substantial material loss, though it was confirmed that the procedure resulted in little change to the material's Raman spectrum. Fast Fourier transforms of direct space TEM images were generated using Gatan Microscopy Suite 3 software.

Seeded growth in a MPCVD from material synthesized in the RF plasma reactor was carried out in an Astex system (Model ECRM). Oxygen-free high conductivity (OFHC) copper (Cu) blank gaskets (1.895" diameter) were used as substrates which have been previously shown to avoid *de novo* diamond growth.[15] Substrates were cleaned prior to experiments for 30 minutes by a plasma at the same conditions as growth under a flow of 150 sccm H_2 and without RF heating of the substrate holder. A solution of Si nanoparticle seeds was prepared in 200 proof ethanol and slowly drop cast onto the Cu substrates and allowed to dry until a visible layer of particles was left behind. Growth conditions were kept constant for all experiments at 25 Torr, 100 sccm of 1% CH_4 in H_2, and 900 W MW excitation. The substrate holder was heated by a grounded RF susceptor, yielding a substrate surface temperature of ~610 °C as measured by a Williamson pyrometer (model 8220C-C-T).

3.3 Results and discussion

3.3.1 *Raman spectroscopy and TEM of homogeneously synthesized carbon material*

Raman spectra of carbon powder synthesized by homogeneous nucleation in the RF plasma reactor at 1% CH_4 in Ar are shown in Figure 3-2 as a function of applied RF power and H_2. The most prominent features in the first-order region of the spectra (between 1000 and 1800 cm^{-1}) are the D and G bands, centered at 1310-1320 and 1590-1600 cm^{-1}, respectively. In the second-order region of the spectra (between 2400 and 3400 cm^{-1}), the most prominent feature that appears in some samples is the 2D band centered near 2640 cm^{-1}. Some qualitative trends are apparent in the spectra regarding these features: with increasing power and increasing H_2 concentration, the peak intensity of the D band with respect to the G band increases, and the widths of both bands decrease. Meanwhile, the 2D band is mostly absent until both power and H_2 concentration are increased. Also, as the intensity of the 2D band increases, the G band appears to split in two; the second band, centered near 1610 cm^{-1}, is the so-called D' band and most likely contributes to the G band of all of the other spectra as well. The trends in these features appear to suggest a transition toward more crystalline graphitic carbon. Increasing power with no H_2 added to the feed results in only slight changes, but the addition of H_2 amplifies the influence of power, and the concentration of H_2 itself was found to have a significant impact. In the carbon synthesized without the addition of H_2, there is a particularly steep photoluminescence background that increases with power; this can be attributed to a relatively high degree of hydrogenation.[16]

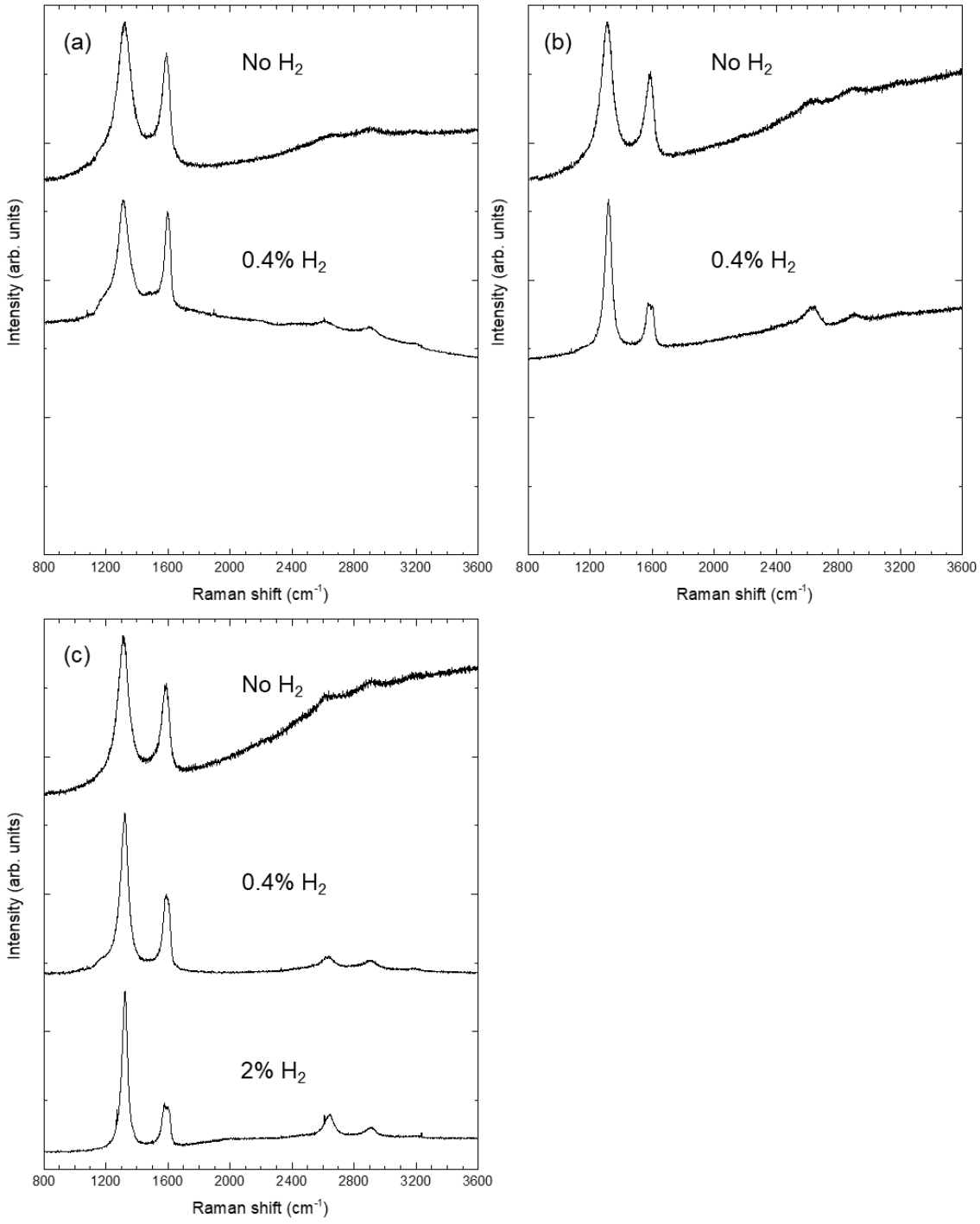

Figure 3-2. Raman spectra of powders synthesized with 1% CH_4 in Ar at (a) 50 W, (b) 125 W, and (c) 200 W applied power.

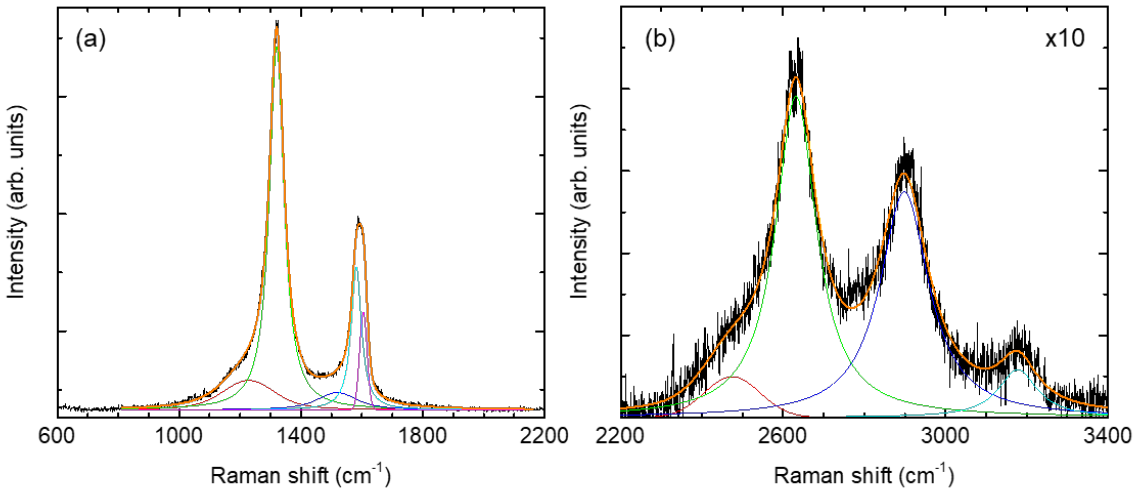

Figure 3-3. (a) First-order and (b) second-order fitted Raman spectra of powder synthesized with 1% CH_4 and 0.4% H_2 in Ar at 200 W.

An example of a fitted spectrum is shown in Figure 3-3. In addition to the D, G, and D' bands already mentioned, the fitting reveals the presence of two additional bands centered around 1225 and 1520 cm^{-1} in the first-order spectrum that are often associated with amorphous carbon.[17–19] Previously, Ferrari and Robertson have related the degree of crystallinity in carbon to spectral parameters of these features, specifically the integrated intensity ratio, I_D/I_G, and the position of the G band.[20] Here, we calculated $I_D/(I_G+I_{D'})$ ratio, where D' was added to the denominator to account for its contribution to the observed G peak in the raw spectra as recommended by Ferrari.[21] This parameter has been previously correlated with $1/L_a$ in relatively ordered graphite,[22] where L_a is crystallite size along the a-axis, and with L_a^2 in amorphous carbon with sp^3-coordination up to ~20%.[23] $I_D/(I_G+I_{D'})$ and G position for all of our carbon samples are plotted in Figures 3-4(a) and (b) as functions of applied power and H_2. The two quantities indicated that the collected material is close to 0% sp^3-coordination according to Ferrari and

Robertson's 'amorphization trajectory'[20] but are not found to follow any particular trend with the growth conditions. Indeed, Ferrari and Robertson note that in this region of amorphous carbon, a hysteresis exists which depends not only on sp^3/sp^2 ratio, but also on the configuration, *i.e.*, length and angle, of the sp^2 bonds.[23]

Previously, both Sadezky *et al.*[14] and Cuesta *et al.*[17] have shown the predictive power of the I_D/I_G ratio and G position to be limited in soot-like materials and instead found the full width half maximum of the D band ($FWHM_D$) to be a more reliable indicator of relative crystallinity. $FWHM_D$ of the carbon powders synthesized in this study are shown in Figure 3-4(c) and are found to follow a more consistent trend with applied power and H_2 concentration. Additionally, the full width half maximum of the 2D band ($FWHM_{2D}$) was found to closely follow $FWHM_D$, as shown in Figure 3-4(d). The presence of a narrow 2D band is a good sign of crystallinity, as it is a requisite feature of graphite and graphene samples.[21,24] Thus, the narrowing of the D and 2D bands with increasing power and increasing H_2 concentration point to longer-range graphitic ordering in the material. To support, TEM photos of two extremes, carbon synthesized at 50 W with no H_2, and at 200 W with 2% H_2, are shown in Figures 3-5(a-d). While both samples show evidence of graphitic planes, the latter of the two samples indeed shows ordering over a longer range. Concomitant with that, the material also appears to transition away from agglomerated particulate morphology toward highly disordered sheets.

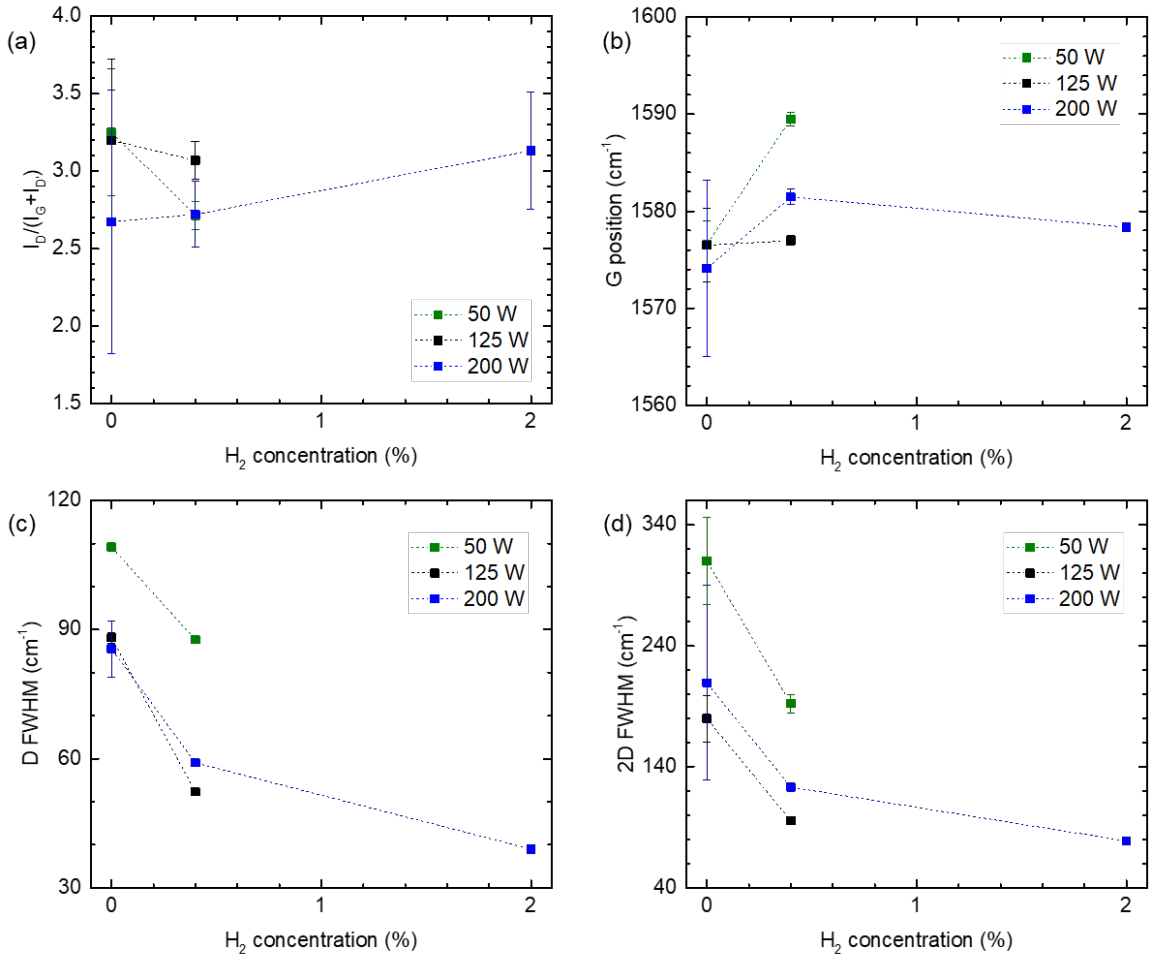

Figure 3-4. (a) $I_D/(I_G+I_{D'})$, (b) G position, (c) $FWHM_D$, and (d) $FWHM_{2D}$ extracted from fitting of Raman spectra of collected powders.

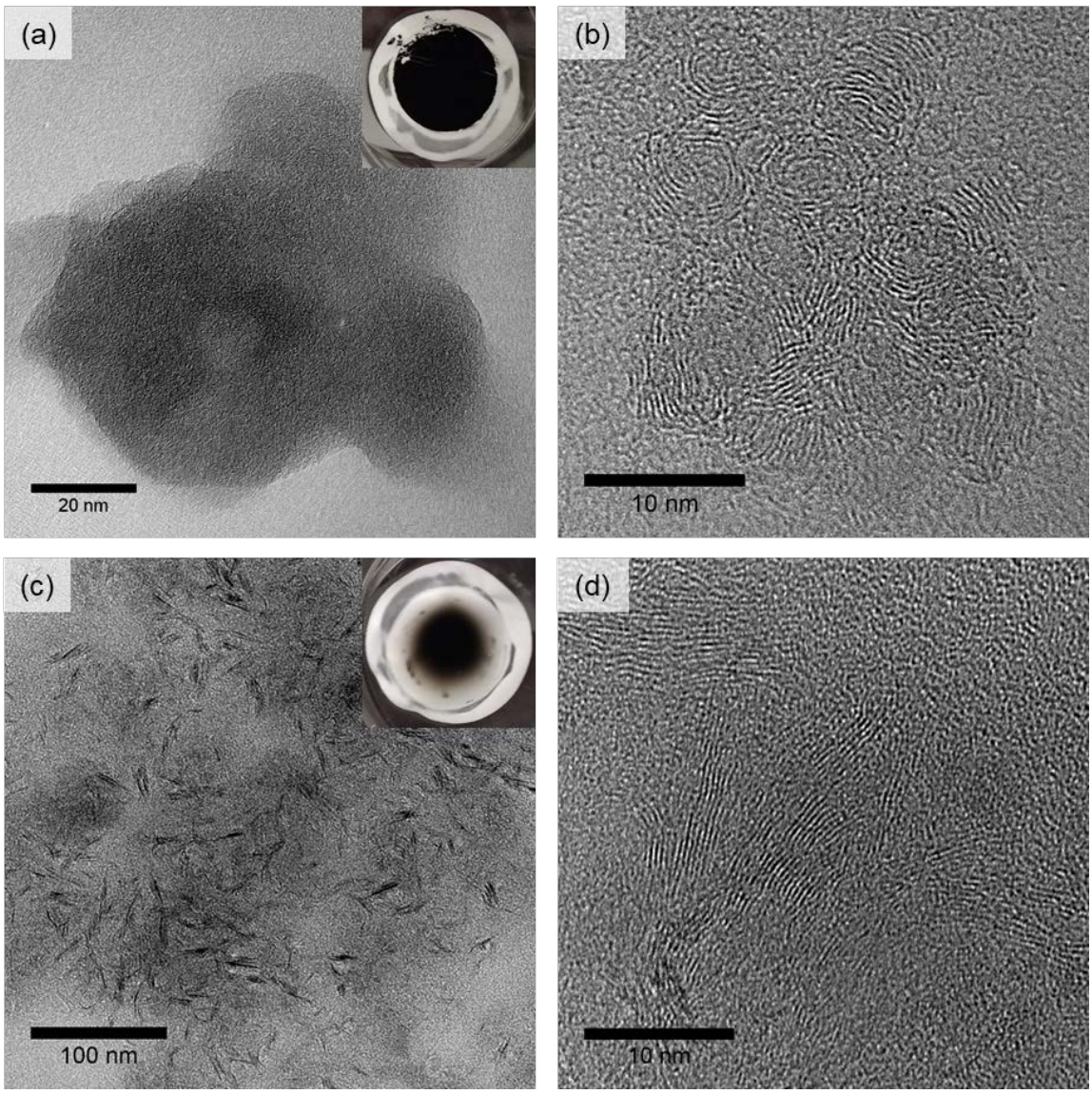

Figure 3-5. TEM images of powder synthesized with (a,b) no added H_2 at 50 W and (c,d) 2% H_2 at 200 W. Insets: photos of powder as collected on the filters.

We were limited in our growth to extending this trend out to higher H_2 concentrations. With increasing H_2 concentration, particle nucleation was found to decrease as shown in Figure 3-6. Particle formation could be recovered by concomitantly increasing power, but was limited to ~200 W, at which point excessive heating occurred. It is possible that further increases in H_2 concentration and power could eventually result

in crystalline carbon materials such as graphene sheets, which has previously been reported in surface microwave discharges at atmospheric pressure.[25,26] It is also possible that these more extreme conditions could lead to diamond growth, but we note that no evidence for diamond from Raman or TEM was observed in the range of growth conditions explored here. Indeed, Mitura's experiments, which resulted in diamond, were conducted at 3 kW of RF power.[8] The trend discovered here, with H_2 addition leading to greater sp^2 content instead of the other way around was unexpected and, to our knowledge, has not been previously reported in growth of carbon materials.

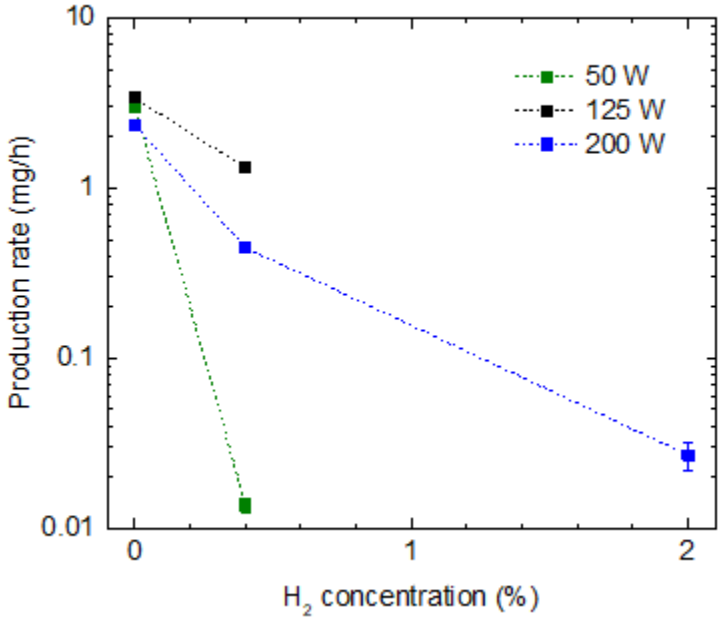

Figure 3-6. Production rates of synthesized powders.

3.3.2 *Seeding gas-phase synthesis of diamond by coinjecting SiH_4*

Silicon is known to be an excellent substrate for growth of diamond thin films by CVD.[15,27] We explored the possibility of synthesizing Si nanoparticles by homogeneous nucleation in the RF plasma reactor to similarly support diamond growth in the gas

phase, an approach that has also been attempted previously by Frenklach, *et al.*[11] We first confirmed the formation of Si nanoparticles from a mixture of 0.16% SiH_4 and 0.5% H_2 in Ar at 50 sccm total, 50 Torr, and 50 W. A representative Raman spectrum of the collected powder is shown in Figure 3-7(a), and the inset shows that the collected powder exhibits its signature yellow-orange color. A sharp peak appears at approximately 512 cm^{-1}, corresponding to crystalline Si, which is downshifted from its usual position at 520 cm^{-1}. This downshift is well known for nanoscale forms of Si[28,29] because of phonon confinement effects.[30,31] Additional peaks appear at 297 and 932 cm^{-1}, also corresponding to crystalline Si, and at 620 and 2093 cm^{-1}, which have been assigned to surface Si-H_x bonds.[32–34] The particles are thus confirmed to be of high quality.

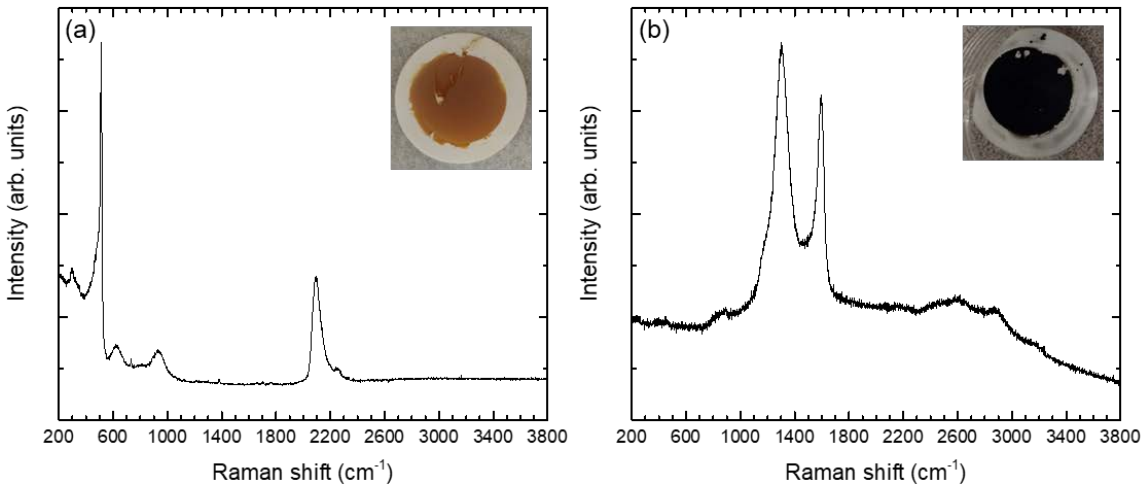

Figure 3-7. Raman spectra of powders synthesized with 0.16% SiH_4 and 0.5% H_2 (a) without CH_4 and (b) with 0.5% CH_4. Insets: photos of powder as collected.

We first studied the potential for Si nanoparticles to serve as seeds for diamond nucleation in a single step by coinjecting the Si precursor, SiH_4, and the carbon precursor, CH_4. H_2 and CH_4 concentrations were selected such that no nucleation was observed

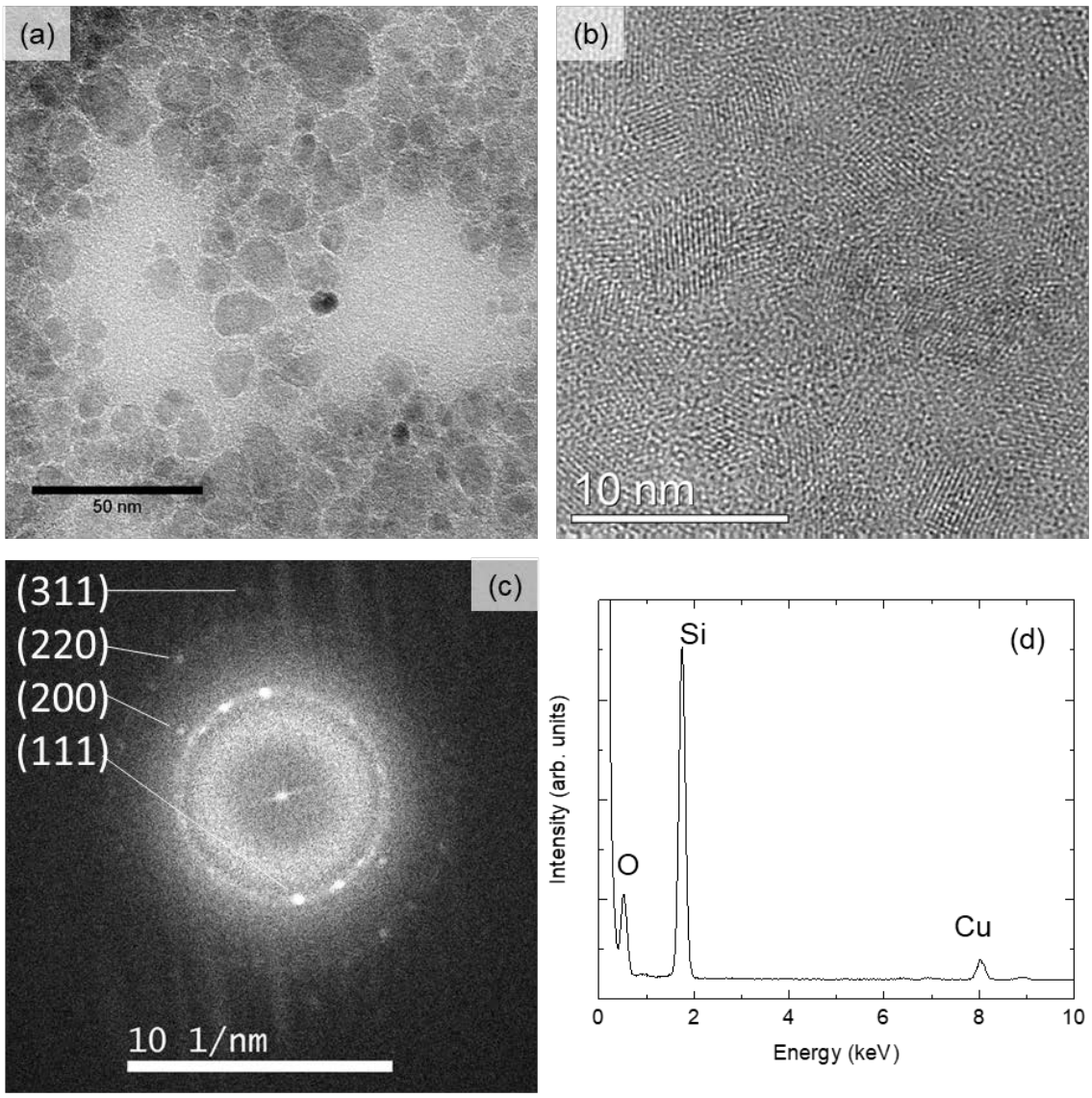

Figure 3-8. (a,b) HRTEM images of material synthesized with a mixture of 0.16% SiH_4, 0.5% H_2, and 0.5% CH_4. (c) FFT of image in (b) with diffraction spot assignments to crystal planes of 3C SiC. (d) EDS of specimen.

without the addition of SiH_4. This resulted in a black powder shown in the inset along with the collected Raman spectrum in Figure 3-7(b). The observed Raman peaks correspond to amorphous carbon and appear similar to those shown in Figure 3-2 in

Section 3.3.1. However, closer inspection of the sample by TEM reveals aggregated particles around 10-30 nm in diameter, shown in Figure 3-8(a). Higher resolution imaging in Figure 3-8(b) reveals crystallites with a domain size of about 3-5 nm. A fast Fourier transform (FFT) of the image, shown in Figure 3-8 (c), reveals lattice spacings measuring approximately 2.51, 2.21, 1.56, and 1.30 Å, which correspond well with the (111), (200), (220), and (311) reflections, respectively, of 3C SiC. These d spacings are generally shared with other common SiC polytypes, such as 4H and 6H, though no other d spacings expected for those polytypes were observed. No lattice spacings corresponding to diamond or Si were observed, and EDS, shown in Figure 3-8 (d), confirmed the only other element present in significant amount besides C was Si.

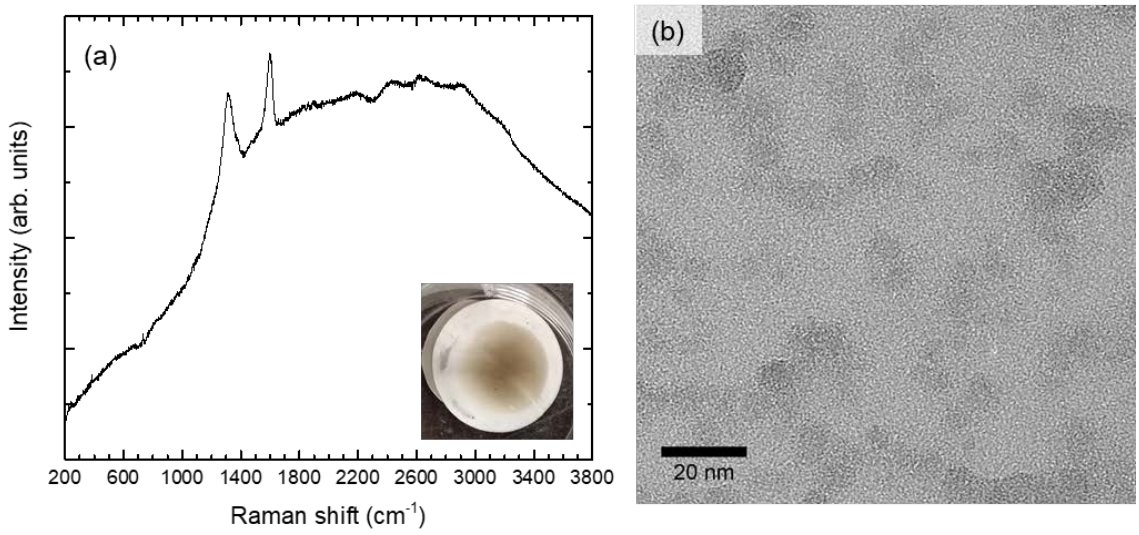

Figure 3-9. (a) Raman spectrum and (b) HRTEM image of material synthesized with 50 ppm SiH_4, 0.5% H_2, and 0.5% CH_4. Inset: photo of powder as collected.

A second sample was collected using the same gas mixture and same operating conditions but with a reduced amount of SiH_4, 50 ppm, which was the minimum

threshold found to produce any solid material at all. This resulted in a light brown powder which is shown along with the corresponding Raman spectrum in Figure 3-9(a). The observed Raman peaks again correspond to amorphous carbon, but superimposed on a strong PL background. Analysis by TEM revealed a particulate morphology, but no crystallinity was detected. This method of seeding, by simultaneous injection of SiH_4 with CH_4, thus appears to result in formation of either amorphous material at low SiH_4 or polycrystalline 3C SiC particles coated in amorphous carbon at high SiH_4. Results similar to the latter case have been reported previously in a very similar RF CCP reactor.[35,36] In those cases, achieving crystalline SiC was sometimes challenging without subsequent annealing. Modifying the process to include two steps instead of one, with the first step producing Si nanoparticles from SiH_4 in one plasma followed by injection of those particles along with a hydrocarbon gas into a second plasma, resulted in preservation of a Si core with a SiC or amorphous carbon outer layer.[37,38]

3.3.3 *Seeding diamond growth by MPCVD with RF plasma-produced Si nanoparticles*

To test the viability of seeding diamond growth by Si nanoparticles synthesized in our RF CCP reactor, we carried out CVD growth of diamond thin films in a microwave plasma reactor. Before testing the Si nanoparticles as seeds, diamond growth was verified using a standard seeding method by rubbing a slurry of detonation diamond powder (procured from Adamas Nanotechnologies) in ethanol onto the surface of the OFHC Cu gasket and then rinsing away all visible residue of powder with fresh ethanol. A photo of the film grown after 5.5 hours is shown in Figure 3-10(a), and the corresponding Raman spectrum is shown in Figure 3-10(b). The film itself was not very adherent, as expected

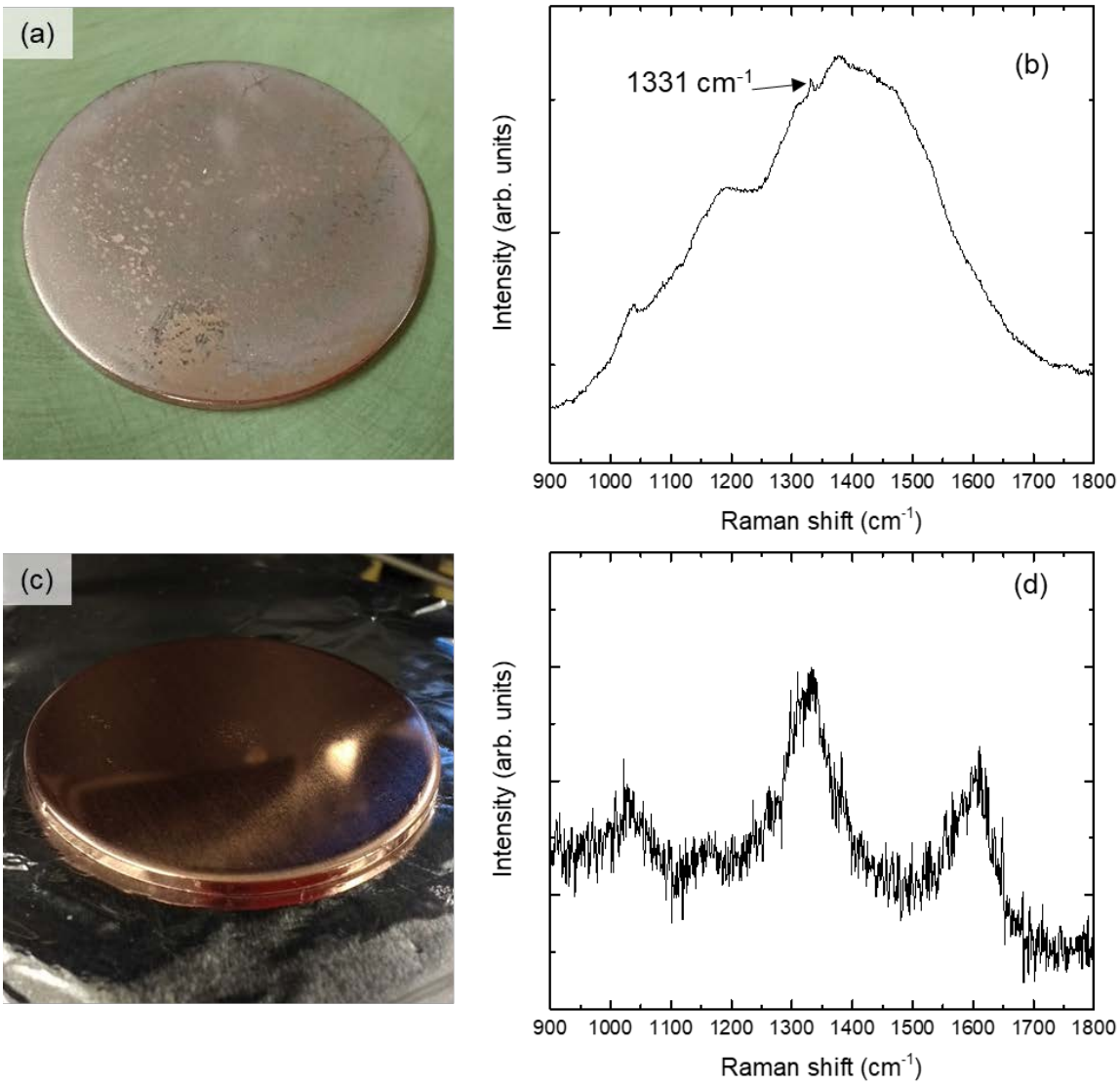

Figure 3-10. (a,b) Photo and Raman spectrum of diamond film grown in 5.5 hours on Cu after seeding with detonation diamond powder. (c,d) Photo and Raman spectrum of control sample that underwent the same treatment after only being rinsed in ethanol.

for growth on Cu.[15,27] The Raman spectrum contains a small peak at 1331 cm^{-1} that confirms diamond. The broad structure surrounding this peak, from around 900-1800 cm^{-1}, is common to most nanocrystalline diamond films and consists of a superposition of

D, G, and the so-called ν_1 and ν_3 bands.[20] The latter two bands correspond to trans-polyacetylene that likely occurs in grain boundaries along with amorphous or graphitic carbon. A control sample was also prepared using this same method by rubbing the OFHC Cu gasket with pure ethanol solvent, which only produced a thin layer of amorphous carbon, as shown by the photo in Figure 3-10(c) and confirmed by the Raman spectrum in Figure 3-10(d).

Samples with Si nanoparticles as seeds on OFHC Cu gasket before and after growth in the MPCVD chamber are shown in Figures 3-11(a) and (b), respectively, with their corresponding Raman spectra in Figure 3-11(c). A diamond film is clearly visible by eye after treatment; additionally, no Raman signatures of Si are present after treatment, though the Si film is still visible underneath the diamond film. Raman spectra of the film were taken at multiple points, labelled in Figure 3-11(b), corresponding to different concentrations of Si nanoparticles underneath the film. In all cases, a small diamond peak and the same broad features in the range 900-1800 cm^{-1} seen in Figure 3-10(b) are present. In addition, a fairly broad peak centered around 2264 cm^{-1} is present in all cases, albeit in varying intensity. This peak location corresponds to an emitted wavelength of 738 nm, which is the zero-phonon line of PL from silicon-vacancy (Si-V) defect centers.[39] The intensity of this peak correlates roughly with the concentration of Si nanoparticles underneath the diamond film.

These results indicate that not only can diamond nucleate on Si nanoparticles, but Si-V centers are also created this way. While Si-V centers in diamond grown on Si wafers has been previously reported[40] and has been explained by incorporation of Si atoms etched from the wafer itself or from other sources in the microwave chamber, to

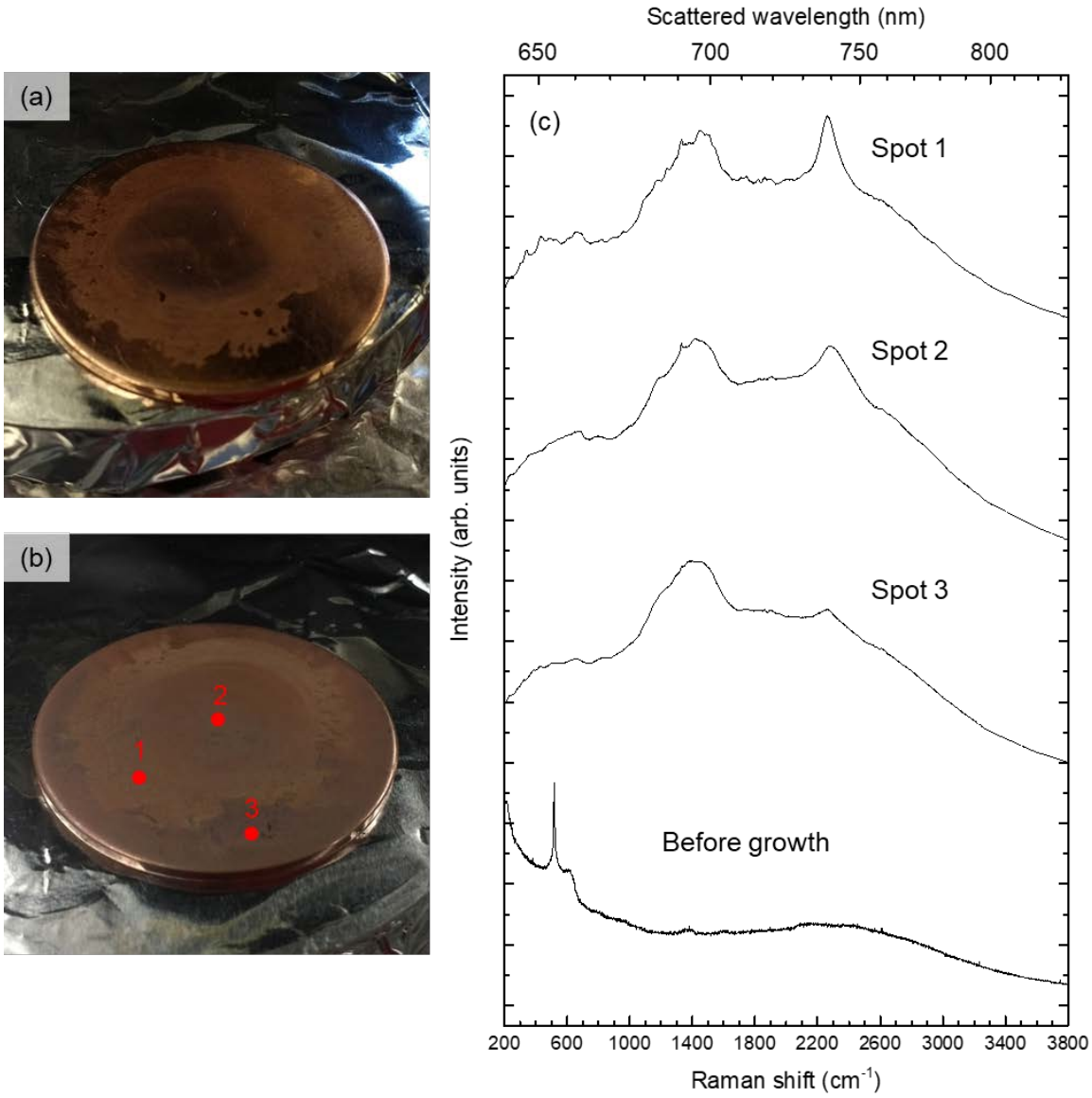

Figure 3-11. Cu gasket coated with a film of Si nanoparticles (a) before and (b) after treatment in the MPCVD chamber. (c) Raman spectra corresponding to points shown in (b).

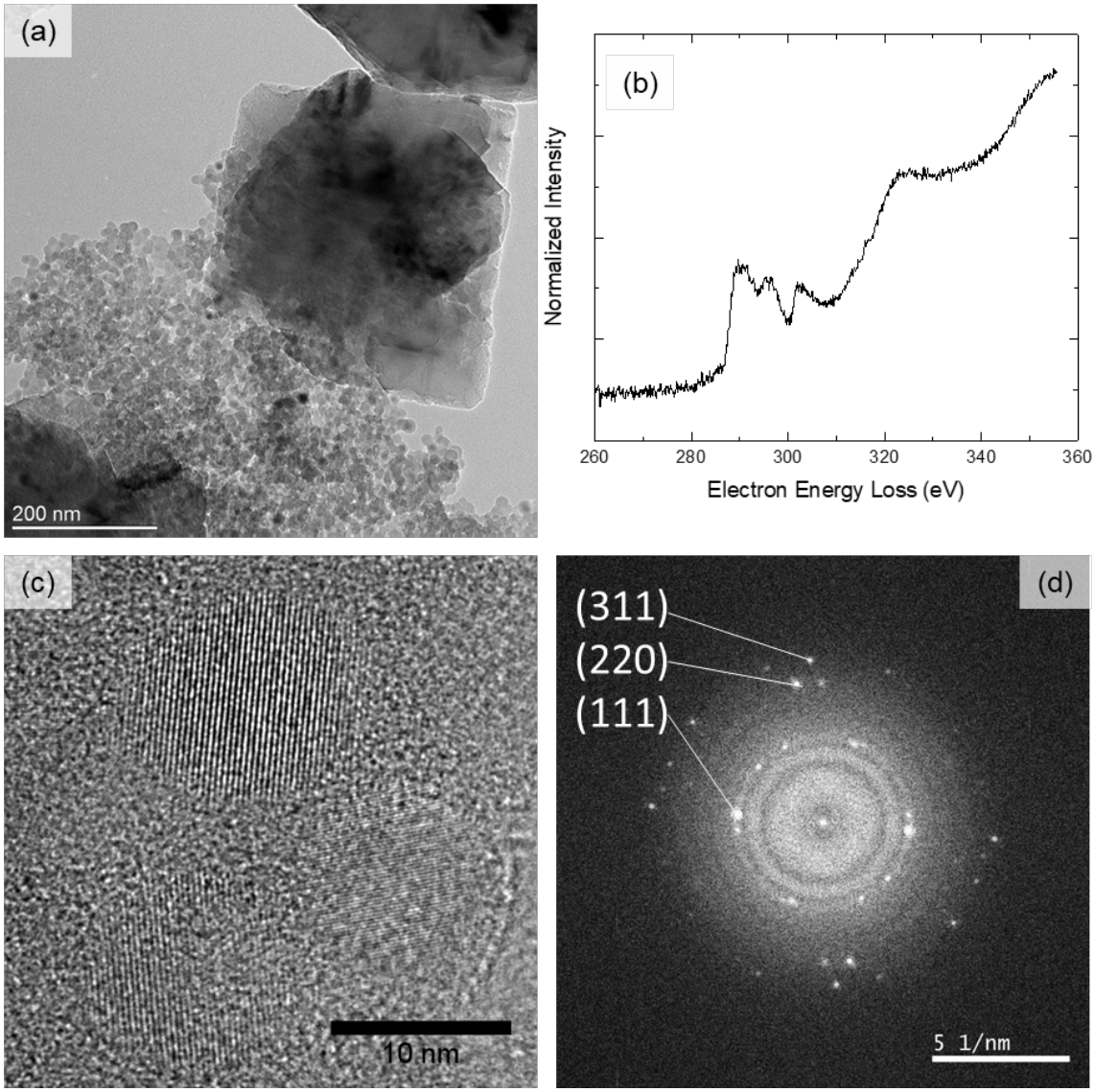

Figure 3-12. (a) TEM image of diamond crystals on top of a bed of Si nanoparticles. (b) EELS of a diamond crystal showing signature features of diamond. (c,d) HRTEM image and corresponding FFT of a cluster of 10 nm Si nanoparticles. Diffraction spots are assigned to crystal planes of cubic Si.

our knowledge this has not been demonstrated with Si nanoparticle seeds. A similar mechanism for Si incorporation in the diamond may also occur here, but we note that no Si atoms could be detected by OES of the microwave discharge during growth, and

incorporation of Si by diffusion into the diamond crystals is also possible. Future experiments are planned to address this question.

The film seeded by Si nanoparticles was found to be more adherent than the one seeded using detonation diamond but could still be removed easily from the substrate. TEM photos of a sample of film scraped from the Cu substrate are shown in Figure 3-12. Si nanoparticles about 10 nm in diameter and large diamond crystals several hundred nm in size are both visible, as shown in Figure 3-12(a). Electron energy loss spectroscopy (EELS) results shown in Figure 3-12(b) confirm that the large crystals are composed of diamond. In agreement with the Raman spectrum shown in Figure 3-7(a), the Si nanoparticles were found to be highly crystalline (see Figure 3-12(c)), even after MPCVD treatment, and also highly monodisperse. As shown in Figure 3-12(d), observed lattice spacings correspond well with the (111), (220), and (311) reflections of cubic Si.

We could not determine from the TEM images whether the diamond crystals grew from individual Si particles or whether they nucleated adjacent to them. An example photo of Si nanoparticles superimposed with a large diamond crystal is shown in Figure 3-13. Lattice spacings for both cubic Si and cubic diamond are identifiable, though whether the Si particles are inside the diamond crystal or simply underneath or on top is not clear. Lattice spacings corresponding to SiC, as might occur at the interface between Si and diamond,[15,27] were not observed. Some spacings between 1.40 and 1.50 Å are present, however, the origin of which could not be determined. Small diamond particles, on the order of 10 nm or so, could not be located.

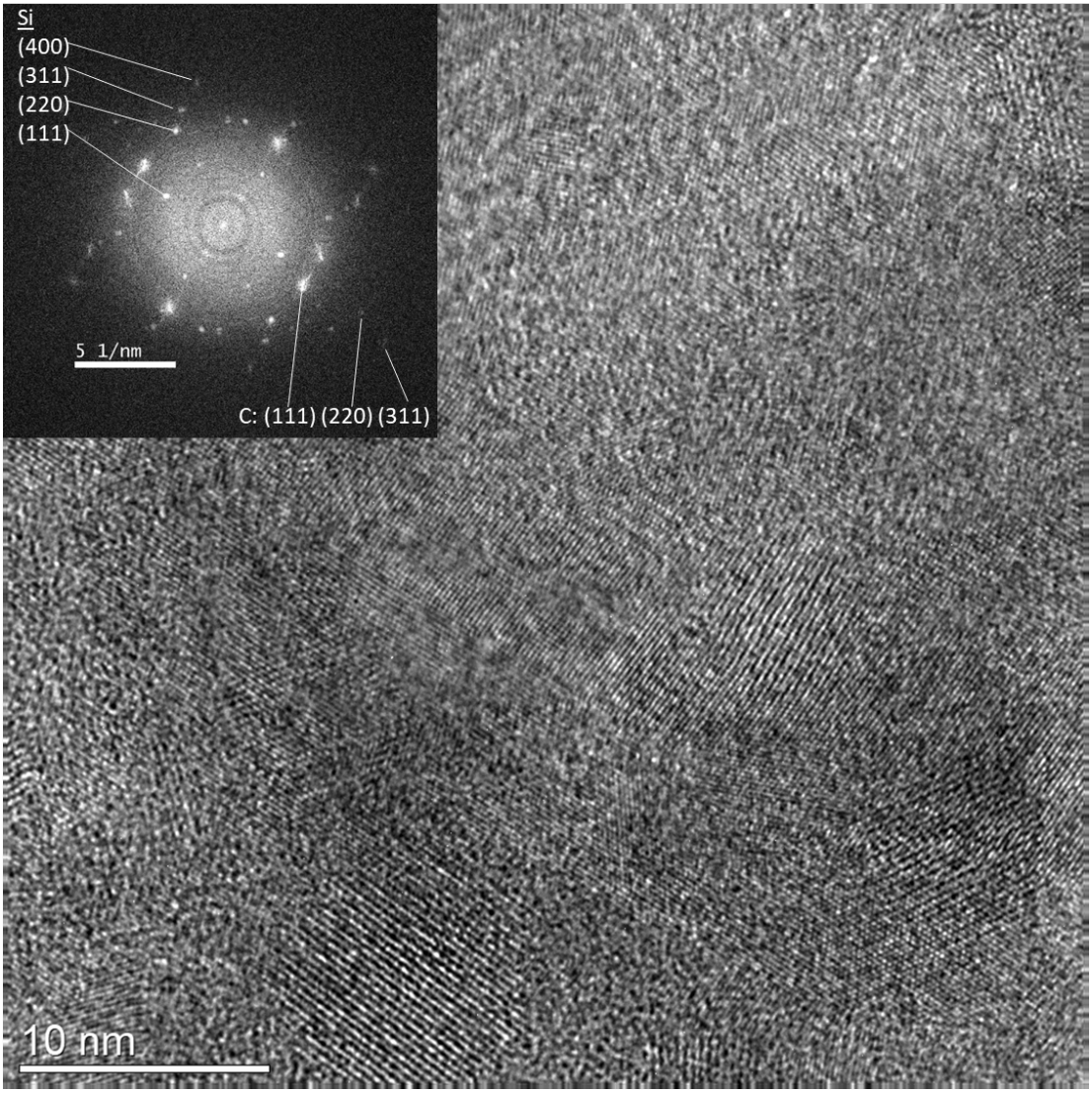

Figure 3-13. HRTEM image of Si nanoparticles superimposed with a large diamond crystal. FFT of the image (inset) shows evidence of both cubic Si and cubic diamond lattice spacings.

To test if the size of the diamond particles could be reduced, two more samples were prepared by the same method as above but with growth times of 30 minutes and 1 hour. The Raman spectra of both samples are shown in Figure 3-14. The resulting films

are thin enough that the primary Si peak is still detectable, but, interestingly, the signature features of nanocrystalline diamond are missing, and only the D and G bands of amorphous carbon are detected. We propose the following explanation for the lack of diamond at shorter growth times. One, the growth mechanism of the diamond film may require a layer of amorphous carbon to form as an initial step. Another explanation is that both amorphous carbon and diamond grow simultaneously, but after only an hour or less of growth time, only the amorphous carbon is detectable by Raman. As shown in Figure 3-10(d), the Cu surface itself will grow an amorphous carbon film under the applied conditions, but that film does not evolve into diamond at any point. Further studies are needed in order to understand fully how the diamond film grows on the Si nanoparticles and, from that, whether or not the size of the resulting diamond particles can be confined to the nanoscale (<10 nm).

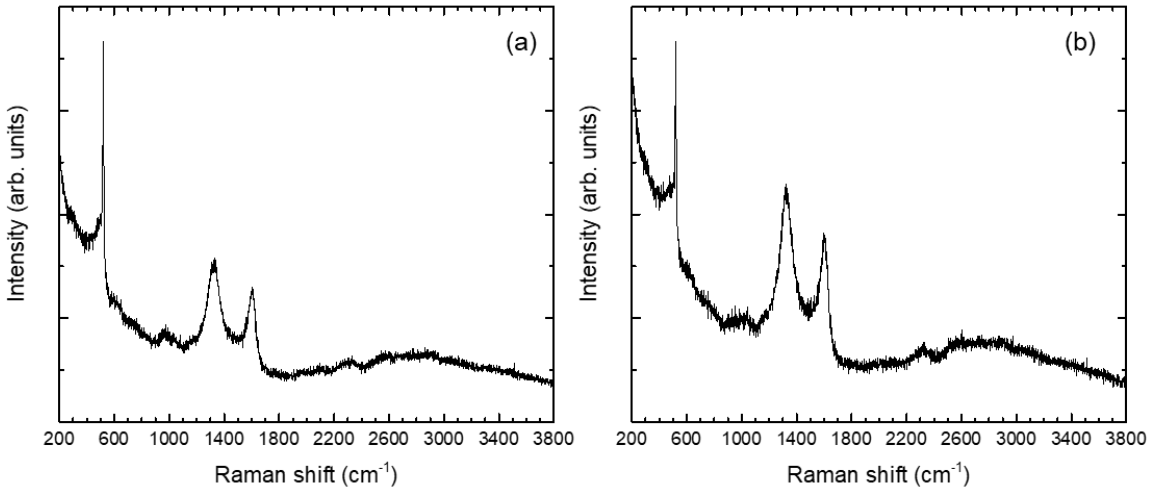

Figure 3-14. Raman spectra of films grown on Si nanoparticles after (a) 30 minutes and (b) 1 hour.

3.4 Conclusions and future work

Homogeneous nucleation of carbon material was achieved in a low pressure RF CCP reactor using a gas mixture of CH_4/H_2/Ar. Raman spectroscopy indicated the material was mostly amorphous, but with a low fraction of sp^3-coordinated bonds and, therefore, some short-range ordering that improved with increased H_2 concentration and applied power, as judged by the FWHM of the D and 2D bands. The material appeared by TEM to be heavily agglomerated with some ordered graphitic lattices in disordered configurations that were seen to evolve into crumpled sheets as power was increased and H_2 was added. However, the production rate of carbon material was found to decrease with increased H_2 concentration, necessitating higher applied powers to nucleate homogeneously. It's possible that this trend in morphology could continue, leading to homogeneous nucleation and growth of more ordered graphene-like sheets. However, this is opposite to the typical trend in CVD where increasing H_2 concentration promotes the formation of the diamond phase.

An alternative strategy to promote the formation of diamond was carried out by seeding with Si, which is well known to support diamond film growth by CVD. Introducing SiH_4 in the gas flow with CH_4 in close to equal ratio was found to produce 3C SiC particles coated in amorphous carbon. Reducing the SiH_4 led to less material grown and without any crystallinity. Modifying this strategy to include two synthesis steps instead of one may offer more promise for diamond growth. For example, Si nanoparticles could be synthesized in an RF CCP before being injected downstream into a second chamber for subsequent heterogeneous diamond growth. To test this idea, Si nanoparticles were used as seeds on Cu substrates for diamond film growth by MPCVD.

Large diamond particles on the order of 100 nm with inclusions of Si-V defect centers were obtained. While the exact mechanism of how the diamond first nucleates and then grows on the Si nanoparticles was not verified, the results show that Si nanoparticles, like a Si substrate, can help nucleate diamond and coincidentally produce Si-V centers. This strategy could be further extended to other nanoparticle materials (e.g., boron, nickel, etc.) to produce other types of defect centers as desired.

3.5 Acknowledgments

This work was conducted in collaboration with Dr. Abdurrahman Almethen and Dr. Philip Hemmer and was supported by NSF Grant No. CBET-1335990 and Columbus Nanoworks, Inc. We are grateful to Dr. John Angus and Dr. Heidi Martin for granting access to the Astex MPCVD chamber and to Dr. Cliff Hayman for assistance with operation. We are also grateful to Dr. Hatsuo Ishida for granting access to Raman spectroscopy and to Dr. Danqi Wang for assistance with TEM.

3.6 References

1. Lopez, T. & Mangolini, L. Low activation energy for the crystallization of amorphous silicon nanoparticles. *Nanoscale* **6,** 1286–94 (2014).

2. Ahadi, A. M. *et al.* Controlled synthesis of germanium nanoparticles by nonthermal plasmas. *Appl. Phys. Lett.* **108,** 93105 (2016).

3. Zhang, H. *et al.* Doped Silicon Nanocrystal Plasmonics. *ACS Photonics* **4,** 963–970 (2017).

4. Zhou, S. *et al.* Boron- and Phosphorus-Hyperdoped Silicon Nanocrystals. *Part.*

Part. Syst. Charact. **32,** 213–221 (2015).

5. Zhou, S. *et al.* Ligand-Free, Colloidal, and Plasmonic Silicon Nanocrystals Heavily Doped with Boron. *ACS Photonics* **3,** 415–422 (2016).

6. Robertson, J. Diamond-like amorphous carbon. *Mater. Sci. Eng. R* **37,** 129–281 (2002).

7. Matsumoto, S. Development of diamond synthesis techniques at low pressures. *Thin Solid Films* **368,** 231–236 (2000).

8. Mitura, S. Nucleation of diamond powder particles in an RF methane plasma. *J. Cryst. Growth* **80,** 417–424 (1987).

9. Frenklach, M. *et al.* Homogeneous nucleation of diamond powder in the gas phase. *J. Appl. Phys.* **66,** 395–399 (1989).

10. Howard, W. *et al.* Synthesis of diamond powder in acetylene oxygen plasma. *J. Appl. Phys.* **68,** 1247–1251 (1990).

11. Frenklach, M. *et al.* Induced nucleation of diamond powder. *Appl. Phys. Lett.* **59,** 546–548 (1991).

12. De Bleecker, K., Bogaerts, A. & Goedheer, W. Detailed modeling of hydrocarbon nanoparticle nucleation in acetylene discharges. *Phys. Rev. E* **73,** 26405 (2006).

13. De Bleecker, K., Bogaerts, A. & Goedheer, W. Aromatic ring generation as a dust precursor in acetylene discharges. *Appl. Phys. Lett.* **88,** 151501 (2006).

14. Sadezky, A., Muckenhuber, H., Grothe, H., Niessner, R. & Poschl, U. Raman microspectroscopy of soot and related carbonaceous materials: Spectral analysis

and structural information. *Carbon N. Y.* **43,** 1731–1742 (2005).

15. Gracio, J. J., Fan, Q. H. & Madaleno, J. C. Diamond growth by chemical vapour deposition. *J. Phys. D. Appl. Phys.* **43,** 374017 (2010).

16. Casiraghi, C., Piazza, F., Ferrari, A. C., Grambole, D. & Robertson, J. Bonding in hydrogenated diamond-like carbon by Raman spectroscopy. *Diam. Relat. Mater.* **14,** 1098–1102 (2005).

17. Cuesta, A., Dhamelincourt, P., Laureyns, J., Martinez-Alonso, A. & Tascon, J. Raman microprobe studies on carbon materials. *Carbon N. Y.* **32,** 1523–1532 (1994).

18. Jawhari, T., Roid, A. & Casado, J. Raman spectroscopic characterization of some commercially available carbon black materials. *Carbon N. Y.* **33,** 1561–1565 (1995).

19. Dippel, B., Jander, H. & Heintzenberg, J. NIR FT Raman spectroscopic study of flame soot. *Phys. Chem. Chem. Phys.* **1,** 4707–4712 (1999).

20. Ferrari, A. C. & Robertson, J. Raman spectroscopy of amorphous, nanostructured, diamond-like carbon, and nanodiamond. *Philos. Trans. R. Soc. London A* **362,** 2477–2512 (2004).

21. Ferrari, A. C. Raman spectroscopy of graphene and graphite: Disorder, electron-phonon coupling, doping and nonadiabatic effects. *Solid State Commun.* **143,** 47–57 (2007).

22. Tuinstra, F. & Koenig, J. L. Raman Spectrum of Graphite. *J. Chem. Phys.* **53,**

1126–1130 (1970).

23. Ferrari, A. C. & Robertson, J. Interpretation of Raman spectra of disordered and amorphous carbon. *Phys. Rev. B* **61,** 14095–14107 (2000).

24. Pimenta, M. A. *et al.* Studying disorder in graphite-based systems by Raman spectroscopy. *Phys. Chem. Chem. Phys.* **9,** 1276–1291 (2007).

25. Dato, A. & Frenklach, M. Substrate-free microwave synthesis of graphene: Experimental conditions and hydrocarbon precursors. *New J. Phys.* **12,** 125013 (2010).

26. Tsyganov, D. *et al.* On the plasma-based growth of 'flowing' graphene sheets at atmospheric pressure conditions. *Plasma Sources Sci. Technol.* **25,** 15013 (2016).

27. Das, D. & Singh, R. N. A review of nucleation, growth and low temperature synthesis of diamond thin films. *Int. Mater. Rev.* **52,** 29–64 (2007).

28. Yasar-Inceoglu, O., Lopez, T., Farshihagro, E. & Mangolini, L. Silicon nanocrystal production through non-thermal plasma synthesis: a comparative study between silicon tetrachloride and silane precursors. *Nanotechnology* **23,** 255604 (2012).

29. Ding, Y. *et al.* A parametric study of non-thermal plasma synthesis of silicon nanoparticles from a chlorinated precursor. *J. Phys. D. Appl. Phys.* **47,** 485202 (2014).

30. Iqbal, Z. & Veprek, S. Raman scattering from hydrogenated microcrystalline and amorphous silicon. *J. Phys. C Solid State Phys.* **15,** 377–392 (1982).

31. Ossadnik, C., Veprek, S. & Gregora, I. Applicability of Raman scattering for the characterization of nanocrystalline silicon. *Thin Solid Films* **337,** 148–151 (1999).

32. Liu, F.-M., Ren, B., Yan, J.-W., Mao, B.-W. & Tian, Z.-Q. Initial Oxidation Processes on Hydrogenated Silicon Surfaces Studied by In Situ Raman Spectroscopy. *J. Electrochem. Soc.* **149,** G95–G99 (2002).

33. Ma, Y., Huang, Y. L., Düngen, W., Job, R. & Fahrner, W. R. Hydride formation on the platelet inner surface of plasma-hydrogenated crystalline silicon investigated with Raman spectroscopy. *Phys. Rev. B* **72,** 85321 (2005).

34. Wang, J. *et al.* A comparative Raman spectroscopy study on silicon surface in HF , HF/H2O2 and HF/NH4F aqueous solutions. *Mater. Sci. Eng. B* **72,** 193–196 (2000).

35. Vivet, F., Bouchoule, A. & Boufendi, L. Synthesis and characterization of SiC:H ultrafine powder generated in an argon-silane-methane low-pressure radio-frequency discharge. *J. Appl. Phys.* **83,** 7474–7481 (1998).

36. Viera, G., Costa, J., Roura, P. & Bertran, E. High nucleation rate in pure SiC nanometric powder by a combination of room temperature plasmas and post-thermal treatments. *Diam. Relat. Mater.* **8,** 364–368 (1999).

37. Coleman, D., Lopez, T., Yasar-Inceoglu, O. & Mangolini, L. Hollow silicon carbide nanoparticles from a non-thermal plasma process. *J. Appl. Phys.* **117,** 193301 (2015).

38. Chaukulkar, R. P. *et al.* Single-step plasma synthesis of carbon-coated silicon

nanoparticles. *ACS Appl. Mater. Interfaces* **6,** 19026–19034 (2014).

39. Aharonovich, I., Greentree, A. D. & Prawer, S. Diamond photonics. *Nat. Photonics* **5,** 397–405 (2011).

40. Vlasov, I. I. *et al.* Nanodiamond Photoemitters Based on Strong Narrow-Band Luminescence from Silicon-Vacancy Defects. *Adv. Mater.* **21,** 808–812 (2009).

Chapter 4: Synthesis of amorphous and onion-like carbon nanoparticles in an atmospheric-pressure RF microplasma

4.1 Introduction

For any type of plasma reactor, the voltage required for gas breakdown scales with the product of pressure p and electrode gap distance d.[1] Thus, as gas pressure is scaled higher, the size of the plasma must be scaled down accordingly in order to maintain feasible breakdown voltages. Atmospheric pressure operation offers several advantages including ease of operation and lower cost by eliminating vacuum equipment, possibility of integration with SMPS systems to monitor particle formation,[2] and higher power densities which could lead to more precursor dissociation and heating for crystallization of materials. Similar to their low pressure analogue, RF CCPs at atmospheric pressure have typically been used in the parallel plate geometry for the purpose of thin film deposition.[3] Specifically, this configuration has been used for surface deposition of carbon nanotubes and nanofibers.[4,5] In these processes, while the higher pressure aids in reducing operating cost, it also increases the likelihood of dust formation. For deliberate synthesis of nanoparticles, atmospheric pressure RF CCPs, both in a ring-electrode configuration, like in the previous chapter, and parallel plate configuration have been employed previously for the synthesis of Si and SiC.[6,7]

In the first part of this study, carbon nanoparticles are synthesized homogeneously in an atmospheric pressure RF CCP with a ring-electrode configuration. In contrast with the DC microplasma tested in Chapter 2, this configuration eliminates contact between the plasma and metal electrodes. Particle morphology is studied by Raman spectroscopy and

TEM as a function of precursor molecule, H_2 addition, and applied power. In the second part of this study, phenomena occurring at high power densities are examined. Specifically, at high power, a filament composed of dendritic carbon was found to grow from the quartz wall underneath the high voltage electrode, and the interaction of the plasma with this filament was found to produce an aerosol of onion-like, or fullerenic,[8] carbon nanoparticles (OLC). Carbon dendrite formation has been reported previously in other atmospheric pressure plasma discharges involving organic precursors,[9–11] although no ejection of OLC was observed in those cases. Production of OLC *via* RF plasma sputtering of carbonaceous targets has also been reported,[12] but with limited control over the process.

4.2 Experimental design

The experimental setup was nearly identical to the one used in Chapter 2 (see Figure 2-1), with the primary exception being the reactor itself, a schematic of which is shown in Figure 4-1. The reactor is essentially a smaller version of the low pressure RF CCP used in Chapter 3, except that the clear-fused quartz tube has an OD of 0.12" and a wall thickness of 0.04". Power was coupled to the gas discharge *via* brass rings 1/8" wide and 0.6" thick, separated by a distance of ½" and positioned on the quartz tube so that the plasma would not contact the metal fittings on either end of the tube. The same RF power supply and matching network were used to sustain the plasma as the low pressure RF CCP, but the voltage was not high enough to initiate gas breakdown. Therefore, a third electrode was added to the reactor to which the high voltage lead of a second power supply (Information Unlimited model PVM500) capable of outputting kV of potential at kHz frequency was attached. Both power supplies shared a ground through the middle of the three electrodes,

as shown in Figure 4-1. An RF discharge could be ignited by first setting the amplitude of the RF power supply to an arbitrary value and then increasing the amplitude of the kHz power supply until a discharge initiated. At this point, the kHz power supply could be shut off, and the RF discharge was self-sustaining. The total volumetric flow rate was held constant at 100 sccm for all experiments, unless otherwise specified. Aside from the reactor, the only other change made to the experimental setup was the addition of an H_2 gas stream, controlled by a thermal MFC, which was directed along with the carrier Ar stream through the liquid bubbler. Calculation of organic precursor concentration by Equation 2.1 was adjusted accordingly.

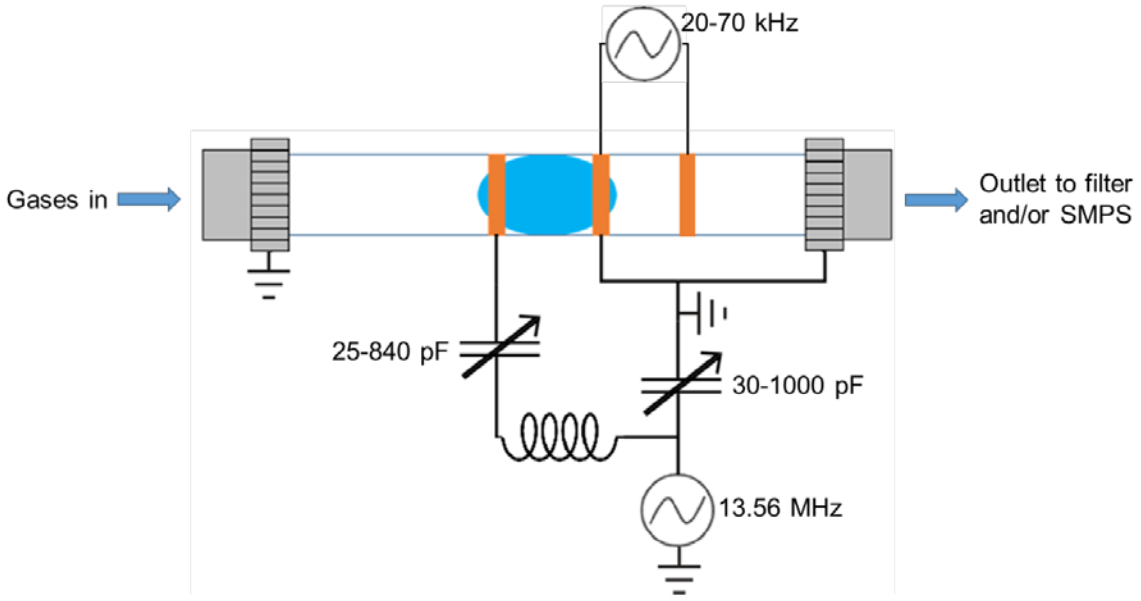

Figure 4-1. Schematic of the atmospheric pressure RF CCP reactor.

Particle collection and diagnostics by SMPS followed the same procedure outlined in Chapter 2, and fitting analysis by Raman spectroscopy followed the same procedure outlined in Chapter 3. For TEM analysis, particle specimens were deposited directly out of

the gas stream onto a TEM grid (Ted Pella, Inc. 01824) taped to a small disk electrode inside an electrostatic precipitation device (TSI, Inc. Model 3089) for times of a few minutes to 30 min.

4.3 Results and discussion

4.3.1 *Homogeneous synthesis and characterization of amorphous carbon particles*

PSDs of carbon nanoparticles synthesized from MeOH and EtOH vapor in the atmospheric-pressure RF CCP in Ar at varying applied power and H_2 concentration are shown in Figure 4-2. The concentrations of MeOH and EtOH precursor used, 0.9% and 0.45%, respectively, were chosen so that the mass input rate of carbon would be equal

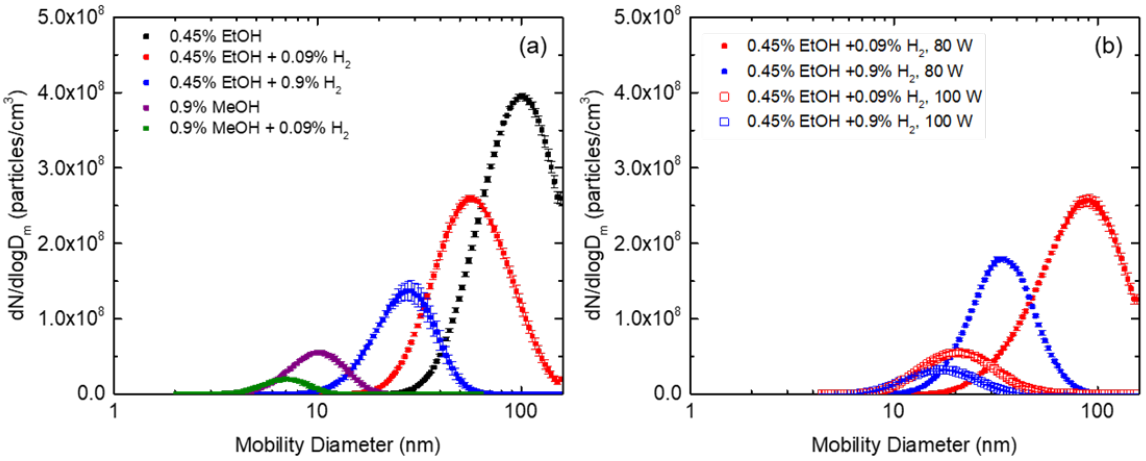

Figure 4-2. SMPS measurements of particles synthesized from EtOH and MeOH at (a) 60 W and (b) greater than 60 W.

in both cases. In the case of MeOH in particular, concentrations lower than 0.9% did not nucleate particles at all. Indeed, as shown in Figure 4-2(a), and similar to what was found in Chapter 2, MeOH is much less effective at nucleating particles than EtOH. In both cases,

adding H_2 was found to decrease the PSD peak and total number concentration of particles, in agreement with previous observations in the DC microplasma reactor.[13] Curiously, at applied power both below and above 60 W, MeOH did not produce any detectable particles, while EtOH produced particles with the PSD peak and particle number concentration increasing between 60 and 80 W, and then decreasing significantly between 80 and 100 W, indicating the presence of some factor that consumes or otherwise inhibits particle growth at high enough power. Without any added H_2, 0.45% EtOH was found to produce an excessive amount of particles in the reactor at powers greater than 60 W and rapidly generated a film on the reactor wall between the two electrodes.

Raman spectra of collected powders are shown in Figure 4-3. In general, the spectra appear very similar to the material produced by the low pressure RF discharge in Chapter 3 (see Figure 3-2); from the same analysis in that chapter, it can be surmised that the carbon materials produced in the atmospheric pressure RF discharge are also close to 0% sp^3-coordinated but contain many irregularities in bond configuration. In this case, however, the addition of H_2 does not have as strong or as consistent of an effect on the morphology. Instead, the biggest influence on structure comes from applied power. At 80 and 100 W, the spectra show a narrowing of the D and G bands, the height of the D band with respect to the G band increases, and the 2D band becomes prominent. The spectra appear to converge to a very similar shape as that seen in Chapter 3 at high H_2 content and high power. In this case, however, a lower power was needed to reach the same morphology, most likely due to the smaller plasma volume, and therefore higher power density, of the atmospheric pressure plasma.

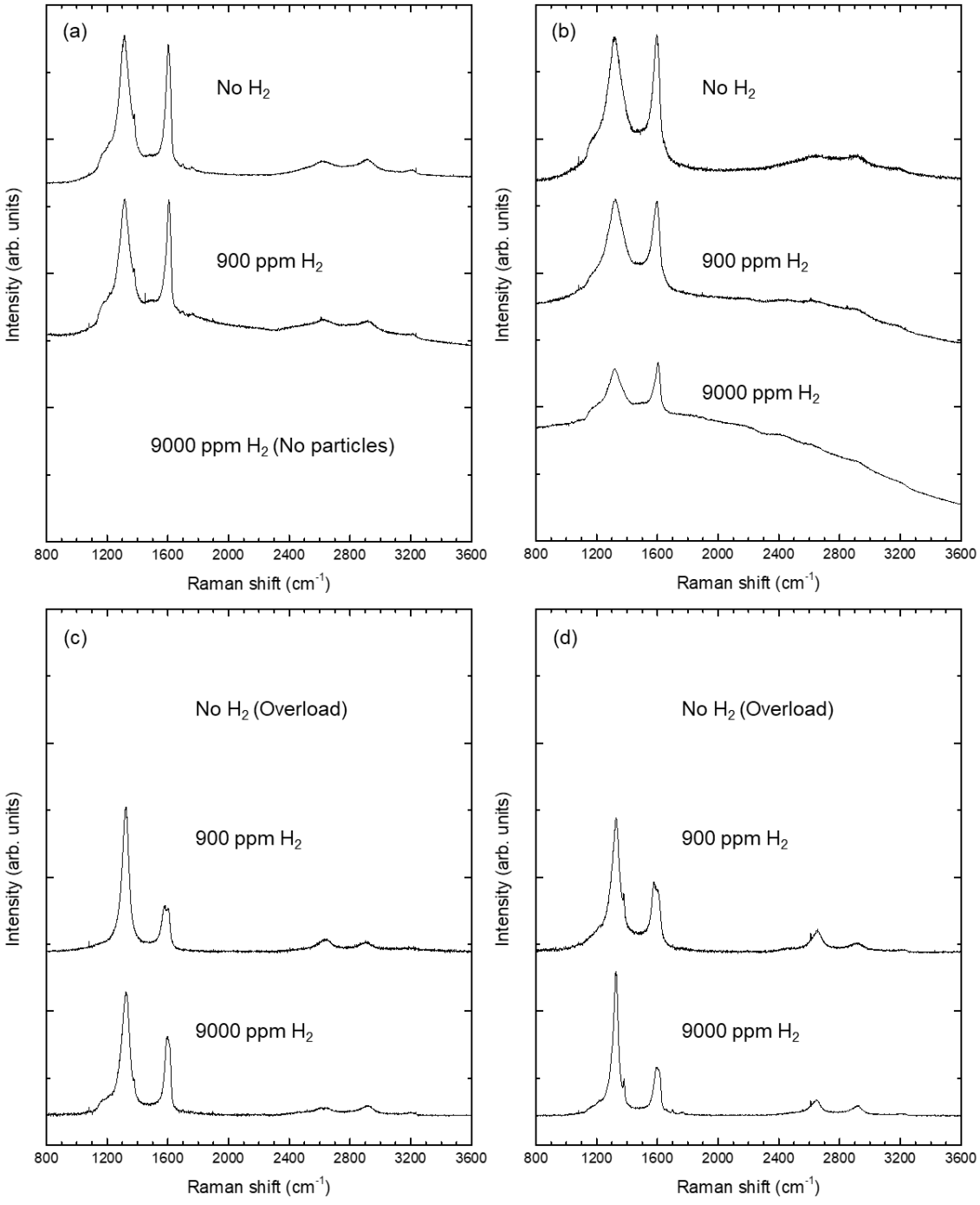

Figure 4-3. Raman spectra of powders synthesized with (a) MeOH at 60 W, (b) EtOH at 60 W, (c) EtOH at 80 W, and (d) EtOH at 100 W.

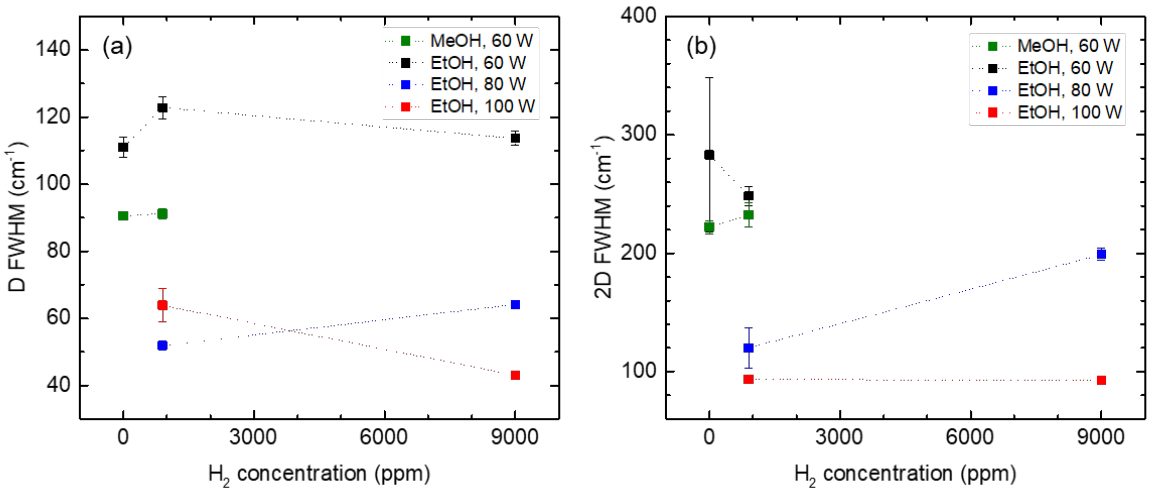

Figure 4-4. FWHM of (a) D and (b) 2D bands from powders synthesized with EtOH and MeOH ($FWHM_{2D}$ of the sample made with 0.45% EtOH and 0.9% H_2 at 60 W could not be accurately determined due to fluorescence background).

Analysis by background subtraction and peak fitting, as described in Chapter 3, was carried out on the spectra. The FWHM of the D and 2D bands of each material are plotted in Figure 4-4, so that trends in the material's relative degree of crystallinity can be more easily visualized. In addition to a significant difference between 60 W and above 60 W for EtOH, the two precursors themselves, EtOH and MeOH, also show a significant difference at otherwise equivalent conditions, with MeOH forming slightly more crystalline material.

Representative TEM images of material produced from 0.9% MeOH at 60 W and 0.45% EtOH with 0.9% H_2 at 80 W are shown in Figures 4-5(a) and (b), respectively. In contrast with the sample preparation method utilized in the previous two chapters, here, the *in situ* deposition onto each TEM grid allows visualization of the particles as they would appear in the aerosol stream without additional agglomeration. The individual particles, on the order of 10 nm in size, show a relative difference in degree of crystallinity that agrees

with their $FWHM_D$ in Figure 4-4(a). The particle in Figure 4-5(b) in particular shows signs of the same ribbon-like structures observed in Figure 3-5(d). As in Chapter 3, no evidence of diamond-phase carbon was observed, making this material distinct from that found by the DC microplasma in Chapter 2, even though atmospheric pressure operation was also used.

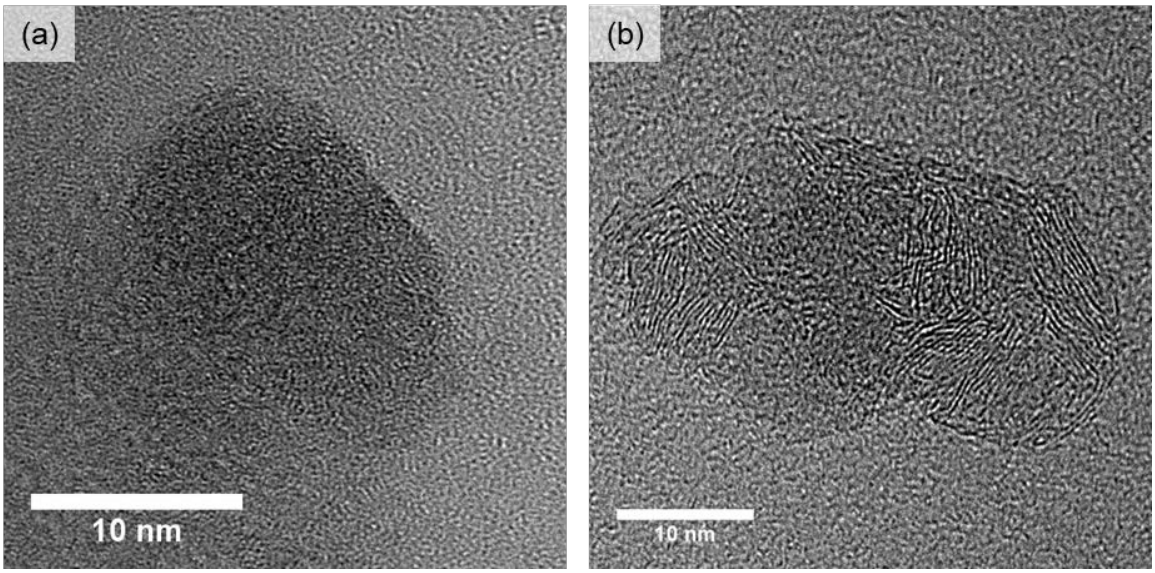

Figure 4-5. TEM images of individual particles made from (a) 0.9% MeOH at 60 W and (b) 0.45% EtOH and 0.9% H_2 at 80 W.

4.3.2 *Onion-like carbon particle synthesis by ejection from dendritic filaments*

At all of the examined conditions, growth of a carbon film occurred on the reactor wall to some extent, particularly underneath the high voltage electrode. As previously mentioned, at higher than 60 W, 0.45% EtOH without any added H_2 rapidly grew a film that occluded the inner quartz wall between the electrodes and short-circuited the plasma. In the case of 0.9% MeOH at up to 100 W, no such rapid growth occurred, nor were any homogeneously nucleated particles observed. Once power was increased to at least 130-

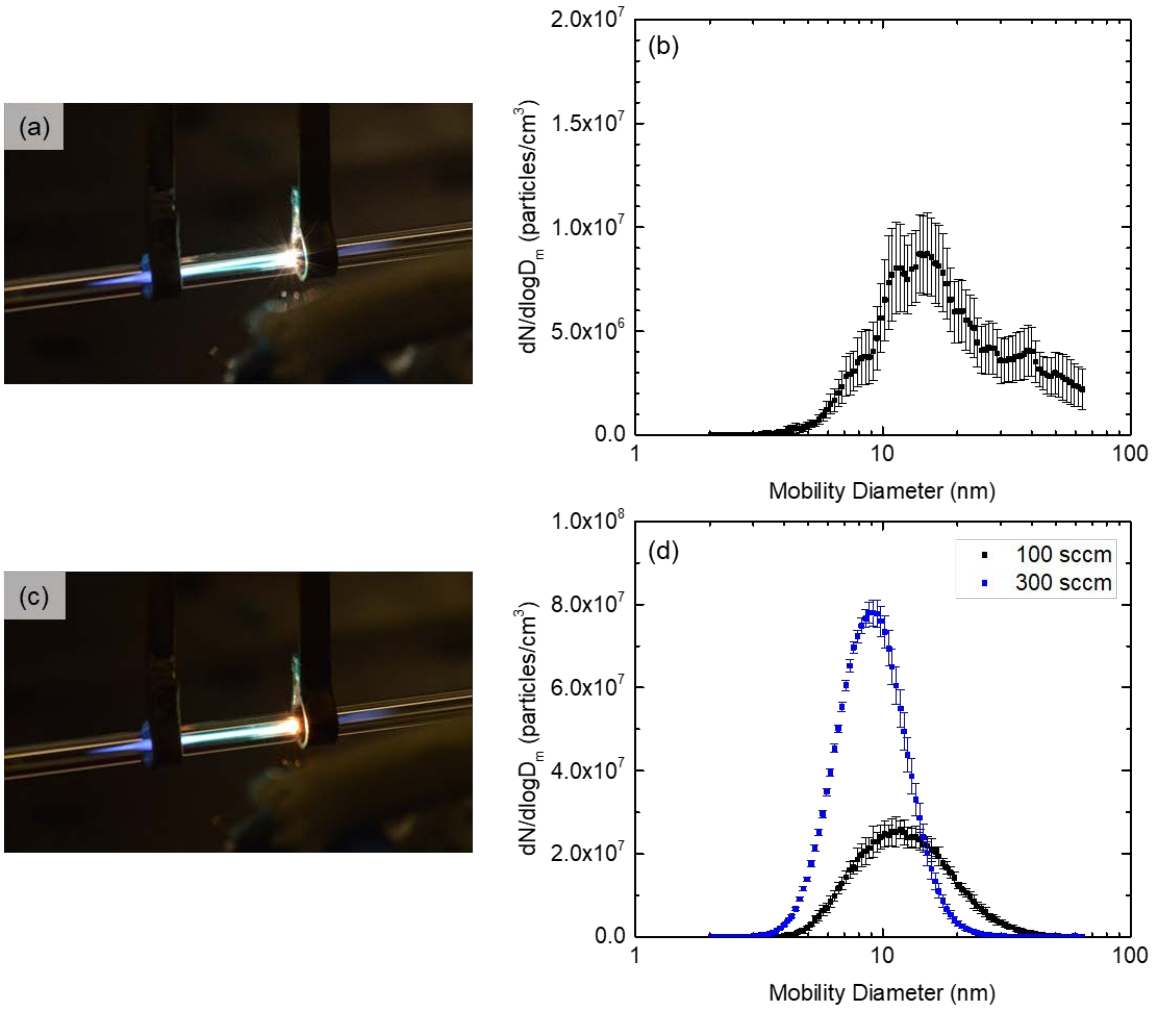

Figure 4-6. Photos of the reactor and SMPS scans of (a,b) unsteady operation with 0.9% MeOH at 130-140 W and (c,d) steady operation at 100 W after allowing the filament to grow for some time.

140 W, however, a bright flashing of white light was observed underneath the high voltage electrode, accompanied by the generation of particles, as measured by the SMPS. A photo of the reactor under these conditions is shown in Figure 4-6(a), along with the resulting PSD in Figure 4-6(b). The PSD did not converge to a particular shape in this operating mode. Over time, a filament centered along the reactor's axis was observed to grow from

underneath the high voltage electrode in the direction of the grounded electrode, with bright incandescence occurring at the interface of the plasma with the filament. After some growth of the filament, power was reduced back to 100 W, resulting in a more stable, bright orange incandescence, as well as a stable PSD, shown in Figures 4-6(c) and (d).

In this mode, the PSD was not significantly sensitive to changes in power, MeOH concentration, or H_2 concentration. Increasing volumetric flow rate to 300 sccm, however, resulted in a shift of the PSD center to a smaller diameter along with an increase in PSD height, as shown in Figure 4-6(d). The Raman spectrum and a representative TEM image of the particles produced at 100 sccm are shown in Figures 4-7(a) and (b). The spectrum for this particle growth mode shows a G band much higher in intensity than the D band, in contrast with the spectra in Figure 4-3, suggesting an even higher degree of crystallinity. In Ferrari and Robertson's 'amorphization trajectory,'[14] this would correspond to a cross-over from amorphous carbon to nanocrystalline graphite. Indeed, TEM imaging, shown in Figure 4-7(b), reveals small particles of OLC around 5 nm in diameter. No other particle morphologies were observed in the TEM sample, aside from some nano-rods, also shown in Figure 4-7(b), indicating good product homogeneity. Most, though not all, of the OLC particles appeared to be hollow with some visible structural disordering in the spherical layers. The OLC particles were also sensitive to the electron beam and significantly degraded in a matter of seconds upon illumination.

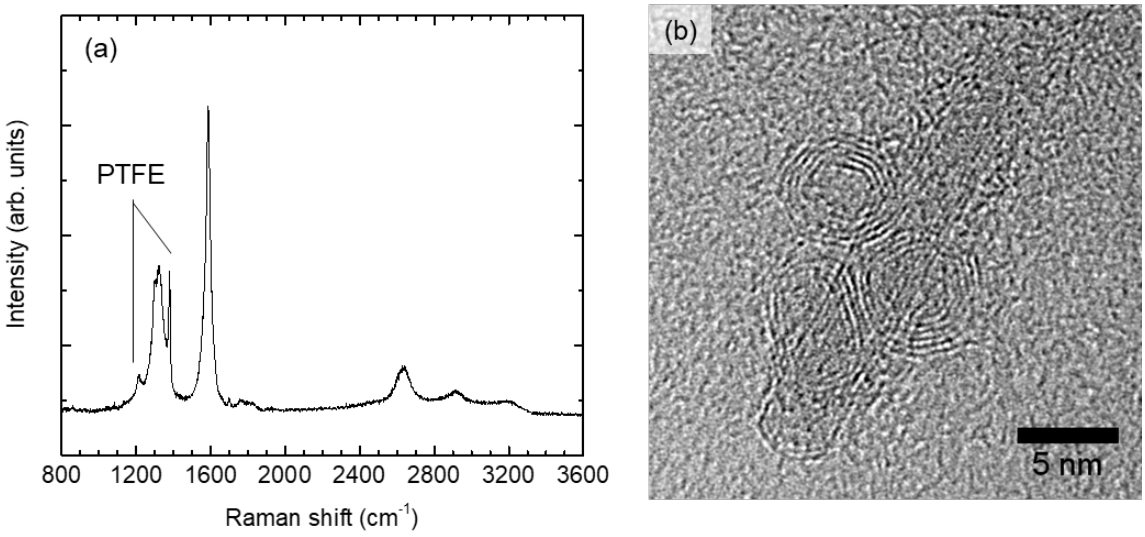

Figure 4-7. (a) Raman spectrum of collected OLC powder. Some interference from PTFE is present due to light loading of the filter. (b) TEM image of synthesized OLC particles along with a carbon nano-rod.

To investigate the origin of the OLC particles, a plasma was ignited with the filament in place but without injecting any MeOH. To prevent the plasma from expanding too much without MeOH, 0.09% H_2 was also added. In addition, power had to be kept at 70 W or below to stabilize the process. At these conditions, a bright orange incandescence at the plasma-filament interface was again observed, as was a stable PSD, shown in Figure 4-8(a), which was almost identical to the PSD generated with MeOH mixed into the plasma. Although this indicates that the observed particles originate from the filament in some way as opposed to gas phase nucleation, the Raman spectrum of the material produced from the filament without MeOH, shown in Figure 4-8(b), is significantly more disordered, i.e., has a much larger D band, more like the spectra in Figure 4-3. Therefore,

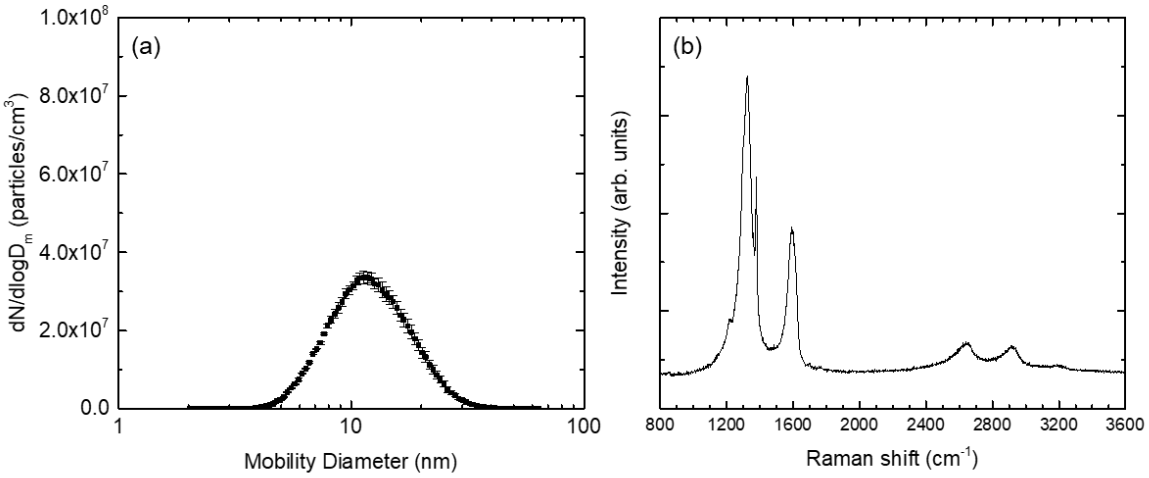

Figure 4-8. (a) SMPS scan and (b) Raman spectrum of particles produced from the filament using a gas mixture of 0.09% H_2 in Ar at 70 W.

while MeOH is not critical to the formation of particles in this operating mode, it does play a role in the quality of the synthesized material. With MeOH added to the feed, the filament continued to grow in length during operation, as shown in Figure 4-9(a). The filament itself was found to be composed of dendritic growths about 20 μm in diameter, shown in Figure 4-9(b), after viewing with an optical microscope. A sample Raman spectrum of the dendrites is shown in Figure 4-9(c), which exhibits fairly narrow D and G bands and, more noticeably, a very large 2D band. The intensity of the 2D band with respect to the G band suggests the dendrites are composed of turbostratic graphite,[15] which does not exhibit the same doublet structure in its 2D band as highly-oriented graphite and bears more of a similarity to single-layer graphene.[16]

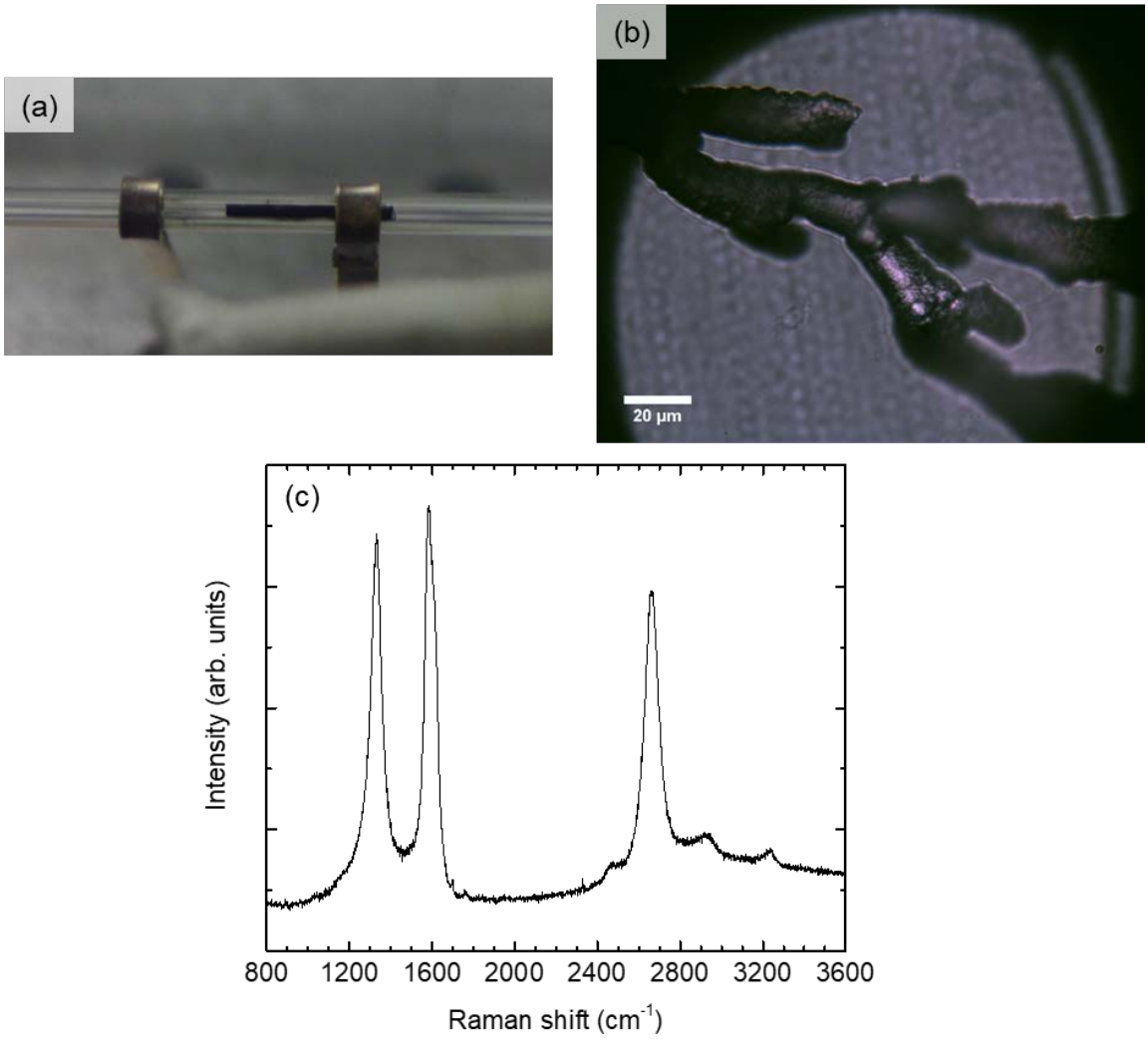

Figure 4-9. (a) Photo of the filamentary growth in the reactor after several hours of operation. (b) Optical microscope photo of the dendritic material composing the filament and (c) Raman spectrum of a carbon dendrite.

4.4 Conclusions and future work

Carbon nanoparticles were synthesized in an atmospheric pressure RF CCP reactor under two different operating modes. In the homogeneous growth mode, the resulting particle morphology was found to be very similar to the products of the low pressure version of the reactor in Chapter 3, as assessed by both Raman spectroscopy and TEM.

However, the morphology did not depend strongly on the amount of H_2 added, but did depend on choice of precursor and especially on applied power. H_2 did, nonetheless, have an inhibiting effect on particle nucleation and growth. As in Chapter 3, the particle structure in this study tended to evolve from highly sp^2-coordinated amorphous carbon in the direction of more ordered nanocrystalline graphite. However, while in Chapter 3 no apparent limit to this trend was reached, in this case increasing power input led to either rapid film growth on the reactor wall or to growth of a dendritic carbon filament down the center of the reactor, effectively limiting progression of homogeneous particle synthesis.

Growth of a dendritic carbon filament in the plasma at high power density was accompanied by generation of a stable PSD, which was determined to originate from the dendrites themselves. This enabled an alternative operating mode that was found to produce small, relatively crystalline OLC nanoparticles with good product homogeneity. In addition, the PSD in this mode could be tuned by adjusting the gas velocity. Although these particles originate from a solid-phase growth inside of the reactor, the growth also originates from the vapor precursor, in this case MeOH, thus opening the door to inclusion of dopants in the gas feed to tune particle properties. This operating mode is limited, however, by the continual lengthening of the carbon filament. Further exploration of the homogeneous synthesis route of carbon particles in this reactor will require some way of inhibiting film and dendrite growth. Finally, in either case, scale-up of the reactor volume to obtain higher throughputs should be considered. Given *pd* scaling of plasma breakdown voltage as described by Paschen's law, this is non-trivial for the chosen reactor geometry, outside of scaling by arrays. An alternative reactor geometry chosen for the purpose of

scaling plasma volume at atmospheric pressure while taking this limitation into account is detailed in the next chapter.

4.5 Acknowledgments

This work was supported by NSF Grant No. CBET-1335990 and Columbus Nanoworks, Inc. We are grateful to Dr. Hatsuo Ishida for access to Raman spectroscopy and to Dr. Danqi Wang for assistance with TEM. We would also like to thank Dr. Davide Mariotti for consultation with regard to reactor design and Adam Maraschky for assistance with photography.

4.6 References

1. Palmer, A. J. A physical model on the initiation of atmospheric-pressure glow discharges. *Appl. Phys. Lett.* **25,** 138–140 (1974).
2. Mariotti, D. & Sankaran, R. M. Perspectives on atmospheric-pressure plasmas for nanofabrication. *J. Phys. D. Appl. Phys.* **44,** 174023 (2011).
3. Kakiuchi, H., Ohmi, H. & Yasutake, K. Atmospheric-pressure low-temperature plasma processes for thin film deposition. *J. Vac. Sci. Technol. A Vacuum, Surfaces, Film.* **32,** 30801 (2014).
4. Nozaki, T. & Okazaki, K. Carbon nanotube synthesis in atmospheric pressure glow discharge: A review. *Plasma Process. Polym.* **5,** 300–321 (2008).
5. Nozaki, T. *et al.* Deposition of vertically oriented carbon nanofibers in atmospheric pressure radio frequency discharge. *J. Appl. Phys.* **99,** (2006).
6. Askari, S. *et al.* Silicon-based quantum dots: synthesis, surface and composition

tuning with atmospheric pressure plasmas. *J. Phys. D. Appl. Phys.* **48,** 314002 (2015).

7. Askari, S. *et al.* Ultra-small photoluminescent silicon-carbide nanocrystals by atmospheric-pressure plasmas. *Nanoscale* **8,** 17141–17149 (2016).
8. Ugarte, D. Curling and closure of graphitic networks under electron-beam irradiation. *Nature* **359,** 707–709 (1992).
9. Kozak, D., Shibata, E., Iizuka, A. & Nakamura, T. Growth of carbon dendrites on cathode above liquid ethanol using surface plasma. *Carbon N. Y.* **70,** 87–94 (2014).
10. Danilaev, M. P., Bogoslov, E. A., Pol, Y. E. & Nasybullin, A. R. Structure of Carbon Dendrites Obtained in an Atmospheric-Pressure Gas Discharge. **62,** 255–260 (2017).
11. Moreno-Couranjou, M., Monthioux, M., Gonzalez-Aguilar, J. & Fulcheri, L. A non-thermal plasma process for the gas phase synthesis of carbon nanoparticles. *Carbon N. Y.* **47,** 2310–2321 (2009).
12. Du, A. B., Liu, X. G., Fu, D. J., Han, P. D. & Xu, B. S. Onion-like fullerenes synthesis from coal. *Fuel* **86,** 294–298 (2007).
13. Kumar, A. *et al.* Formation of nanodiamonds at near-ambient conditions via microplasma dissociation of ethanol vapour. *Nat. Commun.* **4,** 2618 (2013).
14. Ferrari, A. C. & Robertson, J. Raman spectroscopy of amorphous, nanostructured, diamond-like carbon, and nanodiamond. *Philos. Trans. R. Soc. London A* **362,** 2477–2512 (2004).
15. Pimenta, M. A. *et al.* Studying disorder in graphite-based systems by Raman

spectroscopy. *Phys. Chem. Chem. Phys.* **9,** 1276–1291 (2007).

16. Ferrari, A. C. Raman spectroscopy of graphene and graphite: Disorder, electron-phonon coupling, doping and nonadiabatic effects. *Solid State Commun.* **143,** 47–57 (2007).

Chapter 5: Process scale-up considerations for non-thermal atmospheric-pressure plasma synthesis of nanoparticles by homogenous nucleation

5.1 Introduction

The dielectric barrier discharge (DBD) is an effective means for ionizing a large volume of gas at atmospheric pressure.[1] DBDs are industrially implemented for ozone generation,[2] wherein their success is due to both the large-scale production and low cost. In addition, DBDs have found success in UV and VUV light-emitting excimer lamps[3] and are currently being explored as tools for greenhouse gas (CO_2 and CH_4) conversion into value-added chemicals,[4,5] catalytic reduction of pollutants,[6] actuators for aerodynamic flow control,[7] and medical treatments.[8,9]

Typical DBD geometries include parallel plates, coaxial cylinders, and, such as in the case of aerodynamic actuators, coplanar electrodes.[10] In all cases, either one or both of the metal electrodes is covered by a dielectric material, and the plasma is operated by high voltage, alternating current (AC). For gas-phase plasma-chemical applications, such as the examples of ozone generation and plasma-catalytic conversion processes, cylindrical geometries are preferred. Nanoparticle production from vapors by DBD is less reported, but the cylindrical geometry has been employed there as well.[11] As will be shown, there are good engineering reasons for choosing a cylindrical geometry when designing a plasma reactor with scale-up in mind.

In contrast with chemical reactions that convert one molecule into another, nanoparticle production processes are significantly more complex.[12] The value of the

nanoparticle product itself is strongly dependent on the particles' surface and bulk material quality, the mean size and variance of the particle size distribution (PSD), and whether there is significant agglomeration. In the case of catalytic applications, for instance, the surface area to volume ratio of a nanoparticle powder is a strong determinant of its catalytic activity.[13,14] Therefore, scaling nanoparticle production to higher throughputs must preserve these properties. Because of the closely intertwined nature of particle nucleation, growth, and agglomeration kinetics,[15,16] enhancing throughput by simple steps such as increasing precursor concentration in the feed or increasing feed flow rate can increase the overall production rate, but also increase agglomeration.

In this chapter, scale up of nanoparticle production in a plasma reactor is studied by applying simplified scaling rules to a DBD reactor that attempt to preserve the particle properties, *i.e.*, size distribution. The first scaling rule is Paschen's law, which describes gas breakdown as a function of the gas pressure, *p*, and electrode gap, *d*, and which for *pd* on the order of 10 Torr*cm and greater is approximately linear and can be stated as

$$U_{\mathrm{b}} \propto pd \tag{5.1}$$

where U_{b} is the voltage at which breakdown of the gas into a plasma occurs. The implications of this relation when it comes to forming an atmospheric-pressure plasma are that to achieve breakdown, either a much higher voltage must be applied for a given electrode gap than would be needed at vacuum, or the gap must be reduced in size substantially. The second scaling rule applies to the characteristic parameters of the plasma after the discharge is formed, including its electron energy distribution function (EEDF), reduced electric field strength, and plasma density, all of which will determine

the reaction kinetics that ultimately lead to particle nucleation and growth. In general, similarity laws of high frequency discharges suggest that gas pressure, *p*, applied oscillation frequency, ω, applied voltage ΔU, and characteristic dimension, *d*, are the dominant operating variables that may be manipulated for a given gas such that the aforementioned parameters may be preserved in different reactor configurations.[17,18] Although these similarity laws typically apply better to RF and microwave (MW) plasmas, filamentary DBDs show a similar dependence.[19] For simplicity, a strategy would be to keep all of the aforementioned operating parameters constant. While atmospheric-pressure plasma reactors have been reported for nanoparticle synthesis with high throughput in mind,[20,21] no systematic comparison of the performance between differently-sized reactors has yet been reported that would enable further scale up, for example, to industrial production. The goal of this chapter is to develop an understanding of reactor design using a specific geometry that can be scaled indefinitely for nanoparticle production while maintaining the particle properties.

5.2 Approach to scale-up

Two reactor geometries and their suitability for scale-up were initially considered, either two parallel plates, *a la* Askari *et al.*,[21] or two coaxial cylinders (see Figures 5-1(a) and (b)). The volume, *V*, of a rectangular channel formed between two plate electrodes (with two additional walls of insulation to confine the gas stream) can be defined as

$$V = LWd \tag{5.2}$$

where *L* is the channel length in the direction of flow, *W* the width between insulation, and *d* the electrode gap distance (‘electrode’ here will refer to both bare electrode and

dielectric barrier surfaces). In comparison, the volume of a cylindrical annulus can be defined as

$$V = \pi L d^2 \left(\frac{D_o}{d} - 1\right) \tag{5.3}$$

where D_o is the outer diameter of the annulus and d is the width of the annulus gap. Along with keeping d constant, extents of chemical reactions and PSD evolution must be preserved by also retaining residence time in the plasma, τ, defined as

$$\tau = \frac{V}{Q} \tag{5.4}$$

where Q is the volumetric flow rate of the gas stream. Thus, for constant τ, throughput Q scales at the same rate as reactor volume V.

Knowing this, one potential scale-up scenario that can be envisioned is simply increasing L in either reactor. This scenario is quickly rejected for a few reasons. One, in both geometries, V would scale at the same rate as L, which is inefficient. Two, the Reynolds number, Re, which is defined as

$$Re = \frac{Q D_H}{\nu A_c} \tag{5.5}$$

where D_H is the hydraulic diameter, ν is the kinematic viscosity of the gas, and A_c is the cross-sectional area of the channel, increases continuously with Q if no compensation is made to D_H and A_c, thus driving a transition of flow regime from laminar to turbulent if Q increases by orders of magnitude. This leaves W and D_o, in the rectangular and annular cases, respectively, as the controlling parameters that may be scaled to increase V.

Keeping in mind that the desire now is to scale the reactor geometry in a way that is uncoupled from not only d but also τ and Re, the effectiveness of scaling W and D_o in the rectangular and annular channels, respectively, can be evaluated. Starting with the

rectangular channel, a scale parameter, λ, is introduced such that $\lambda = 1$ corresponds to $W = d$. Then,

$$W = \lambda d \tag{5.6}$$

$$V = \lambda L d^2 \tag{5.7}$$

$$A_c = \lambda d^2 \tag{5.8}$$

$$D_H = \frac{2Wd}{W + d} = \frac{2\lambda d}{\lambda + 1} \tag{5.9}$$

$$Re = \frac{2Q}{(\lambda + 1)\nu d} = \frac{2\lambda L d}{(\lambda + 1)\nu\tau} \tag{5.10}$$

As may have already been apparent, V in this case also only scales at an equivalent rate to W, just like in the case of increasing L. In addition, Re is coupled to λ, though asymptotically. Should this be problematic, it could be compensated for by additionally scaling L by $(\lambda+1)/\lambda$, though this would then limit growth of V to $(\lambda+1)/2$, and the same for Q if τ is also to remain uncoupled.

Alternatively, scaling D_o of an annular channel by λ, assigned arbitrarily such that $\lambda = 1$ corresponds to $D_o = 2d$ (i.e., an annulus with an infinitesimally small core cylinder), results in the following:

$$D_o = \lambda 2d \tag{5.11}$$

$$V = \pi L d^2 (2\lambda - 1) \tag{5.12}$$

$$A_c = \pi d^2 (2\lambda - 1) \tag{5.13}$$

$$D_H = 2d \tag{5.14}$$

$$Re = \frac{2Q}{\pi\nu d(2\lambda - 1)} = \frac{2Ld}{\nu\tau} \tag{5.15}$$

In this scenario, scaling D_o by λ scales V by $(2\lambda-1)$, an improvement over the parallel plate case (see Figure 5-1(b)). In addition, Re is completely uncoupled from λ, which simplifies the scale-up process. Because of these advantages, this study focuses on the coaxial geometry.

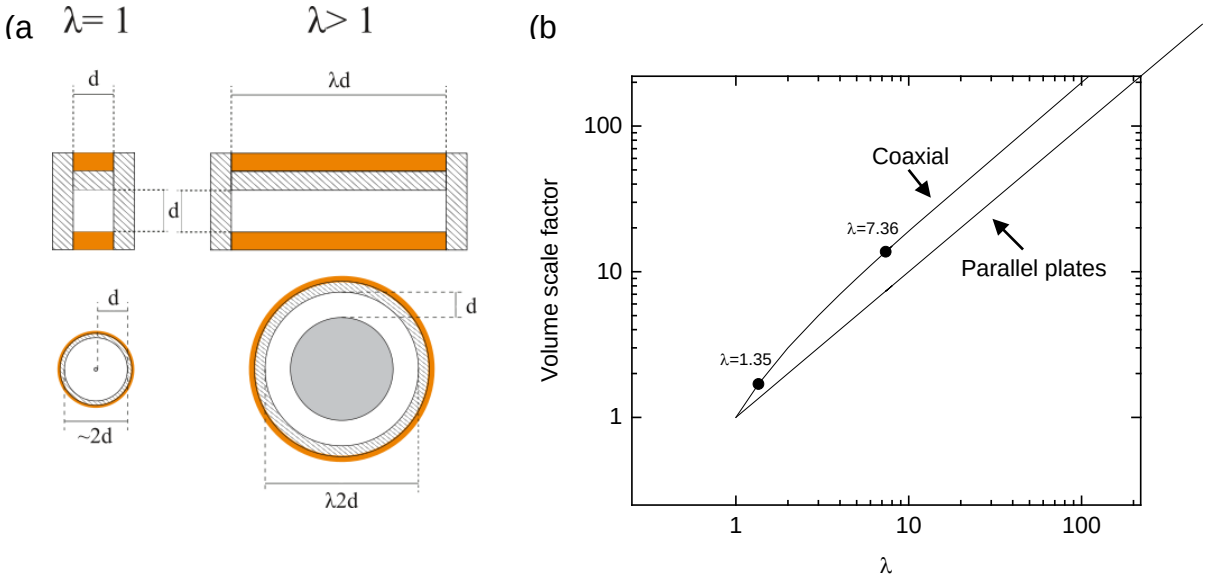

Figure 5-1. (a) Schematic diagram of scale-up procedure for parallel plate and coaxial cylinder geometries and (b) corresponding plot showing how reactor volume scales with λ. Data points refer to approximate λ values for the two pilot reactors studied in this work, with d = 1.5 mm.

In addition to d, Re, and τ, there are other factors to consider during scale-up. Because surface interactions may play a strong role in both the discharge physics and reaction kinetics, the ratio of electrode surface area to volume should also be maintained. It can be easily shown that this is the case for both parallel plates and coaxial electrodes. Moreover, in the case of kHz-driven DBDs, it's previously been found that charge transferred per microdischarge scales with the dielectric layer thickness as well as the

dielectric barrier capacitance and total reactor capacitance, C_{cell}.[19] For the pilot reactors tested in the following sections, these parameters were not initially considered, but may have played a role in the results (see Section 5.4.6). Finally, one might also consider the conductance of the reactor, which may induce a pressure gradient that varies with λ. This dependence is complex and not expected to decouple from λ in either of the geometries discussed, so it is not considered here. The conductance of rectangular and annular channels over all pressures is described elsewhere.[22]

As was previously indicated, this scale-up strategy could potentially apply to any DBD-like atmospheric pressure plasma regime, whether kHz-driven filamentary, glow, or RF-α. A kHz-driven filamentary regime was chosen here because it operates at orders of magnitude lower current[23] and therefore lower temperature than the RF-α regime and does not require an additional dielectric layer on the inner electrode to protect it from sputtering.[19] Also, synthesis of nickel (Ni) nanoparticles from bis(cyclopentadienyl)nickel(II) ('nickelocene') molecules, which has been previously reported,[24–26] was chosen for study to focus on the evaluation of the reactors.

5.3 Experimental design

Two reactors with a gas gap of $d \sim 1.5$ mm and corresponding outer and inner diameters that produce a nine-fold change in volume were fabricated, with scale factors λ for what will be referred to as the small (S) and large (L) reactors being 1.35 and 7.36, respectively. A summary of the component dimensions and materials is given in Table 5-1. Although the intention was to keep both the electrode gaps and dielectric thicknesses

in the two reactors identical, there were small differences because of the standard sizes of materials available.

Component	Material	Size (small)	Size (large)
Inner electrode diameter (mm)	316 Stainless steel	1.59	19.0
Dielectric inner diameter (mm)	Clear-fused quartz	4.04	22.1
Dielectric outer diameter (mm)		5.94	24.9
Outer electrode width (mm)	Copper tape	3.18	3.18
Gap distance (mm)		1.23	1.51
Annulus volume (mm^3)		34.4	310

Table 5-1. Summary of component materials and dimensions of the two test DBD reactors.

The discharges in both reactors were initiated and sustained at atmospheric pressure using a high voltage AC power supply (Information Unlimited, Model PVM500) typically operated at 23.5 kHz. Breakdown of the plasma typically occurred around 3 kV peak-to-peak (p-p). High voltage was applied to the outer electrode for simplicity, while the inner electrode was grounded, though the opposite configuration was briefly tested and found to work equally well. One particular design consideration that was found to have a significant impact on results was electrode centering. While an off-center electrode has been shown in an inductively-coupled RF system to aid in plasma expansion at atmospheric pressure,[20] care has been taken here to keep the inner electrode centered in both reactors for the purpose of providing a more systematic performance comparison. The orientation of the inner electrodes with respect to the quartz outer tubes was not perfectly rigid due to bending of the stainless steel rods used and to flexibility from the polymer ring-sealed gas fittings used to connect the quartz tubes to the rest of

the gas plumbing in the experimental setup. In order to make fine adjustments to the inner electrode orientation, two adjustable platforms were used to support each end of the reactor. Sufficient centering was judged by eye according to how uniformly the plasma filled the annular channel. Inner electrode surfaces were kept smooth, though some surface roughness was not found to have a significant impact on results.

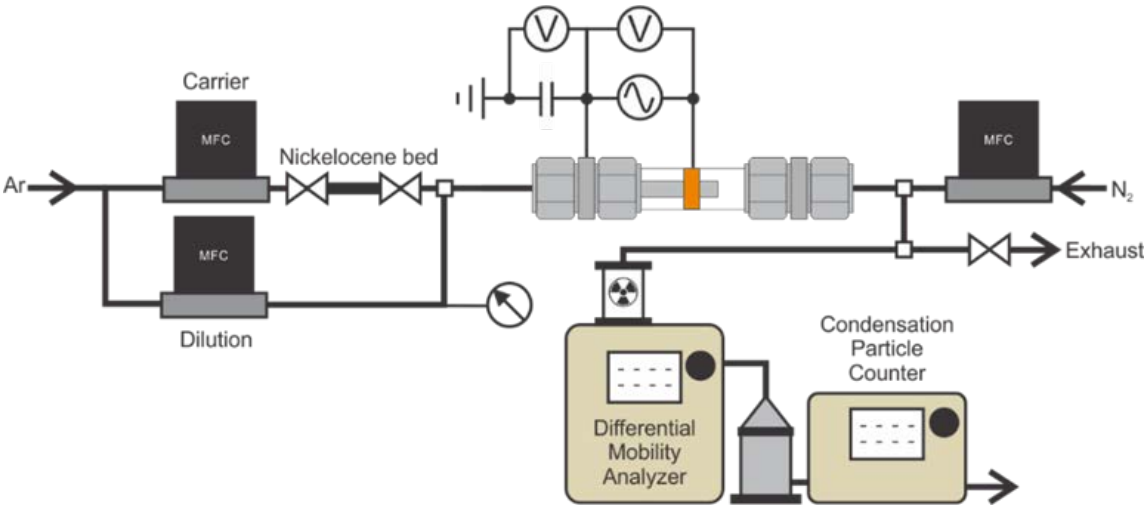

Figure 5-2. Schematic of experimental setup for nanoparticle synthesis and online aerosol ion mobility measurements using coaxial DBD reactor.

A schematic of the experimental setup, including electrical circuitry, is shown in Figure 5-2. Electrical characterization of the process was carried out following the standard method described by Brandenburg *et al.*[10,27,28] The applied voltage waveform, *U(t)*, was measured using a 1000:1 turndown high voltage, high frequency probe (Pintek HVP-15HF) and read from an oscilloscope (Agilent 54616B). Despite the high turndown ratio, the probe nevertheless draws a significant current, altering the plasma; for this reason, all experiments were conducted with the probe attached throughout their entirety. To measure the induced charge waveform *q(t)* of the reactor, a 46 nF ceramic disk

capacitor was placed in between the inner electrode and ground, and the voltage drop across the capacitor was directly read with the oscilloscope. In the absence of plasma, i.e., at sub-breakdown voltages, the capacitance of each reactor itself, C_{cell}, can be estimated from the charge and voltage waveforms using the equation

$$q_{\text{dis}}(t) = C_{\text{cell}} U(t) \tag{5.16}$$

which allows extrapolation of the displacement charge, q_{dis}, at any voltage after the initiation of a plasma. Subtracting q_{dis} from the total q waveform yields q_{plasma}, the charge transferred through the plasma, which is useful for determining the power transferred through the discharge, P_{plasma}. To do so, a Lissajous plot, $q_{\text{plasma}}(t)$ versus $U(t)$, was constructed, and the area contained within one cycle was calculated and then multiplied by the oscillation frequency, ω:

$$P_{\text{plasma}} = \omega \int_{U(t_0)}^{U\left(t_0+\frac{1}{\omega}\right)} q_{\text{plasma}}(t) dU(t) \tag{5.17}$$

It should be noted that this analysis relies on the validity of an equivalent circuit as an approximation for the behavior of the DBD reactor[27,28]. Digital acquisition of waveforms and calculation of P_{plasma} were performed *in situ* using a customized LabView Virtual Instrument (VI). Finally, optical emission spectra (OES) were also collected from each reactor under standard operating conditions using an OceanOptics HR4000 spectrometer (detection range 373.4 to 822.8 nm and NA of 0.22) to provide supplemental information on plasma conditions. Plasma emission was collected using a 600 μm fiber optic cable, external to the reactor, oriented at a slight angle to the inner electrode axis.

The vapor precursor, nickelocene, was introduced by sublimation of a powder with a flow of Ar gas. Because the vapor pressure of nickelocene, taken from Torres-

Gómez *et al.*,[29] is low, only one dilution line was needed to achieve the desired precursor concentration range, in this case 0.1 to 10 ppm. The nickelocene powder (obtained from Sigma-Aldrich) was loaded into a ¼" OD stainless steel tube plugged on either end with glass fiber to prevent displacement. To prevent oxidation of the nickelocene, which was found to have a significant influence on results, care was taken to always load fresh powder into the tube from inside a nitrogen-filled glove box. The tube could then be capped on either end with plug valves for transportation and installment into the experimental setup. To further prevent oxidation from residual air in the Ar service lines and in the event of swapping MFCs, a purge valve was also installed upstream of the nickelocene bed to turn over any contaminated Ar before each experiment. Because the flow rate of nickelocene itself is small and can be neglected, its concentration, y_{nick}, was estimated from the equation

$$y_{\mathrm{nick}} = \frac{Q_c p^*_{\mathrm{nick}}(T)}{(Q_{\mathrm{c}} + Q_{\mathrm{dil}})p} \tag{5.18}$$

where Q_{c} is the carrier gas flow rate, Q_{dil} is the dilution flow rate, $p^*_{\mathrm{nick}}(T)$ is the equilibrium vapor pressure of nickelocene as a function of temperature, and p is the total gas pressure. Carrier and dilution flow rates were controlled by thermal MFCs. A Bourdon pressure gauge was installed upstream of the reactor to detect any pressurization; at the highest reactor flow rate tested, 10 slm, a rotary-vane pump (Edwards RV3) with a throttle valve at the inlet was installed in parallel with the exhaust line labeled in Figure 5-2 in order to compensate for pressurization inside the reactor. All other experiments did not require this measure. Finally, the nickelocene bed was wrapped with heating tape in order to reach the higher end of the concentration range examined. In order to prevent re-condensation on the walls of the service lines, the heating tape

extended somewhat past the point at which the carrier gas stream joined with the dilution stream. To reduce experimental error, the same temperature was used for each concentration regardless of the total flow rate being examined. In addition, the flow rate of carrier gas through the nickelocene bed was kept below 200 sccm in order to increase the likelihood of reaching equilibrium saturation.

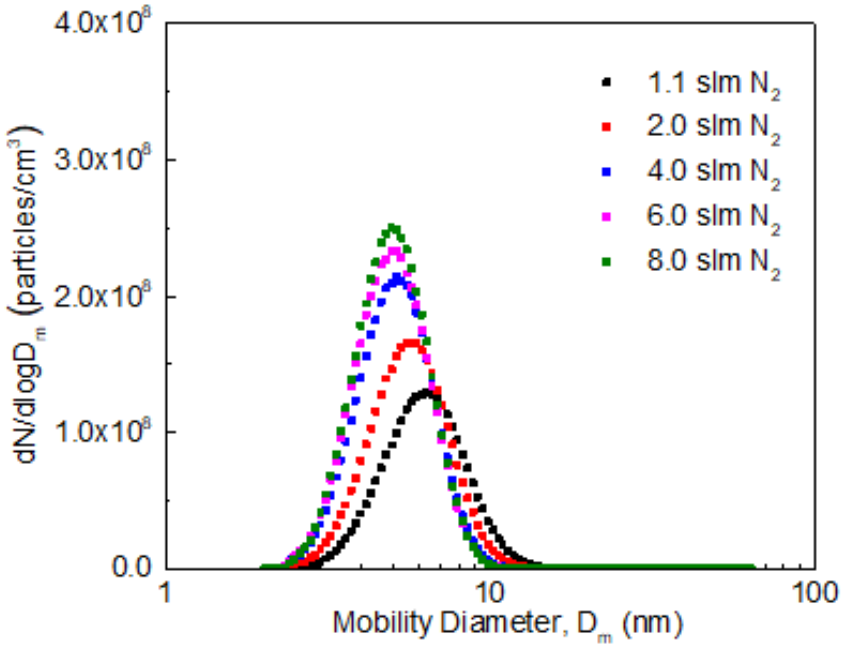

Figure 5-3. PSDs showing the influence of N_2 flow rate on distribution parameters of particles generated in the small reactor.

PSDs synthesized in the reactor were measured online by the same SMPS system described in Section 2.2. Before entering the SMPS, the reactor effluent was diluted with a stream of N_2, also controlled by a thermal MFC. This was especially necessary if the reactor effluent flow rate was less than the required inlet flow rate at the CPC of 1.5 slm. If the reactor effluent flow rate was greater than 1.5 slm, the excess was split into an

exhaust (see Figure 5-2). Adding a N_2 dilution also minimized the residence time available for the particles to agglomerate. An example PSD measured using different N_2 dilution flow rates is shown in Figure 5-3. The N_2 dilution also prevented gas breakdown in the DMA, which is easier in Ar. An Ar concentration of 15% or less in the DMA was sufficient to prevent breakdown.

The SMPS measures PSDs as $dN/d\log D_m$ versus D_m, where N is particle number per unit volume and D_m is the so-called mobility diameter, i.e., the diameter of a sphere that would have the same mobility (in $m^2\ V^{-1}\ s^{-1}$) as the objects actually being filtered through the DMA at a particular voltage. For particles that closely approximate spheres, this is the same as particle diameter; for other shapes or for fractal-like chains, this value corresponds with the object's mobility but only roughly with a characteristic dimension. Because of the N_2 dilution, the measured PSDs were modified to reflect particle concentrations at the reactor outlet by the following relation:

$$\frac{Q_R + Q_{N2}}{Q_R}\left(\frac{dN}{d\log D_m}\right)_{measured} = \left(\frac{dN}{d\log D_m}\right)_{reactor} \tag{5.19}$$

where Q_R is the total flow rate through the reactor and Q_{N2} is the flow rate of N_2. Each PSD could also be converted to a rate distribution by multiplying by Q_R:

$$Q_R\left(\frac{dN}{d\log D_m}\right)_{reactor} = \left(\frac{d(Q_R N)}{d\log D_m}\right)_{reactor} \tag{5.20}$$

This rate distribution reflects the particle throughput of the reactor, as opposed to particle concentration. In order to systematically compare the shapes of the PSDs collected, each was fit with a log-normal curve. To do so, each PSD was converted to dN/dD_m by the following transformation:

$$\frac{1}{\ln(10)D_{\mathrm{m}}}\frac{\mathrm{d}N}{\mathrm{dlog}D_{\mathrm{m}}}=\frac{\mathrm{d}N}{\mathrm{d}D_{\mathrm{m}}} \tag{5.21}$$

Without this transformation, the integral under each measured curve, $\int \frac{\mathrm{d}N}{\mathrm{dlog}D_{\mathrm{m}}}\mathrm{d}D_{\mathrm{m}}$, would be non-physical. Then, from the definition of the log-normal distribution,

$$\frac{\mathrm{d}N}{\mathrm{d}D_{\mathrm{m}}}=\frac{N_{\mathrm{total}}}{D_{\mathrm{m}}\sigma\sqrt{2\pi}}\exp\left(\frac{-(\ln D_{\mathrm{m}}-\mu)^2}{2\sigma^2}\right) \tag{5.22}$$

where N_{total} is the integral under $\mathrm{d}N/\mathrm{d}D_{\mathrm{m}}$, i.e., the total number concentration of particles of all sizes, and μ and σ are the so-called location and scale parameters, respectively. These are related to the geometric mean, GM[D_{m}], and geometric standard deviation, GSD[D_{m}], of the PSDs by the following definitions:

$$\mathrm{GM}[D_{\mathrm{m}}]=\mathrm{e}^{\mu} \tag{5.23}$$

$$\mathrm{GSD}[D_{\mathrm{m}}]=\mathrm{e}^{\sigma} \tag{5.24}$$

The total volume of particles in the aerosol per volume of gas, which is related by material density to the total mass of particles per volume of gas, can also be computed by the following relation, assuming the particles are approximately spherical:

$$V_{\mathrm{total}}=\frac{\pi}{6}N_{\mathrm{total}}\mathrm{e}^{3\mu+\frac{9}{2}\sigma^2} \tag{5.25}$$

Although this equation is useful in the ideal case of spherical particles, it is unfortunately of limited utility when the objects in the aerosol are irregularly shaped, as is the case in many of the experimental conditions that follow.

Before each experiment, a plasma was initiated in pure Ar gas and monitored with the SMPS to ensure no residual nickelocene or other contaminants were present in the reactor that could nucleate particles. At each set of operating conditions with nickelocene added, the PSD produced by the reactor was typically found to converge to a particular

final shape within the time span of one SMPS scan, about two minutes. The first scan after initiating the plasma was thus typically not used in data analysis. At least five scans of steady-state operation were collected and averaged to produce the PSDs shown, with error bars representing the standard error of the mean (SE) in each measurement bin.

To measure the mass production rate of particles, the aerosol product was collected using the same filtration setup described in Section 2.2. Material collection was limited to when a significant pressurization was incurred. For HRTEM studies, particles were deposited directly from the reactor exit onto a TEM grid with a 2-3 nm amorphous carbon film (Ted Pella, Inc. 01824) taped to a small disk electrode in an electrostatic precipitation device (TSI, Inc. Model 3089). HRTEM and energy-dispersive X-ray spectroscopy (EDS) were performed with an FEI Tecnai F30 at 300 kV accelerating voltage.

5.4 Results and discussion

5.4.1 *PSD measurements by SMPS at varying precursor concentration*

Photos of the small and large reactors with a plasma initiated at 6 kV p-p are shown in Figure 5-4. Figure 5-5(a) shows the PSDs measured from the two reactors at the same voltage and at y_{nick} of 0.1, 1, and 10 ppm. Flow rates of 0.39 and 3.51 slm were used in the small and large reactors, respectively, in order to control for τ, equal to 5.2 ms in this case, at the different reactor volumes. Increasing the precursor concentration is found to shift GM[D_m] to larger sizes while N_{total} increases with y_{nick} from 0.1 to 1 ppm but then decreases when y_{nick} is increased to 10 ppm. These trends are consistent with previously reported results[26] and are understood in terms of simultaneous nucleation,

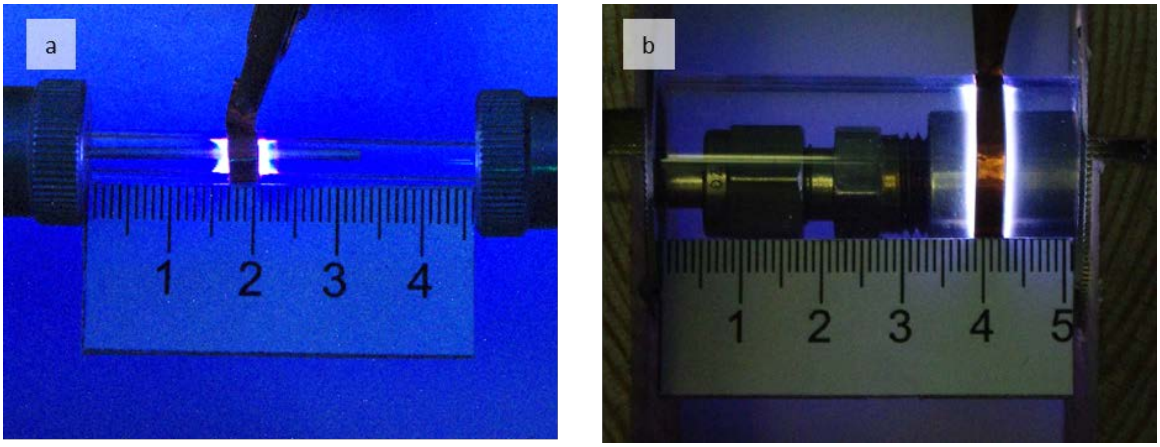

Figure 5-4. Photographs of (a) small reactor and (b) large reactors operating at an applied voltage of 6 kV p-p. Scale shown is in cm.

growth, and agglomeration of particles. As the concentration of nickelocene is increased, the concentration of nucleation precursors, i.e. supersaturated Ni atoms, is expected to increase as well, leading to faster nucleation and growth rates and hence larger N_{total} and GM[D_{m}]. However, as the concentration of particles themselves increases, increase of GM[D_{m}] may occur predominantly from a high agglomeration rate, which consumes particles; a net decrease in N_{total} may then be explained by an agglomeration rate outpacing nucleation. Importantly, as was the goal of this study, the PSDs from the two reactors at each y_{nick} are remarkably similar. Furthermore, because the flow rate is increased nine-fold in the large reactor, the throughput of particles, $\frac{\text{d}(Q_{\text{R}}N)}{\text{dlog}D_{\text{m}}}$, is also nine times greater, as shown in Figure 5-5(b). A summary of parameters obtained from log-normal fits to the PSDs in Figure 5-5 is shown in Table 5-2 for direct comparison.

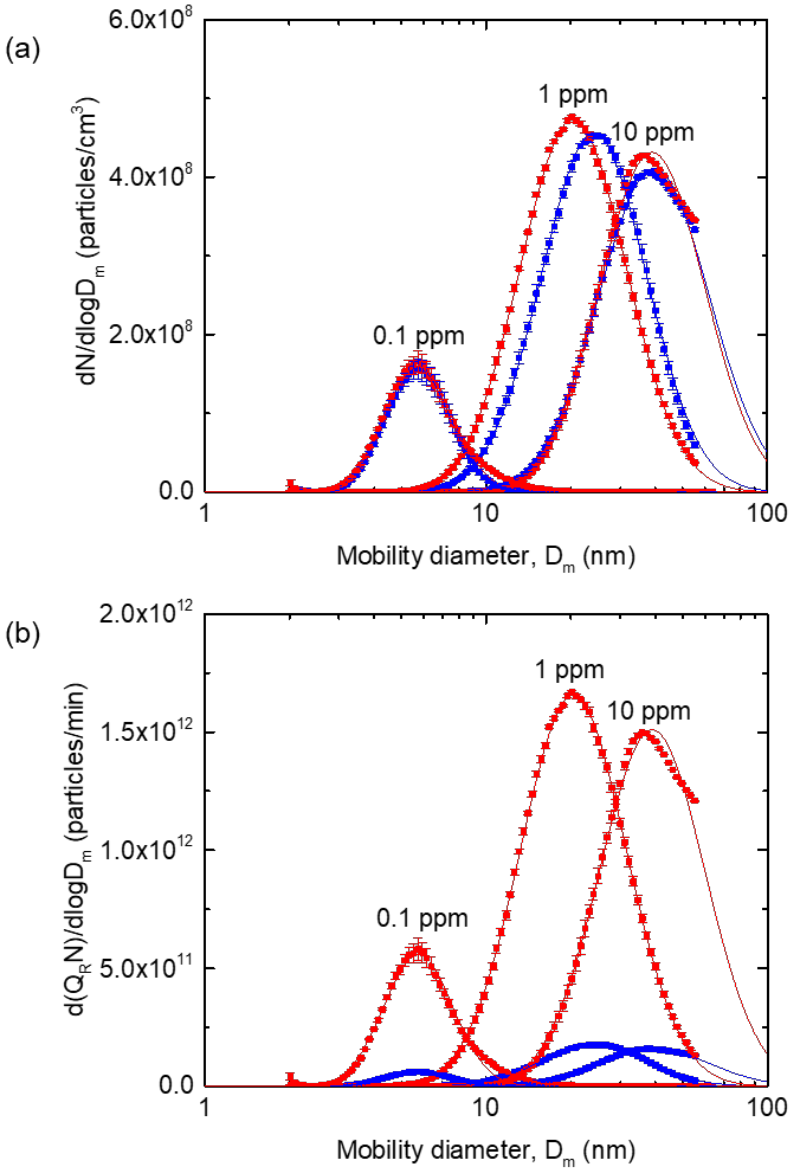

Figure 5-5. PSDs obtained by SMPS as a function of indicated y_{nick} in small (blue) and large (red) reactors in terms of (a) particle number concentration, dN/d(logD_m), and (b) particle number production rate, d($Q_R N$)/d(logD_m). Solid lines represent log-normal fits to the data. Flow rate was 0.39 slm in the small reactor and 3.51 slm in the large reactor, and applied voltage was 6 kV p-p in both reactors

y_{nick} (ppm)	Reactor	Q_R (slm)	GM[D_m] (nm)	GSD[D_m]	N_{total} (particles/cm^3 x 10^{-7})
0.1 ppm	S	0.39	5.7	1.30	4.4
	L	3.51	5.7	1.33	4.9
1 ppm	S	0.39	24.2	1.54	21.0
	L	3.51	20.4	1.54	22.5
10 ppm	S	0.39	39.5	1.57	20.3
	L	3.51	38.9	1.54	20.1

Table 5-2. A summary of distribution parameters estimated by log-normal fits corresponding to the data presented in Figure 5-5 for the purpose of quantitatively comparing the aerosol product from each reactor.

5.4.2 *Reactor throughput and efficiency*

In addition to measuring PSDs, a secondary assessment of the nanoparticle production rate in the reactors was obtained by filtration and weight measurements. There are a few caveats regarding the interpretation of this measurement. One, non-nickel, organic components originating from the cyclopentadienyl rings, could incorporate in the collected solid material. Two, pure Ni nanoparticles are expected to also be sensitive to oxygen in air. Therefore, the measured weight should not be assumed to reflect only the metal content of the nanoparticle product. However, assuming a similar degree of contribution from contaminant sources in all of the collected samples, comparison of the relative differences in production rate is nonetheless informative. Figure 5-6(a) shows the measured mass production rate of nanoparticles, calculated from the weight of filtered material and the collection time, as a function of y_{nick} for both the small and large reactors. In agreement with SMPS measurements, increasing y_{nick} is found to increase the mass

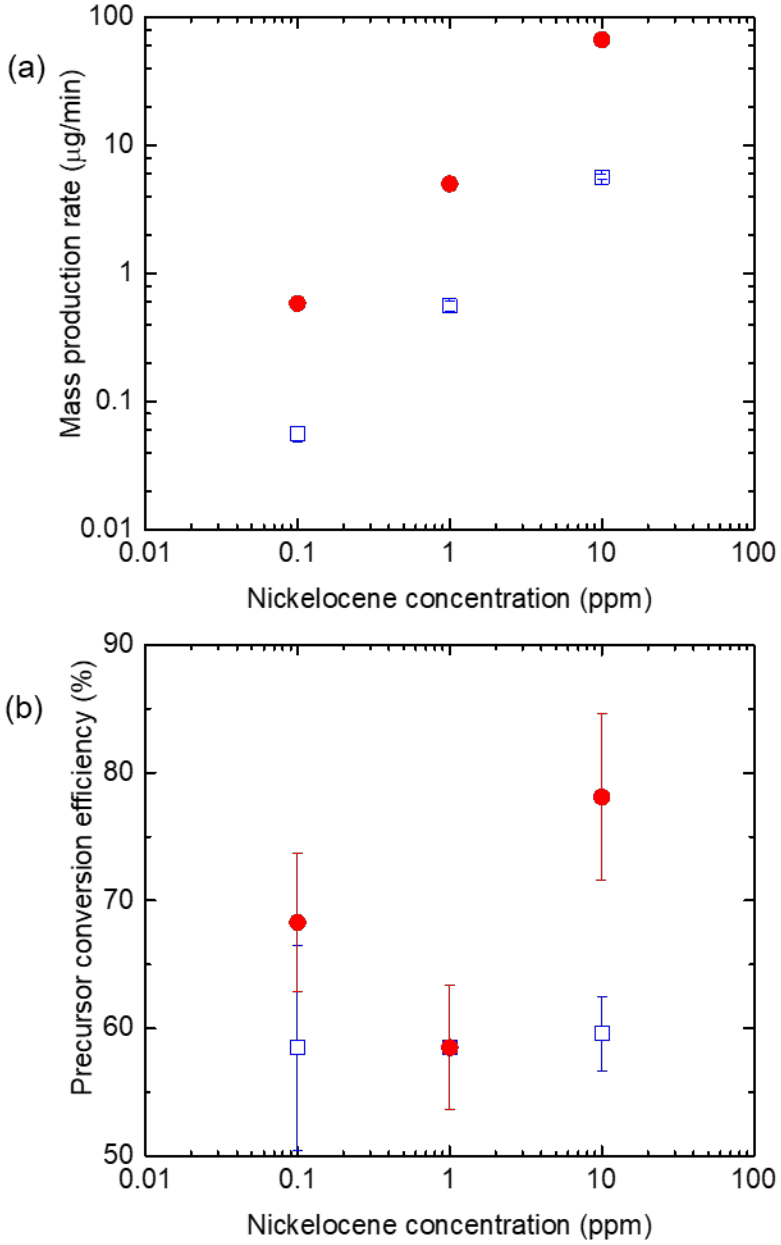

Figure 5-6. (a) Mass production rate and (b) precursor conversion efficiency for Ni nanoparticle synthesis in the small (open blue squares) and large (solid red circles) reactors as a function of y_{nick}. Total gas flow rates were 0.39 slm for the small reactor and 3.51 slm for the large reactor.

production rate in both reactors, and nearly an order of magnitude increase in throughput from the small to the large reactor is evident. Photographs of the filtered material, Figure 5-7, also visibly show these relative changes in mass. It should be emphasized that the measured production rate does not correlate with $Q_R N_{total}$ since GM[D_m] is different at each y_{nick}. Instead, it should in theory correlate with $Q_R V_{total}$, though, as noted in Section 5.3, this would only be valid for spherical particles.

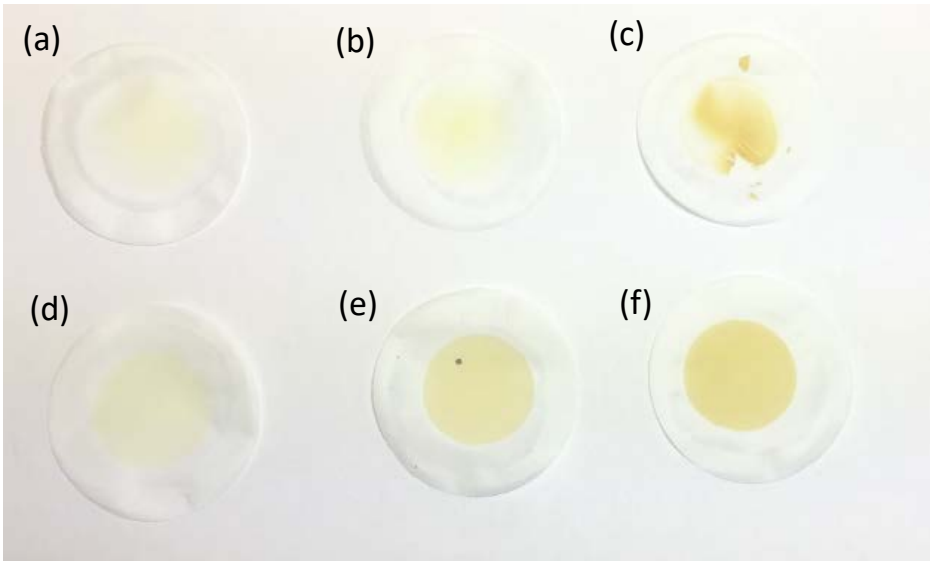

Figure 5-7. Photographs of material collected on PTFE fiber filters from (a) small reactor at y_{nick} = 0.1 ppm after 36 h, (b) small reactor at y_{nick} = 1.0 ppm after 6 h; (c) small reactor at y_{nick} = 10 ppm after 1 h, (d) large reactor at y_{nick} = 0.1 ppm after 6 h, (e) large reactor at y_{nick} = 1.0 ppm after 40 min, and (f) large reactor at y_{nick} = 10 ppm after 3 min.

From the collected material, a precursor conversion efficiency was calculated, defined as

$$Conversion\ efficiency = \frac{Mass\ production\ rate}{Elemental\ precursor\ mass\ input\ rate} \tag{5.26}$$

where the denominator refers to the mass input rate of the element of interest, in this case Ni, contained in the precursor molecule. The conversion efficiency for both reactors is given in Figure 5-6(b) and found to be relatively constant for the small reactor at ~60%, but less constant and generally higher for the large reactor, fluctuating between ~60 and 80%. In addition to the precursor conversion efficiency, as defined above, the specific energy cost can be defined as

$$Specific\ energy\ cost = \frac{Total\ power\ input}{Mass\ production\ rate} \tag{5.27}$$

These calculations are compared in Table 5-3 with literature values, along with corresponding process details, for nanoparticle synthesis in non-thermal plasma systems by homogeneous nucleation, both at low pressure and atmospheric pressure. For this comparison, only the primary particle size is used, i.e., agglomeration of particles is not taken into account. Table 5-3 shows that low pressure systems tend to produce higher production rates than atmospheric pressure systems. They also tend to result in better utilization of precursor, though the present work is possibly an exception. It's also noteworthy that the system examined in the present work, a kHz-driven DBD, consumes much less power than RF-ignited systems but nonetheless has a similar specific energy cost. Reference [21], which is ignited by RF in a parallel plate geometry, but operates at atmospheric pressure, is an exception and suffers from both a low nanoparticle production rate and specific energy cost, thus highlighting the challenges of designing an atmospheric pressure reactor capable of high throughput.

Besides the metrics tabulated in Table 5-3, another consideration that is common to all non-thermal plasma methods of nanoparticle synthesis is the cost of the precursor molecule itself, which may be expensive to produce in large quantities. This contrasts

somewhat with thermal plasma,[30] metal evaporation, and spark or laser ablation methods,[31] where a base material in the solid phase may be used as precursor feed (though $TiCl_4$ is one exception since it is itself an intermediate used to produce base Ti). In addition, as highlighted in the Introduction, the value of the particles themselves depends strongly on their material quality. It has already been noted earlier that the presence of byproducts can influence the way in which process efficiency is evaluated; beyond that, there is also crystalline fraction and surface character[32,33] and, of course, the PSD shape and degree of agglomeration. While emphasis in the literature has adequately been given to the feasibility of a reactor type in terms of total nanoparticle production

Reference	Nanoparticle material	Power source	Precursor	Operating pressure	Total Power input	Primary particle diameter	Mass production rate	Precursor conversion efficiency	Specific energy cost
Present work	Ni	20-30 kHz	$Ni(Cp)_2$	1 atm	1 W	7 nm	66.7 µg/min	60-80%	1 J/µg
[21]	Si	13.56 MHz	SiH_4	1 atm	100 W	6 nm	16.7 µg/min	3-9%	3,600 J/µg
[20]	ZnO	13.56 MHz	$Zn(C_2H_5)_2/O_2$	1 atm	25-45 W	20 nm	400 µg/min	~7-70%*	6.8 J/µg
[34]	TiN	13.56 MHz	$TiCl_4/NH_3$	3 Torr	180 W	4-8 nm	833 µg/min	40%	13 J/µg
[33]	Si	13.56 MHz	$SiCl_4$	3.5 Torr	175 W	5-10 nm	2,330 µg/min	50%	4.5 J/µg

Table 5-3. A comparison of production rates of nanoparticles synthesized in non-thermal plasma systems by homogeneous nucleation. For this work, results are shown for nanoparticles synthesized from 10 ppm nickelocene in the large reactor at a total gas flow rate of 3.51 slm. *Information in Reference [20] insufficient to accurately estimate precursor conversion efficiency.

rate and other metrics highlighted in Table 5-3, this work takes a step further by evaluating how a particular reactor type performs in preserving PSD and material quality as throughput is scaled.

5.4.3 *HRTEM analysis*

To evaluate the nanoparticle structure, composition, and other properties not given by SMPS measurements, analysis by TEM was carried out. Figures 5-8(a) and (b) show HRTEM micrographs of particles synthesized from 0.1 ppm nickelocene in the small and large reactors, respectively, and directly deposited onto TEM substrates. The images reveal well-dispersed particles less than 5 nm in diameter in both cases, slightly smaller than those measured by SMPS (see Table 5-2). A possible reason for this discrepancy is the presence of an organic coating on the particles originating from cyclopentadienyl rings. In support, the lattice spacings are visible, an example of which is shown in Figure 5-8(c), even though one would expect spontaneous oxidation of pure Ni nanoparticles. A hydrocarbon coating could thus explain how the crystalline core was protected from oxidation during transfer of the deposited particles in room air. The measured lattice spacings match well with hexagonally close-packed (hcp) Ni, although identification of hcp Ni based on diffraction alone has been argued to be ambiguous with Ni_3C.[35] This is somewhat surprising given that the thermodynamically stable form of Ni is face-centered cubic (fcc). EDS does nonetheless further confirm that the samples consist primarily of Ni, as shown in Figure 5-8(d), but because of the presence of C in the background film, Ni_3C cannot necessarily be confirmed.

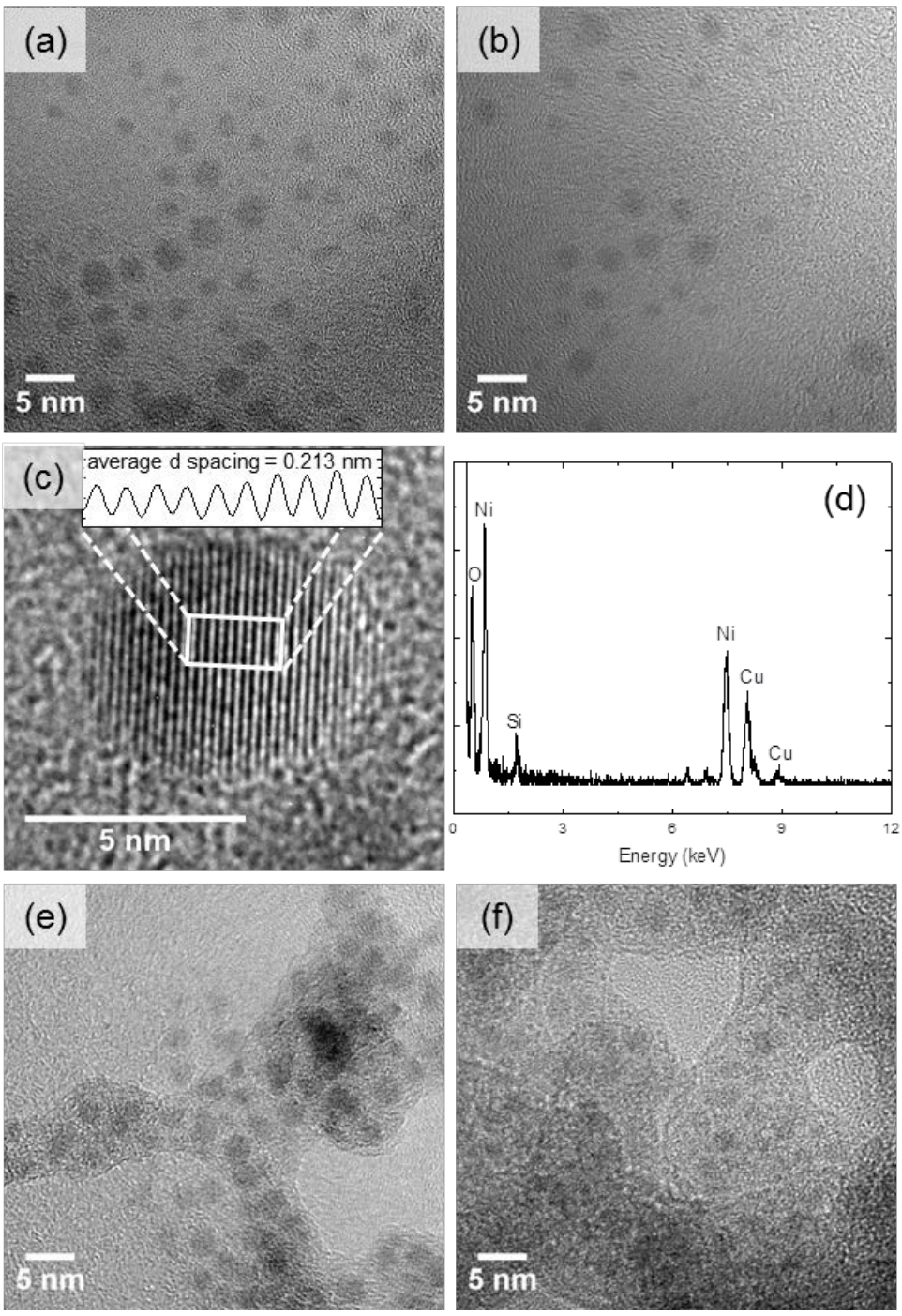

Figure 5-8. TEM images of Ni nanoparticles synthesized from 0.1 ppm nickelocene in (a) small and (b) large reactors. (c) High-resolution TEM image of a representative Ni nanoparticle exhibiting lattice spacings with an average distance of 0.213 nm, possibly corresponding to the (002) face of hcp Ni. The inset shows the intensity profile used for estimating the average lattice spacing. (d) Representative EDS spectrum of Ni nanoparticles showing Ni peak, as well as Cu from the TEM substrate, Si from the instrument, and O either from the background or the nanoparticles. TEM images of Ni nanoparticles synthesized from (e) 1 ppm and (f) 10 ppm nickelocene in the small reactor.

HRTEM micrographs of particles synthesized from 1 and 10 ppm nickelocene in the small reactor and directly deposited onto TEM substrates are shown in Figures 5-8(e) and (f), respectively. In comparison with the lower precursor concentration, particle aggregation is visible with increasing y_{nick}, in agreement with the shifts in GM[D_m] measured by the SMPS (see Figure 5-5). The size of the primary particles in the aggregates is notably consistent with the particle sizes in Figures 5-8(a) and (b), suggesting that the PSDs in this system grow past some critical size primarily by aggregation rather than vapor condensation as y_{nick} is increased. This growth mechanism is consistent with the decrease in N_{total} observed earlier between 1 ppm and 10 ppm nickelocene. In addition, the primary particles appear to be embedded in an amorphous matrix, further supporting that there is an organic byproduct originating from nickelocene. Although increasing y_{nick} in either reactor substantially increases the mass production rate, the particle properties change dramatically, particularly with regard to dispersity. On the other hand, the particle properties are preserved when y_{nick} is held constant and Q is increased in the larger reactor to preserve τ.

5.4.4 *PSD measurement by SMPS at varying gas volumetric flow rate*

Figure 5-9 shows PSDs obtained in the small and large reactors for different Q at a constant y_{nick} of 0.1 ppm, which was chosen to minimize particle agglomeration; this also allows more valid use of V_{total} to compare relative differences in particle mass throughput. The values of Q were chosen to provide some overlap of τ in the two reactors, though due to practical limitations, much lower values were accessible in the small reactor than in the large, and *vice versa*. A summary of PSD parameters obtained from

log-normal fits to the data is shown in Table 5-4. For the small reactor, it was found that increasing Q from 0.39 to 1.17 slm, thereby decreasing τ from 5.2 to 1.7 ms, increases N_{total} significantly, but only results in small changes to μ and σ. A further increase to 3.51 slm results in only a small change, but increasing to 10.53 slm leads to a decrease in N_{total}. Meanwhile, in the large reactor, increasing Q from 3.51 to 10.53 slm, equivalent to also decreasing τ from 5.2 to 1.7 ms, results in a broadening of the PSD. A Q of 0.13 slm through the small reactor results in no particles at all, while at 1.17 slm, the same τ, a substantial amount of particles are generated. The large reactor does seem to reach a similar limit at τ of 46.8 ms, where very few particles are made.

These results indicate the following. One, the two reactors do not necessarily perform equivalently at the same τ, as was initially hypothesized and as seemed to be the case in Section 5.4.1. Two, at 3.51 slm, the same Q tested for the large reactor in Section 5.4.1, the small reactor has a similar PSD but a large enhancement in nucleation; this enhancement with decreased τ suggests that the precursor conversion efficiency and particle mass throughput, $Q_R V_{total}$, can surpass those of the large reactor with an identical feed rate. The large reactor did also exhibit a nucleation enhancement with decreased τ, but it is much less pronounced and also accompanied by some widening of the PSD and possibly some agglomeration. It should be noted that higher flow rates were not available to further push the system so that this trend could be further tested. The dependence of the small reactor's performance on τ is surprising: one would expect that the precursor conversion efficiency would decrease with higher Q due to a lower residence time. Potential explanations for these results are provided in the following sections.

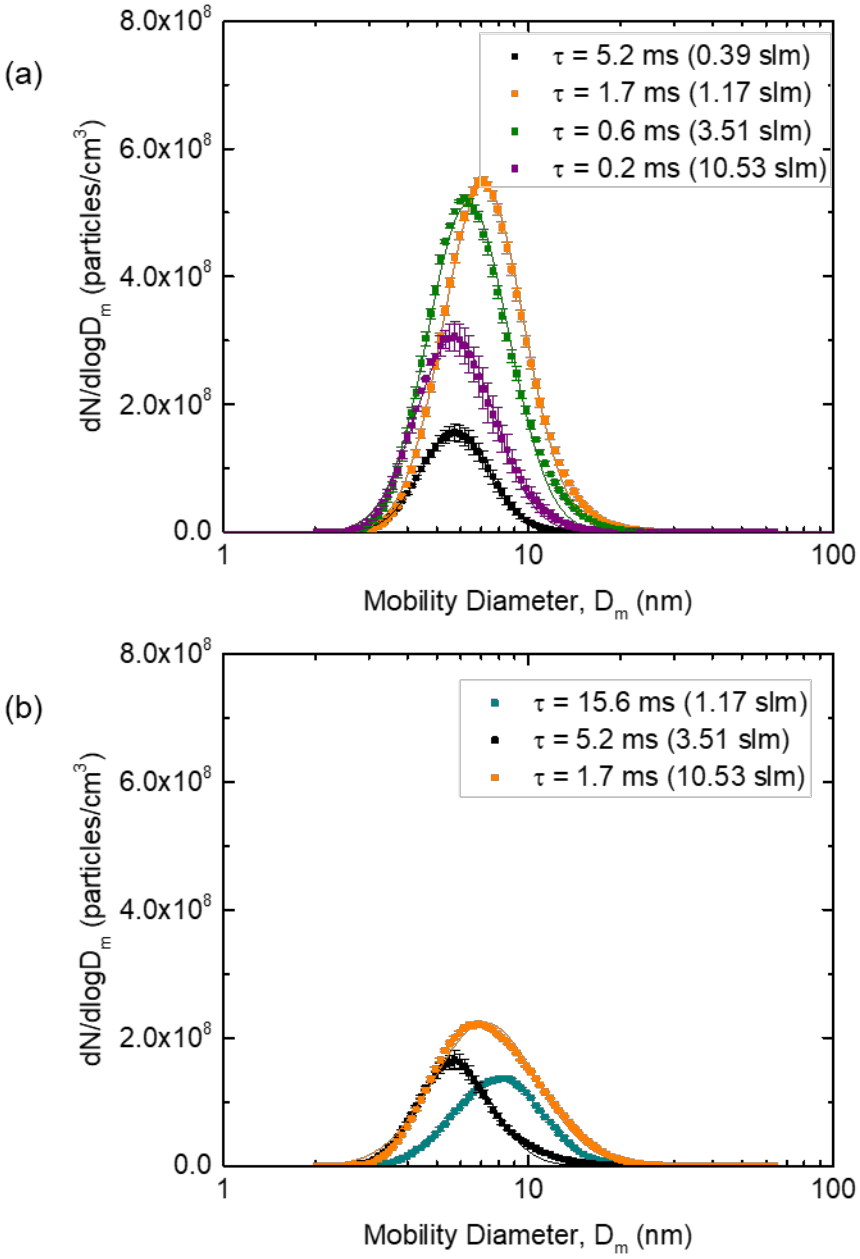

Figure 5-9. PSDs obtained by SMPS measurements in (a) small and (b) large reactors at the indicated reactor flow rates. y_{nick} was 0.1 ppm and applied voltage was 6 kV p-p in all cases. Solid lines represent log-normal fits to the data.

Q_R (slm)	Reactor	τ (ms)	GM[D_m] (nm)	GSD[D_m]	N_{total} (particles/cm^3 x 10^{-7})	$Q_R V_{total}$ (nm^3/min x 10^{-12})
0.13	S	15.6	0	0	0	0
0.39	S	5.2	5.7	1.30	4.4	2.3
1.17	S	1.7	7.1	1.35	18	59
3.51	S	0.6	6.3	1.36	17	122
10.53	S	0.2	5.7	1.34	9.8	150
0.39	L	46.8	5.3	1.36	.035	0.016
1.17	L	15.6	8.0	1.39	4.9	25
3.51	L	5.2	5.7	1.33	4.9	24
10.53	L	1.7	7.2	1.47	9.4	377

Table 5-4. Summary of PSD parameters estimated by log-normal fits to the corresponding data shown in Figure 4-10.

5.4.5 *Reactor dependence on electric field gradient*

The discrepancy in dependence of nanoparticle production rate in the small and large reactor on τ or, equivalently, gas velocity suggests that there is some other fundamental change occurring when increasing reactor volume. Gas flow parameters, ΔU, and d, and, therefore, the applied electric field strength E, equal to $\Delta U/d$, were preserved in the two reactors. However, closer inspection of the geometry of the two reactors reveals that although the spatially averaged electric field strength, $\frac{1}{d}\int_{\frac{(D_o-2d)}{2}}^{\frac{D_o}{2}} E(r)\mathrm{d}r$, is indeed the same at any λ>1, the radial gradient of E, $\frac{\partial E(r)}{\partial r}$, has a pronounced curvature when the ratio $\frac{2d}{D_o-2d}$, or equivalently, $\frac{1}{\lambda-1}$, is high, as in the case of the small reactor. In the case of the large reactor, the curvature is approximately negligible, as would be the

case for parallel plates, i.e., the limit as D_o or λ approach infinity. This is illustrated graphically by Comsol simulations of the two reactors in Figure 5-10, where a significant concentration of field strength is found close to the inner electrode of the small reactor. This analysis, including the Comsol simulations, is performed at the DC limit and does not take into account the influence of ω on *E*, if any. In addition, the simulations assume the externally applied electric field in the absence of a plasma, but the reduced electric field of the plasma after initiation, $\frac{E_{\text{plasma}}}{p}$, is not the same and in fact may be largely independent of the external field.[18] Nonetheless, $\frac{E_{\text{plasma}}}{p}$ itself may be expected to have a significant gradient inside the small reactor, and non-uniform $\frac{E_{\text{plasma}}}{p}$ may, from similarity laws,[17] induce ramifications on other plasma parameters locally.

Such a gradient in $\frac{E_{\text{plasma}}}{p}$ may change other plasma parameters locally[17] or cause changes to the way in which gas velocity couples with plasma characteristics such as, for example, ionic species flux[36] or heat transfer[37] that may in turn influence particle nucleation. In order to support this idea, the small reactor was altered by introducing a larger inner electrode, 3.2 mm OD, which would result in the same $\frac{2d}{D_o-2d}$ as the large reactor, as shown in Figure 5-10(c). In order to maintain the spatially averaged *E*, *ΔU* was also reduced from 6 to 2.5 kV p-p. Similarly, appropriate values of *Q* were also selected in order to yield τ values of 5.2 and 1.7 ms. The results of this modification are shown in Figure 5-11, with y_{nick} set to 0.1 ppm. τ of 5.2 ms once again yields a similar result to that seen in both the small and large reactors, and while decreasing τ to 1.7 ms still results in an enhancement of nucleation, this enhancement is moderate in comparison to that seen

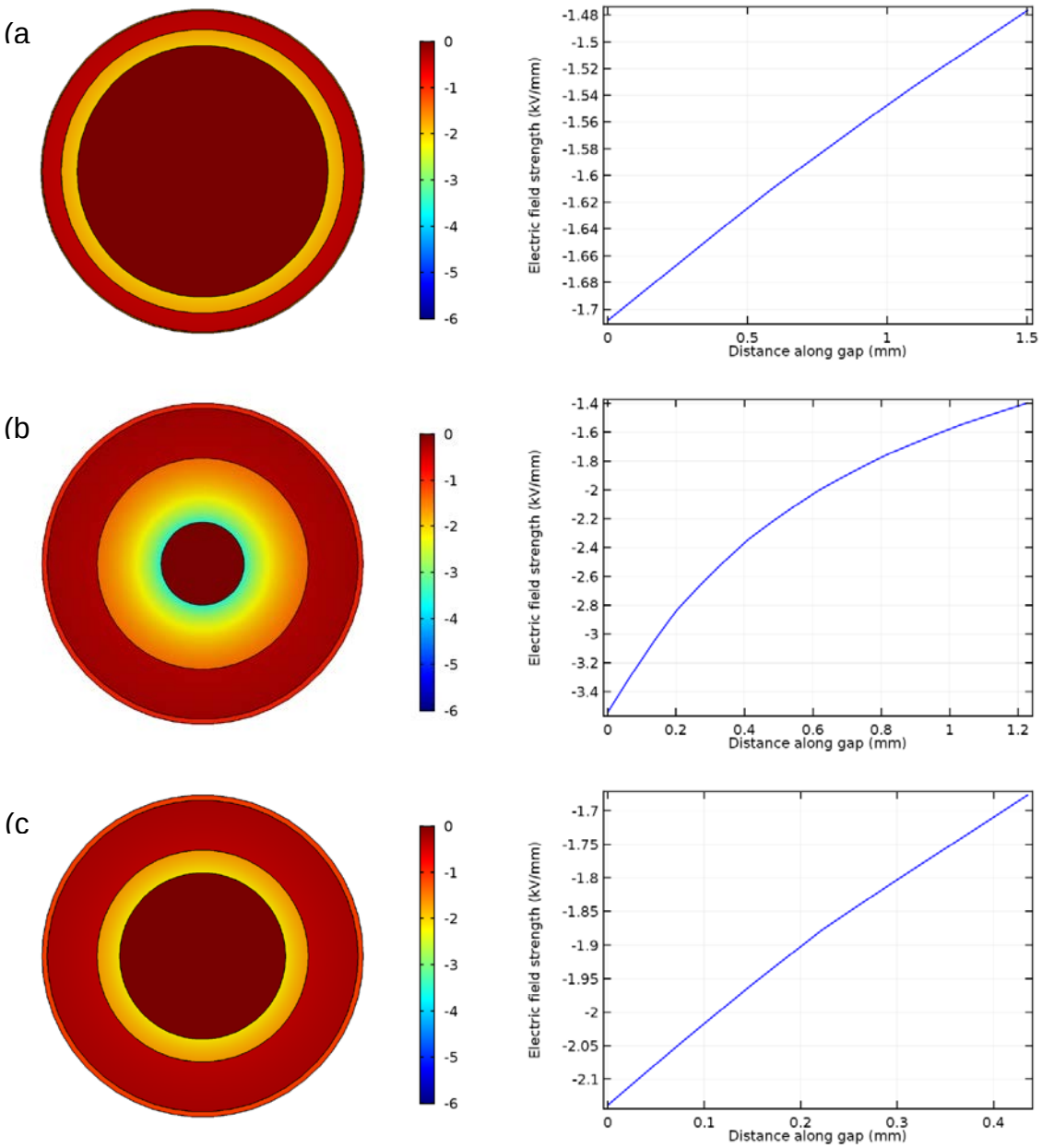

Figure 5-10. Color maps and line graphs showing electric field gradients in the gaps of the (a) large reactor, (b) small reactor with a 1.6 mm diameter inner electrode, and (c) the alternate small reactor with a 3.2 mm diameter inner electrode. Simulations were performed using COMSOL Multiphysics Modeling Software. An electrostatic potential was applied to the reactors, i.e., frequency was not taken into account. 3 kV was applied in (a) and (b) while 1.25 kV was applied in (c).

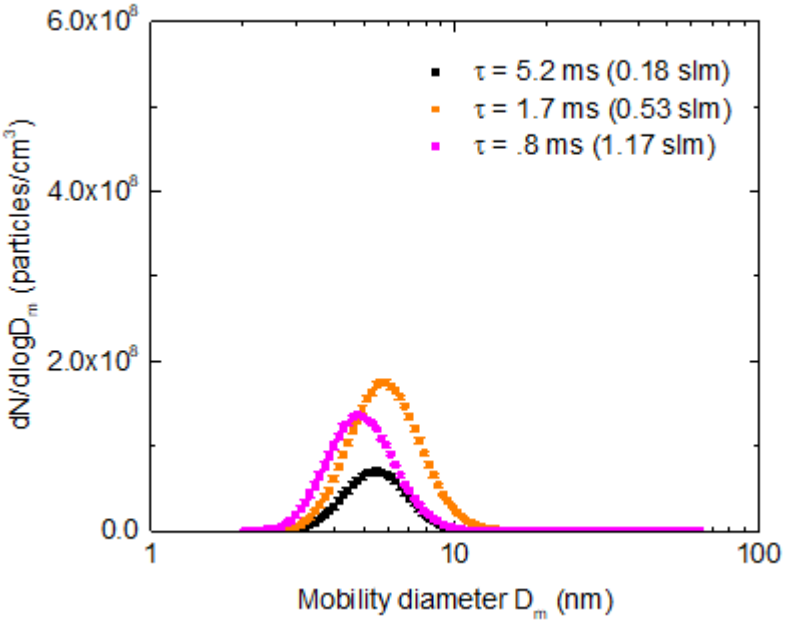

Figure 5-11. PSDs measured by SMPS in the alternative small reactor at the indicated τ. y_{nick} was 0.1 ppm and ΔU was lowered from 6 kV p-p to 2.5 kV p-p in order to keep the average electric field strength the same as the original small reactor.

with a 1.6 mm inner electrode. Furthermore, a decrease in nucleation is seen as τ decreases to 0.8 ms, well before the limit observed with the 1.6 mm electrode. This result points to a correlation between ∇E and nucleation rate, but further studies are needed to isolate ∇E as the root cause of the observed phenomenon. This initial test of that hypothesis is limited partly because of the difficulty of precisely orienting such a small gas gap, but also because changing d alone may have ramifications on the plasma characteristics regardless of the value of ΔU.[17–19]

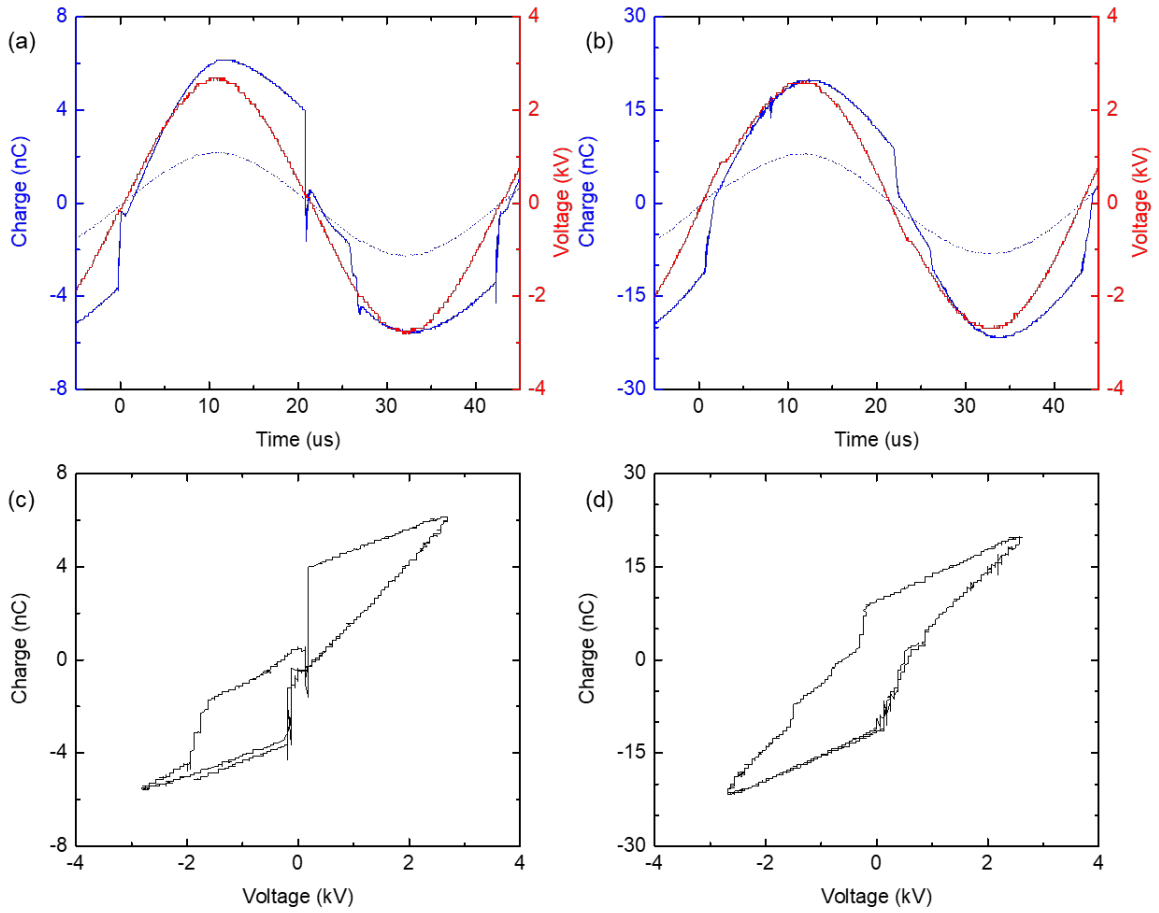

Figure 5-12. Voltage (red) and charge (blue) waveforms in (a) small and (b) large reactors. The applied voltage was 6 kV p-p in both cases. The calibrated displacement charge is also shown (dotted blue). (c,d) Corresponding Lissajous plots for the small and large reactors, respectively.

5.4.6 *Electrical characterization of the DBD reactors*

Voltage and charge waveforms of about one cycle for each reactor operated at 6 kV p-p are shown in Figure 5-12, along with Lissajous plots. The contribution of displacement charge, q_{dis}, in each reactor is also shown. Ar flow rate and precursor concentration were not found to have a significant effect on the length of the plasma or

on its electrical characteristics, though higher flow rates did result in a plasma that appeared by eye to be more uniform. Table 5-5 summarizes the relevant electrical characteristics of the plasma in each reactor, including power density, which is defined as

$$Power\ density = \frac{P_{\text{plasma}}}{Plasma\ volume} \tag{5.28}$$

To estimate volume, the length of the plasma itself as estimated from the photos in Figure 4-5 is used, not the length of the copper tape electrode. The plasma length was found to be about the same in the two reactors.

Reactor	ΔU (kV)	Total power (W)	q (nC)	P_{plasma} (W)	q_{dis} (nC)	Plasma volume (mm^3)	Power density (W/cm^3)
S	6	.303 ± .004	10.8 ± .3	.268 ± .005	4.9 ± .1	65	4.13 ± .08
L	6	1.27 ± .04	34.6 ± .2	1.18 ± .05	18.2 ± .7	540	2.19 ± .09
S	4	.148 ± .006	6.5 ± .1	.133 ± .008	3.40 ± .06	43	2.1 ± .2
L	4	.62 ± .02	20.3 ± .3	.59 ± .03	12.7 ± .7	340	1.09 ± .08

Table 5-5. A summary of relevant electrical characteristics extracted from the voltage and charge waveforms of the small and large reactors when initiated at 6 and 4 kV p-p.

The shape of the Lissajous plots confirms more or less that both discharges are indeed filamentary, judging by the step-like patterns appearing in each half-cycle; this is generally to be expected for pure Ar at atmospheric pressure.[38] However, it is also apparent that the power density of the large reactor is only about half that of the small reactor, when for an ideal performance comparison, both would be equal; besides ∇E, mentioned previously, this may also contribute to the discrepancy seen in the nucleation rate of the large and small reactors. The lower power density in the large reactor may

stem from the value of C_{cell} not scaling at the same rate as reactor volume; the scaling of C_{cell} is determined by comparing q_{dis} of each reactor at 6 kV and applying Equation 5.16

$$C_{\text{cell}} = \frac{2\pi L \varepsilon_0 \varepsilon_{\text{h}}}{\ln\left(\frac{D_{\text{o}} + 2h}{D_{\text{o}}}\right) + \varepsilon_{\text{h}} \ln\left(\frac{D_{\text{o}}}{D_{\text{o}} - 2d}\right)} \tag{5.29}$$

where ε_0 is vacuum permittivity, ε_h is the relative permittivity of the dielectric barrier, and h is the thickness of the dielectric barrier. Thus, the reactor's theoretical capacitance can be compared with the values of C_{cell} measured from the voltage and charge waveforms. Plugging in the dimensions tabulated in Table 5-1 and using ε_h=4.5 (the relative permittivity of quartz) shows that only about a 6-fold increase in C_{cell} is theoretically expected for the reactors; the measured values of C_{cell}, meanwhile, show about a 4-fold increase. These values are summarized in Table 5-6. Equation 5.29 also shows that the value of C_{cell} is fairly sensitive to small changes in reactor dimensions. For instance, if the values of d and h are set to be exactly constant between the two reactors (the real dimensions of the large reactor were used for this hypothetical), and values of D_o are correspondingly set so as to incur a 9-fold increase in V, C_{cell} instead is expected to increase 10-fold (these values are tabulated under the column "Ideal" in Table 5-6), demonstrating the need for precise sizing when building a DBD to achieve the desired characteristics. This also demonstrates that even though the surface area adjacent to the gas gap in each reactor scales at the same rate as V in the proposed geometry, C_{cell} might not, which will affect the current and therefore power density of the plasma and thus possibly other characteristics.

Reactor	C_{cell} - Theoretical	C_{cell} - Measured	C_{cell} - Ideal
Small	0.17 pF	.83 ± .02 pF	0.10 pF
Large	1.0 pF	3.1 ± .1 pF	1.0 pF
Large:small ratio	5.9	3.7	10

Table 5-6. Theoretical and measured values of reactor capacitances, plus a hypothetical case where *d* and *h* are exactly the same between the two reactors.

OES was utilized in order to monitor any potential changes to the plasma characteristics. As has been reported in detail elsewhere, the optical emission spectrum of a pure Ar plasma over a range of pressures all the way up to atmospheric allows the determination of electron density, n_e, electron temperature, T_e (assuming a Maxwellian EEDF), and gas temperature, T_g.[39] A full treatment of the emission spectrum is not given here, but it should essentially follow from the previous statement that nearly identical spectra indicate nearly identical plasma parameters. OES of the small and large reactors are shown in Figure 5-13(a) and (b), respectively, at applied voltages of both 6 and 7.5 kV. Very little difference is observed between all spectra, even at different voltages, although the intensity of light (not shown in Figure 5-13 since the spectra have been normalized) and plasma length are much greater at 7.5 kV. These observations are consistent with previous studies of DBDs, where it has been found that ΔU will scale the number of microdischarges per area per time in a DBD but not necessarily alter the character of those microdischarges.[19,40] So, by OES the plasma parameters in the small and large reactors appear to be similar, but this method only assesses a spatial average; a

method with very fine spatial resolution may reveal spectral differences in the two reactors that are not otherwise easily observable.

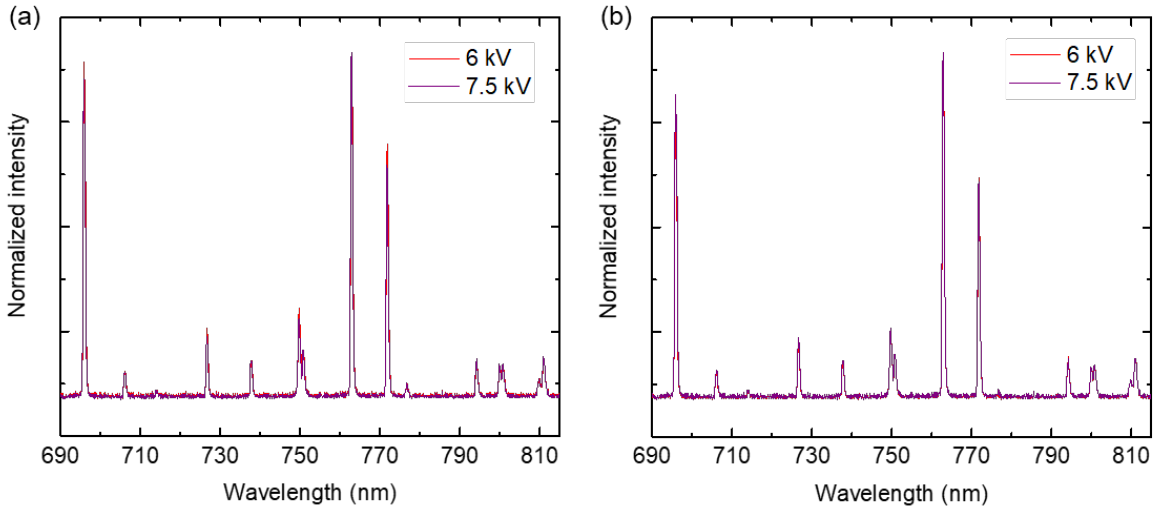

Figure 5-13. OES showing Ar emission lines for (a) small and (b) large reactors at 6 and 7.5 kV p-p.

To test whether nucleation rate in the large reactor could be enhanced similar to the small reactor by controlling for power density, a voltage of 7.5 kV p-p was applied along with a Q of 3.51 slm and y_{nick} of 0.1 ppm. While this results in the same power density as that observed in the small reactor at 6 kV p-p, virtually all particle throughput ceased, perhaps from enhanced electrostatic precipitation on the reactor walls or from less uniform filling of the reactor volume because of enhanced filament formation, as was visibly apparent. On the other hand, decreasing ΔU to 4 kV p-p in both reactors was found to result in an enhancement of particle nucleation, as shown in Figure 5-14. Examining the corresponding Lissajous plots in Figures 5-14(b) and (c) reveals that at this ΔU, the plasma regime approaches a glow[38] or even pseudo-glow[41] regime, as

indicated by their increasingly parallelogram-like shapes. This result suggests that, in addition to all other parameters discussed already, plasma regime may also be a necessary consideration for improving reactor efficiency when scaling up.

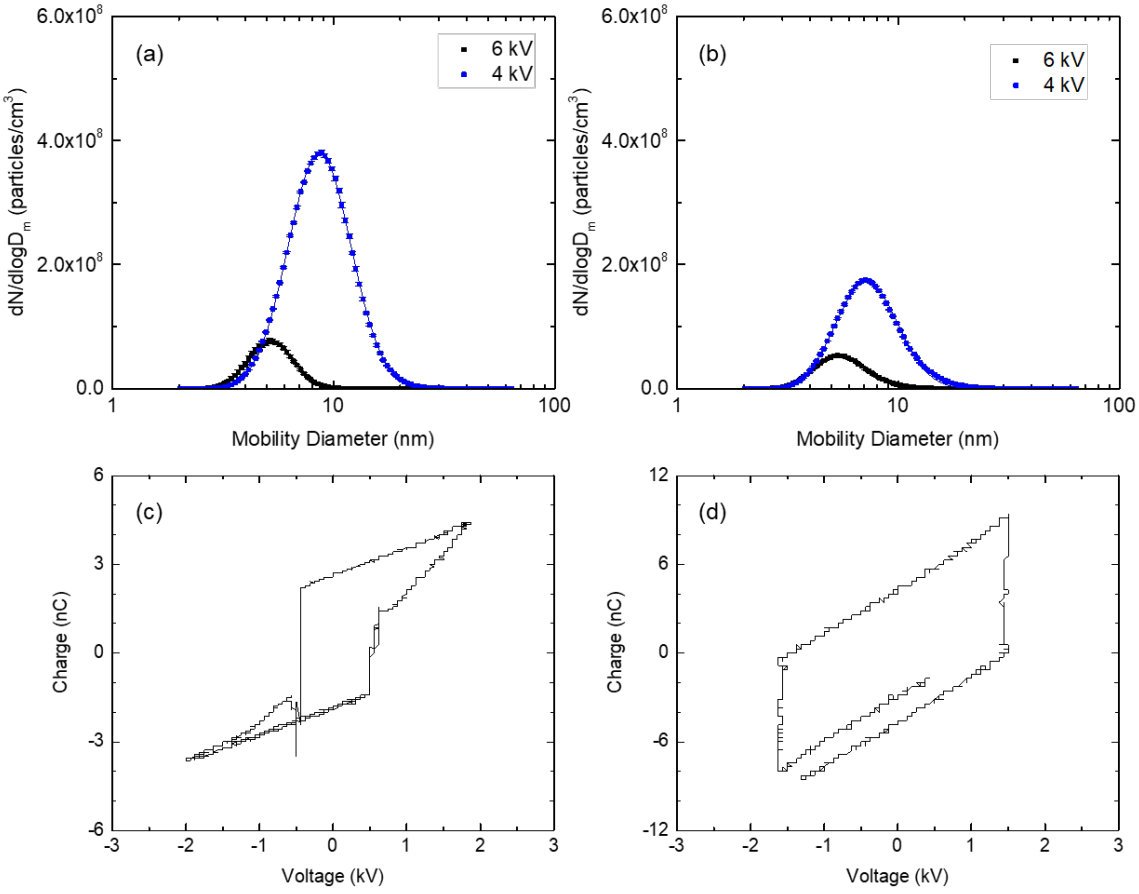

Figure 5-14. (a,b) SMPS measurements in the small and large reactors, respectively, showing a dramatic increase in nucleation with decreasing voltage. (c,d) Corresponding Lissajous plots indicating a transition in both reactors toward a glow regime.

5.5 Conclusions and future work

A coaxial electrode DBD plasma system has been studied for nanoparticle synthesis by homogeneous nucleation to evaluate the potential for scale-up. The advantage of this geometry is that the plasma volume can be easily increased while preserving a small electrode gap to maintain U_b and other important characteristics. For a particular residence time, it was found that the nanoparticle production rate increases with reactor volume without altering the PSD, all other operating variables being constant. While only shown for two test reactors, this approach should be applicable to any reactor volume and offers a path to scaling up to achieve even higher production rates than those shown here. Additional experiments showed that PSD is not necessarily preserved at all residence times, however; specifically, increasing the gas velocity in a smaller volume reactor leads to a significant increase in particle concentration that is not as pronounced in a larger volume reactor. Additional understanding of how plasma parameters and fluid effects couple to control particle growth dynamics is required in order to achieve a truly optimal scale-up strategy.

5.6 Acknowledgments

This work was conducted in collaboration with Dr. Yao Zhang, Dr. Chang-jun Liu, and Tianqi Liu and was supported by NSF Grant No. CBET-1335990, the National Natural Science Foundation of China (#21476157), Tianjin Municipal Natural Science Foundation (12JCQNJC04500), and the China Scholarship Council (CSC file No. 201506250013). We would also like to thank Danqi Wang for assistance with TEM, and

Joseph Toth and Mihai Bilici for help with design and electrical characterization of the DBD reactors.

5.7 References

1. Kogelschatz, U. Dielectric-barrier Discharges : Their History , Discharge Physics , and Industrial Applications. *Plasma Chem. Plasma Process.* **23,** 1–46 (2003).
2. Eliasson, B., Hirth, M. & Kogelschatz, U. Ozone synthesis from oxygen in dielectric barrier discharges. *J. Phys. D. Appl. Phys.* **20,** 1421–1437 (1987).
3. Kogelschatz, U. Ultraviolet excimer radiation from nonequilibrium gas discharges and its application in photophysics , photochemistry and photobiology. *J. Opt. Technol.* **79,** 484–493 (2012).
4. Bogaerts, A., Kozak, T., van Laer, K. & Snoeckx, R. Plasma-based conversion of CO2: current status and future challenges. *Faraday Discuss.* **183,** 217–232 (2015).
5. Tu, X. & Whitehead, J. C. Plasma-catalytic dry reforming of methane in an atmospheric dielectric barrier discharge: Understanding the synergistic effect at low temperature. *Appl. Catal. B Environ.* **125,** 439–448 (2012).
6. Hammer, T., Kappes, T. & Baldauf, M. Plasma catalytic hybrid processes: gas discharge initiation and plasma activation of catalytic processes. *Catal. Today* **89,** 5–14 (2004).
7. Corke, T. C., Enloe, C. L. & Wilkinson, S. P. Dielectric Barrier Discharge Plasma Actuators for Flow Control. *Annu. Rev. Fluid Mech.* **42,** 505–529 (2010).
8. von Woedtke, T., Reuter, S., Masur, K. & Weltmann, K. Plasmas for medicine. *Phys. Rep.* **530,** 291–320 (2013).

9. Babaeva, N. Y. & Kushner, M. J. Reactive fluxes delivered by dielectric barrier discharge filaments to slightly wounded skin. *J. Phys. D. Appl. Phys.* **46,** 25401 (2013).

10. Wagner, H.-E. *et al.* The barrier discharge: basic properties and applications to surface treatment. *Vacuum* **71,** 417–436 (2003).

11. Vons, V., Creyghton, Y. & Schmidt-Ott, A. Nanoparticle production using atmospheric pressure cold plasma. *J. Nanoparticle Res.* **8,** 721–728 (2006).

12. Bergmann, R. B. & Bill, A. On the origin of logarithmic-normal distributions: An analytical derivation, and its application to nucleation and growth processes. *J. Cryst. Growth* **310,** 3135–3138 (2008).

13. Narayanan, R. & El-Sayed, M. A. Catalysis with transition metal nanoparticles in colloidal solution: Nanoparticle shape dependence and stability. *J. Phys. Chem. B* **109,** 12663–12676 (2005).

14. Bell, A. T. *et al.* The impact of nanoscience on heterogeneous catalysis. *Science (80-.).* **299,** 1688–91 (2003).

15. Girshick, S. L. & Chiu, C.-P. Homogeneous Nucleation of Particles from the Vapor Phase in Thermal Plasma Synthesis. *Plasma Chem. Plasma Process.* **9,** 355–369 (1989).

16. Flagan, R. C. & Lunden, M. M. Particle structure control in nanoparticle synthesis from the vapor phase. *Mater. Sci. Eng. A* **204,** 113–124 (1995).

17. Ferreira, C. & Moisan, M. The similarity laws for the maintenance field and the absorbed power per electron in low-pressure surface wave produced plasmas and their extension to HF plasmas in general. *Phys. Scr.* **38,** 382–399 (1988).

18. Moisan, M. *et al.* Radio frequency or microwave plasma reactors? Factors determining the optimum frequency of operation. *J. Vac. Sci. Technol. B* **9,** 8–25 (1991).

19. Brandenburg, R. Dielectric barrier discharges: progress on plasma sources and on the understanding of regimes and single filaments. *Plasma Sources Sci. Technol.* **26,** 53001 (2017).

20. Bilik, N., Greenberg, B. L., Yang, J., Aydil, E. S. & Kortshagen, U. R. Atmospheric-pressure glow plasma synthesis of plasmonic and photoluminescent zinc oxide nanocrystals. *J. Appl. Phys.* **119,** 243302 (2016).

21. Askari, S. *et al.* Silicon-based quantum dots: synthesis, surface and composition tuning with atmospheric pressure plasmas. *J. Phys. D. Appl. Phys.* **48,** 314002 (2015).

22. Fan, P., Chu, J. & Shao, J. Conductance calculation of long tubes with rectangular cross section and annular cross section in the full pressure range. *Vacuum* **68,** 373–378 (2003).

23. Boisvert, J., Margot, J. & Massines, F. Transitions of an atmospheric-pressure diffuse dielectric barrier discharge in helium for frequencies increasing from kHz to MHz. *Plasma Sources Sci. Technol.* **26,** 35004 (2017).

24. Chiang, W. H. & Sankaran, R. M. Microplasma synthesis of metal nanoparticles for gas-phase studies of catalyzed carbon nanotube growth. *Appl. Phys. Lett.* **91,** 121503 (2007).

25. Lin, P. A. & Sankaran, R. M. Plasma-Assisted Dissociation of Organometallic Vapors for Continuous, Gas-Phase Preparation of Multimetallic Nanoparticles.

Angew. Chemie - Int. Ed. **50,** 10953–10956 (2011).

26. Ghosh, S. *et al.* Atmospheric-pressure dielectric barrier discharge with capillary injection for gas-phase nanoparticle synthesis. *J. Phys. D. Appl. Phys.* **48,** 314003 (2015).

27. Pipa, A. V., Hoder, T., Koskulics, J., Schmidt, M. & Brandenburg, R. Experimental determination of dielectric barrier discharge capacitance. *Rev. Sci. Instrum.* **83,** 75111 (2012).

28. Pipa, A. V., Koskulics, J., Brandenburg, R. & Hoder, T. The simplest equivalent circuit of a pulsed dielectric barrier discharge and the determination of the gas gap charge transfer. *Rev. Sci. Instrum.* **83,** 115112 (2012).

29. Torres-Gómez, L. A., Barreiro-Rodríguez, G. & Méndez-Ruiz, F. Vapour pressures and enthalpies of sublimation of ferrocene, cobaltocene and nickelocene. *Thermochim. Acta* **124,** 179–183 (1988).

30. Girshick, S. *et al.* Thermal plasma synthesis of ultrafine iron particles. *J. Aerosol Sci.* **24,** 367–382 (1993).

31. Swihart, M. T. Vapor-phase synthesis of nanoparticles. *Curr. Opin. Colloid Interface Sci.* **8,** 127–133 (2003).

32. Ding, Y. *et al.* A parametric study of non-thermal plasma synthesis of silicon nanoparticles from a chlorinated precursor. *J. Phys. D. Appl. Phys.* **47,** 485202 (2014).

33. Yasar-Inceoglu, O., Lopez, T., Farshihagro, E. & Mangolini, L. Silicon nanocrystal production through non-thermal plasma synthesis: a comparative study between silicon tetrachloride and silane precursors. *Nanotechnology* **23,** 255604

(2012).

34. Alvarez Barragan, A., Ilawe, N. V., Zhong, L., Wong, B. M. & Mangolini, L. A Non-Thermal Plasma Route to Plasmonic TiN Nanoparticles. *J. Phys. Chem. C* **121,** 2316–2322 (2017).

35. He, L. Hexagonal close-packed nickel or Ni3C? *J. Magn. Magn. Mater.* **322,** 1991–1993 (2010).

36. Petrović, D., Martens, T., Dijk, J. Van, Brok, W. J. M. & Bogaerts, A. Modeling of a dielectric barrier discharge used as a flowing chemical reactor. *J. Phys. Conf. Ser.* **133,** 12023 (2008).

37. Tirumala, R. *et al.* Temperature characterization of dielectric barrier discharge actuators: influence of electrical and geometric parameters. *J. Phys. D. Appl. Phys.* **47,** 255203 (2014).

38. Okazaki, S., Kogoma, M., Uehara, M. & Kimura, Y. Appearance of stable glow discharge in air, argon, oxygen and nitrogen at atmospheric pressure using a 50 Hz source. *J. Phys. D. Appl. Phys.* **26,** 889–892 (1993).

39. Zhu, X.-M. & Pu, Y.-K. A simple collisional-radiative model for low-temperature argon discharges with pressure ranging from 1 Pa to atmospheric pressure: kinetics of Paschen 1s and 2p levels. *J. Phys. D. Appl. Phys.* **43,** 15204 (2010).

40. Borra, J. P., Jidenko, N., Hou, J. & Weber, A. Vaporization of bulk metals into single-digit nanoparticles by non-thermal plasma filaments in atmospheric pressure dielectric barrier discharges. *J. Aerosol Sci.* **79,** 109–125 (2015).

41. Radu, I., Bartnikas, R. & Wertheimer, M. R. Frequency and Voltage Dependence of Glow and Pseudoglow Discharges in Helium Under Atmospheric Pressure.

IEEE Trans. Plasma Sci. **31,** 1363–1378 (2003).

Chapter 6: Conclusions and outlook

6.1 Comments on important findings

Direct homogeneous nucleation of diamond nanoparticles was the original goal of this study, though that remained elusive outside of the direct-current (DC) microplasma process reported in Chapter 2. Although that process produced diamond in small quantities, it was accompanied by a large quantity of non-diamond carbon and metallic impurities originating from the reactor electrodes. In Chapter 4, a similar process was designed to eliminate metal contamination by relocating the electrodes to the outside of the reactor and using radio-frequency (RF) excitation to generate a discharge. This modified process also operated at atmospheric-pressure and utilized the same vapor precursors, but the resulting homogeneously nucleated material was remarkably distinct (specifically, more graphitic) from that of the DC microplasma and did not appear to contain any diamond. The experiments performed with these two reactors focused on the role of precursor chemistry in determining material structure, though the precursors themselves (specifically methanol and ethanol) were found to have only a small influence outside of nucleation and growth rates. This suggests a stronger dependence of material structure on the type of plasma discharge instead, which may lead to very different reaction pathways. Alternatively, the presence of a metal surface in contact with the plasma may itself play an important role.

The choice of precursors and rationale behind the experiments in Chapters 2 and 4 were informed by the example of the Bachmann diagram utilized in chemical vapor deposition (CVD) of diamond.[1] The addition of H_2 to preferentially etch non-diamond carbon, a crucial component of the diamond CVD process,[2] was also tested with homogeneous carbon particle growth in a low pressure capacitively-coupled RF plasma

(RF CCP) in Chapter 3 and yielded unexpected results. While the H_2 did result in lower production rates of carbon powder, Raman spectra and TEM imaging of the produced powders showed a positive correlation between graphitic content and amount of H_2 added to the gas feed, the opposite of the trend that was expected. On the other hand, when a similar set of experiments with H_2 addition was carried out in the atmospheric-pressure RF CCP in Chapter 4, H_2 was again found to lower production rates of carbon powder, but almost no change in material structure was observed. The exact role of H_2 in these reactions may be complex; in addition to acting as a chemical etchant, it may also cause significant changes in the plasma characteristics or chemically inhibit carbon particle nucleation.[3] Further experiments would be needed to narrow down the possibilities.

In light of these results, it may be the case that an analogy between a diamond CVD process and homogeneous carbon particle growth in flow-through plasma reactors is limited. In contrast with typical diamond CVD occurring on a heated substrate in a large-volume chamber, the processes studied here occur within much shorter residence times and are dominated by convection transport rather than diffusion. The governing principles and important variables may then be distinct. Additionally, as mentioned before, the type of plasma used may be very important. In the end, the most reliable method of achieving clean diamond growth in this work was microwave plasma-enhanced CVD (MPCVD). As some authors have pointed out, microwave excitation tends to be more favorable for diamond growth by CVD than RF due to lower ion energies.[4,5] Microwave plasma may then offer another area of exploration into homogeneous nucleation of diamond; work by Gries *et al.*[6] has already shown evidence of diamond dust formation during MPCVD and could therefore offer a springboard for future studies.

Finally, the results in Chapter 5 open a promising path toward scale-up of atmospheric-pressure non-thermal plasma reactors for homogeneous synthesis of nanoparticles that could conceivably be applied for any material and perhaps for discharge types other than kHz-driven dielectric barrier discharge, such as RF-α or microwave. Importantly, adequate proof of concept that particle size distribution can be preserved while increasing reactor volume and particle throughput was achieved under some conditions but not all. Improvement on the proposed strategy can be made by studying in more depth the relationship between reactor geometry and local plasma characteristics and how these impact particle nucleation, growth, and agglomeration processes.

6.2 Future work

Throughout the myriad directions explored in this work, promising threads for continued studies have been identified. For example, the coinjection of SiH_4 and CH_4 into a low-pressure RF CCP (see Section 3.3.2) did not result in seeded diamond growth but did, under some conditions, result in synthesis of 3C SiC nanoparticles, albeit with an amorphous carbon coating. This is an important finding, since, like diamond, SiC can also contain useful color center defects.[7,8] If the reactant chemistry and operating conditions can be adjusted appropriately to minimize amorphous carbon while still maintaining SiC growth (Raman signatures of SiC, which were not observed in this work because of the amorphous coating, would be an important indicator of purity), investigation of color center incorporation in SiC nanoparticles during synthesis is well motivated. This could then result in a process similar to what had originally been envisioned for diamond nanoparticles: a simple, low cost, and high throughput method of producing SiC

nanoparticles in the gas phase with a controlled size distribution and controlled introduction of color centers.

In addition to SiC, the discovery of silicon-vacancy (Si-V) color centers in diamond film grown on a deposit of Si nanoparticles on copper is particularly exciting (see Section 3.3.3). Although Si-V centers have been incorporated in diamond as a result of growth on Si wafer substrates,[9] this method of incorporation is novel to the best of our knowledge and significant in its ability to easily grow a diamond film without the need for any prior seeding with diamond powder. This inspires further research questions: is there a diamond nucleation enhancement on Si nanoparticles in comparison with a Si wafer, and if so, what causes this enhancement? Does this method result in more Si-V centers than growth on a Si wafer does? Can this same method be used to incorporate alternative color centers, such as germanium-vacancy,[10,11] by using nanoparticle films of other materials?

Some limitations are worth highlighting as areas for improvement, as well. For instance, the diamond film grown by this method consisted of particle grains larger than 100 nm (see Figure 3-12(a)) when ideally the desired size is less than 10 nm. This could be remedied by operating methods that yield exceptionally high nucleation densities, such as DC bias-enhanced nucleation,[12] use of Ar/CH_4 mixture as feed, which results in so-called 'ultrananocrystalline' films composed of 2-5 nm grains,[13] or both.[14] Finally, because individual nanoparticles are desired instead of films, a compelling though challenging direction is development of a process in which diamond growth may occur on an aerosol suspension of nanoparticles (composed of Si, Ge, etc.) fed into a microwave plasma chamber; this could be thought of as microwave plasma-enhanced CVD with the nanoparticle surfaces themselves acting as the substrate. Furthermore, a process can be

envisioned which would occur in at least two steps: upstream conversion of gas-phase reactants into nanoparticle aerosol by an RF CCP followed by injection into a microwave plasma chamber. Particle surface temperature and residence time are likely to be important variables; some inspiration may be taken from a previously reported method of diamond growth by hot filament CVD on top of diamond seed particles levitated in an RF field.[15]

6.3 References

1. Bachmann, P. K., Leers, D. & Lydtin, H. Towards a general concept of diamond chemical vapour deposition. *Diam. Relat. Mater.* **1,** 1–12 (1991).
2. Angus, J. C. & Hayman, C. C. Low-Pressure, Metastable Growth of Diamond and 'Diamondlike' Phases. *Science (80-.).* **241,** 913–921 (1988).
3. De Bleecker, K., Bogaerts, A. & Goedheer, W. Detailed modeling of hydrocarbon nanoparticle nucleation in acetylene discharges. *Phys. Rev. E* **73,** 26405 (2006).
4. Matsumoto, S. Development of diamond synthesis techniques at low pressures. *Thin Solid Films* **368,** 231–236 (2000).
5. Jackman, R. B., Beckman, J. & Foord, J. S. Diamond chemical vapor deposition from a capacitively coupled radio frequency plasma. *Appl. Phys. Lett.* **66,** 1018–1020 (1995).
6. Gries, T., Vandenbulcke, L., Rouzaud, J. N. & de Persis, S. Diagnostics in dusty C–H–O plasmas with diamond and graphitic nanoparticle generation. *Plasma Sources Sci. Technol.* **19,** 25015 (2010).
7. Castelletto, S. *et al.* Room temperature quantum emission from cubic silicon carbide nanoparticles. *ACS Nano* **8,** 7938–7947 (2014).

8. Radulaski, M. *et al.* Scalable Quantum Photonics with Single Color Centers in Silicon Carbide. *Nano Lett.* **17,** 1782–1786 (2017).

9. Vlasov, I. I. *et al.* Nanodiamond Photoemitters Based on Strong Narrow-Band Luminescence from Silicon-Vacancy Defects. *Adv. Mater.* **21,** 808–812 (2009).

10. Bhaskar, M. K. *et al.* Quantum Nonlinear Optics with a Germanium-Vacancy Color Center in a Nanoscale Diamond Waveguide. *Phys. Rev. Lett.* **118,** 223603 (2017).

11. Iwasaki, T. *et al.* Germanium-Vacancy Single Color Centers in Diamond. *Sci. Rep.* **5,** 12882 (2015).

12. Williams, O. A. Nanocrystalline diamond. *Diam. Relat. Mater.* **20,** 621–640 (2011).

13. Xiao, X., Birrell, J., Gerbi, J. E., Auciello, O. & Carlisle, J. A. Low temperature growth of ultrananocrystalline diamond. *J. Appl. Phys.* **96,** 2232–2239 (2004).

14. Alcantar-Peña, J. J. *et al.* Fundamentals towards large area synthesis of multifunctional Ultrananocrystalline diamond films via large area hot filament chemical vapor deposition bias enhanced nucleation/bias enhanced growth for fabrication of broad range of multifunctional devices. *Diam. Relat. Mater.* **78,** 1–11 (2017).

15. Shimizu, S. *et al.* Synthesis of diamond fine particles on levitated seed particles in a rf CH4/H2 plasma chamber equipped with a hot filament. *J. Appl. Phys.* **112,** 73303 (2012).